05 STIF III

APPLICATION OF LANDSAT TO THE MANAGEMENT OF DELAWARE'S MARINE AND WETLAND RESOURCES

Vytautas Klemas, Principal Investigator
Center for Remote Sensing
College of Marine Studies
University of Delaware
Newark, Delaware 19711

Final Report for Period:
February 1976 - December 1977

20570

(E78-10068) APPLICATION OF LANDSAT TO THE MANAGEMENT OF DELAWARE'S MARINE AND WETLAND RESOURCES Final Report, Feb. 1976 - Dec. 1977 (Delaware Univ.) 142 p CSCL 08C

N78-17441

HC A07/MF A01

Unclas
G3/43 00068

TECHNICAL REPORT STANDARD TITLE PAGE

1. Report No.	2. Government Accession No.	3. Recipient's Catalog No.
Final		

4. Title and Subtitle	5. Report Date
Application of Landsat to the Management of Delaware's Marine and Wetland Resources	December 1977
	6. Performing Organization Code

7. Author(s)	8. Performing Organization Report No.
V. Klemas, D. Bartlett, G. Davis, W. Philpot, R. Rogers*	

9. Performing Organization Name and Address	10. Work Unit No.
Center for Remote Sensing, College of Marine Studies, University of Delaware, Newark, Delaware 19711	11. Contract or Grant No. NAS5-20983
	13. Type of Report and Period Covered Final Feb. 1976-Dec. 1977
12. Sponsoring Agency Name and Address James R. Higgins National Aeronautics & Space Administration Goddard Space Flight Center, Greenbelt, MD	14. Sponsoring Agency Code

15. Supplementary Notes

R. Rogers, Bendix Aerospace Systems Division, Earth Resources Directorate, 3621 S. State Rd., Ann Arbor, Michigan 48107

16. Abstract

Analysis of Landsat imagery was applied to monitoring of several aspects of Delaware's marine environment. Landsat data was found to be the best source of synoptic information on the distribution of horizontal water mass discontinuities (fronts) at different portions of the tidal cycle. Distributions observed were used to improve an oil slick movement predication model for Delaware Bay. Landsat data was used to monitor the movement and dispersion of industrial acid waste material dumped over the continental shelf. A technique for assessing aqueous sediment concentration with limited ground truth has been proposed.

A technique for training automated anlaysis of Landsat multi-spectral data based on in situ measurements of target reflectance was tested in Delaware's wetlands and found to produce comparable classification accuracy to conventional relative radiance training. Soil moisture and plant morphology were found to be dominant physical factors affecting target reflectance. Studies indicated that green plant biomass assessment is possible using Landsat-MSS spectral bands but may be limited by spatial resolution available.

(see next page)

17. Key Words (Selected by Author(s))	18. Distribution Statement
Estuarine fronts, pollution dispersion, monitoring of offshore industrial waste dumps, sediment concentration, coastal wetland vegetation, biomass, onshore impact of offshore oil & gas development.	

19. Security Classif. (of this report)	20. Security Classif. (of this page)	21. No. of Pages	22. Price*
None	None		

*For sale by the Clearinghouse for Federal Scientific and Technical Information, Springfield, Virginia 22151.

Figure 2. Technical Report Standard Title Page

Landsat imagery was found to be useful in updating land use maps for a frontier-type coastal oil exploration area but must be combined with other data sources if detailed categorization and identification of functional relationships are desired.

APPLICATION OF LANDSAT TO THE MANAGEMENT OF DELAWARE'S MARINE AND WETLAND RESOURCES

Vytautas Klemas
Principal Investigator
Center for Remote Sensing
College of Marine Studies
University of Delaware
Newark, Delaware 19711

December 1977

Final Report for Period February 1976 - December 1977

Prepared for:

Goddard Space Flight Center
Greenbelt, Maryland 20771

TABLE OF CONTENTS

I.	SUMMARY OF CONCLUSIONS	1
	1.1 Density Fronts and Their Effects on Coastal Pollutants	1
	1.2 Determination of the Concentration of Suspended Sediment by Remote Sensing	1
	1.3 Monitoring the Dispersion and Movement of Ocean Dump Plumes	2
	1.4 Analysis of Coastal Vegetation	3
	1.5 Analysis of Effects of Offshore Development on Coastal Land Use in the Kenai Region, Alaska	3
II.	DENSITY FRONTS AND THEIR EFFECTS ON COASTAL POLLUTANTS	5
	2.0 Introduction	5
	2.1 Description of the Delaware Estuarine System	8
	2.2 Oceanography of Estuarine Fronts	9
	2.3 Effect of Fronts on Oil Slick Movement	12
	2.4 Mapping Fronts with Satellites	15
	2.5 Conclusions	19
	2.6 References	20
	2.7 List of Figures	22
III.	DETERMINATION OF THE CONCENTRATION OF SUSPENDED SEDIMENT BY REMOTE SENSING	53
	3.0 Introduction	53
	3.1 Signal at the Remote Sensing Instrument	53
	3.2 Interaction of Light with Water	54
	3.3 Relationship Between Concentration and Radiance	55
	3.4 Discussion	59
	3.5 Conclusions	62
	3.6 References	63
	3.7 List of Figures	63

IV. MONITORING THE DISPERSION AND MOVEMENT OF OCEAN DUMP PLUMES 69

4.0 Introduction 69

4.1 Waste Composition and Disposal 69

4.2 Satellite Observations 71

4.3 Application of Current Drogues 73

4.4 Discussion of Results 74

4.5 Conclusions 77

4.6 References 78

4.7 List of Figures 80

V. COASTAL VEGETATION STUDIES 91

5.1 Introduction 91

5.2 Methods 92

5.21 Field Studies 95

5.22 Landsat Data Processing and Evaluation of Classified Results 97

5.3 Results 102

5.4 Conclusions 109

5.5 References 110

5.6 List of Figures 111

VI. ANALYSIS OF THE EFFECTS OF OFFSHORE DEVELOPMENT ON COASTAL LAND USE IN THE KENAI REGION, ALASKA 116

6.0 Introduction 116

6.1 Offshore Petrochemical Development 116

6.2 Remote Sensing Analysis and Change Assessment 121

6.21 Aircraft 122

6.22 Landsat 124

6.3 Separating Offshore - and Onshore - Related Land Use Changes 128

√

6.4 Conclusions 131

6.5 References 132

6.6 List of Figures 132

APPENDIX A - Publications and Invited Presentations 135

I. SUMMARY OF CONCLUSIONS

Analysis of Landsat-MSS data was found to be of real or potential value in a number of applications to Delaware's marine and coastal environments.

1.1 Density Fronts and Their Effects on Coastal Pollutants

Imagery from Landsat-1 and Landsat-2 proved valuable in mapping the location, type and extent of estuarine fronts in Delaware Bay over all portions of the tidal cycle. Satellite observations of flood-associated fronts on the New Jersey side of the Bay and ebb-associated fronts on the Delaware side, where studies were being conducted, agreed with boat measurements and model predictions. Since estuarine fronts influence the movement of oil slicks and the dispersion of other pollutants, clean-up operations depending on the use of oil slick drift prediction models will benefit from aircraft tracking the actual slicks and from Landsat observations of surface currents and frontal systems. Neither ships nor aircraft alone were as effective in providing a complete, snyoptic and repetitive overview as did the satellite.

1.2 Determination of the Concentration of Suspended Sediment by Remote Sensing

A method is presented for making estimates of the concentration of suspended matter in Delaware Bay with only a limited amount of ground truth. The method makes use of the fact that there is normally a wide range of concentrations in bay waters to derive an equation relating radiance to concentration. There are two primary assumptions made: 1) atmospheric effects are effectively constant over the entire bay and 2) suspended material is optically the same throughout the bay.

If this approach proves workable it should be possible to compare Landsat data for different overpasses of the bay with only a few data points

for each pass.

1.3 Monitoring the Dispersion and Movement of Ocean Dump Plumes

Satellites such as Landsat offer an effective means of assessing the drift and dispersion of industrial waste dumped on the continental shelf. This is particularly true for the acid wastes disposal site approximately 64 km off the Delaware coast. These wastes form a sparse but optically persistent ferric floc which can be observed by Landsat's multispectral scanner band 4 up to three days after dump.

Most of the 22 waste plumes imaged by Landsat were found to be drifting at average rates of 0.28 knot to 1.83 knots into the southwest quadrant. The plumes seemed to remain above the thermocline which was observed to form from June through August at depths ranging from 13 to 31 meters. During the remainder of the year, the ocean at the test site was not stratified, permitting wastes to mix throughout the water column to the bottom.

The magnitudes of plume drift velocities were compatible with the drift velocities of current drogues released over a twelve month period at the surface, at mid-depth and near the bottom. However, during the stratified warm months, more drogues tended to move in the north-northeast direction, while during the non-stratified winter months a southwest direction was preferred. Drogues released at different depths frequently traveled along different paths and at different speeds, indicating the presence of current shear.

Rapid movement toward shore occurs primarily during storms, particularly northeasters. During such storms, however, the plume is rapidly dispersed and diluted. Therefore, the probability of an identifiable plume containing heavy concentrations of waste reaching the shore is quite low.

1.4 Analysis of Coastal Vegetation

Digital analysis of Landsat earth resources data may realize significant advantages from *in situ* measurements of terrestrial target radiance and transformation of these and MSS data to absolute reflectance by application of appropriate solar and atmospheric corrections. Such a technique would, in some cases, allow more accurate derivation of target signatures and facilitate temporal extension of signatures obtained. A recently developed technique for *in situ* radiance measurement and atmospheric correction was tested using four cover categories in Delaware's tidal wetlands. The atmospheric correction technique, as applied, can produce comparable classification accuracies to those obtained using conventional relative radiance training. The technology exists for further refinement of the technique if the limit of classification accuracy imposed by natural spectral variation is not reached. Field studies indicate that while natural signature variability is a problem, the means of identifying sources of variation offered by *in situ* reflectance measurement may allow refinements in sampling and choice of season for data analysis to improve categorization accuracy and utility. Specifically, assessment of green biomass for *S. alterniflora* appears to be possible using ratioed Band 7 and Band 5 reflectances. Most effective species discrimination may result from minimizing intraspecific variation in biomass and growth morphology by choosing early growing season data for analysis.

1.5 Analysis of Effects of Offshore Development on Coastal Land Use in the Kenai Region, Alaska

Interpretation of remote sensor data is a valid and valuable technique for evaluating onshore impacts of offshore petrochemical development. There are, however, limitations inherent to the use of such information.

High-altitude aircraft photography can be used to document specific land use and land cover types indicative of petrochemical development. It can also be used to monitor and define land use and land cover changes resulting from petrochemical development.

Similarly, Landsat imagery can be used to document land use types and changes, but from more generalized categories and to a more limited degree. Results of other studies on computerized classification of digital data from the Landsat multispectral scanner (MSS) indicate, however, that this type of remote sensing platform can provide almost as much detail as the aircraft photography when used in frontier areas such as Kenai.

The primary deficiency in the use of remotely sensed data occurs in areas where petrochemical development is proceeding both onshore and offshore. In such cases the designation of specific land uses as either onshore-related impact or offshore-related impact is virtually impossible. This separation becomes practical however, when additional data such as population, labor, resource development and similar statistics are analyzed in concert with remotely sensed data.

In summary, conventional remote sensing technology provides excellent information for analysis of types and locations of land changes which result from offshore oil and gas development. The disadvantage to the use of this information is its inability to identify the functional relationships of many land use and land cover types. Visual analysis of Landsat imagery provides an update capability which is often not available through conventional means but which is limited to general classification of land use categories. Results reported by Ellefsen (1974) suggest that better results can be achieved through automated analysis of Landsat digital data.

II. DENSITY FRONTS AND THEIR EFFECTS ON COASTAL POLLUTANTS

2.0 Introduction

Estuaries are the zones of transition between rivers and the sea.* As such they are subject to a number of sources of environmental stress: industrial thermal and waste discharges, sewerage inputs from the great and small coastal cities, and spills of oil and other materials associated with the world's maritime transport. At the same time estuaries serve as spawning and nursery grounds for many important species of fish and shellfish, as well as being the conduits through which nutrients pass into productive coastal waters. It is, therefore, important that we understand and be able to model the estuarine processes controlling the dispersal of pollutants floating on the surface as well as those suspended or dissolved in the water column.

Current estuarine chemistry and pollution studies are based on classical notions of estuarine circulation. The classical picture of circulation in a partially mixed estuary which has been brought to a state of quantitative understanding by the work of Pritchard (1952) and others, has been reviewed by Dyer (1972). This classical picture is one in which dilute sea water moving up the bottom of the estuary is mixed and advected upward into an upper layer of relatively fresh water moving downstream. It is two-dimensional (axial and vertical) in its essential factors. Salinity variations and flows in the transverse direction are viewed as effects of minor dimensional scheme. Moreover, the classical picture is one in which the dynamical quantities vary smoothly in the horizontal plane.

---

*"An estuary is a semi-enclosed coastal body of water which has a free connection with the open sea and within which sea water is measurably diluted with fresh water from land drainage." (Pritchard, 1952).

Remote sensors mounted on aircraft or satellites are now capable of providing a synoptic view of surface and near-surface water conditions in real time over large coastal areas. Useful results have been obtained in estuarine circulation studies, particularly when aircraft or satellites have been combined with boats gathering water samples and making other measurements as the remote sensors view the scene from above. Remotely tracked dyes and drogues have been used to trace currents. In coastal waters remote sensors benefit significantly from naturally occurring tracers, such as suspended sediment, or color differences between water masses.

In Delaware Bay one can observe a variety of tide lines, color fronts, foam lines, shear boundaries, etc., some of which seem random while others appear repeatedly in the same general location. These observations, together with boat-based field work lead one to severely question the simplicity of the classical view of estuarine circulation described above, particularly its assumption of smooth horizontal variations. It is clear from our work that regions with extremely strong transverse gradients of velocity and density exist in estuaries and that these regions play an important role in the dynamical and chemical processes of the system. These regions are called "fronts".

Fronts are a major hydrographic feature in Delaware Bay and other estuaries. Horizontal salinity gradients of four parts per thousand in one meter have been observed and convergence velocities of the order of 0.1 m/sec are typical (Kupferman et al., 1973). Often, fronts extend for tens of miles; generally parallel to the axis of the Bay's channels. They are observed on both sides of the Bay and along every channel where we have looked for them. Fronts have also been observed near the mouth of the Bay where they appear to be associated with the tidal interaction of shelf and estuarine water.

Aquatic fronts are somewhat similar to atmospheric fronts in that the denser fluid tends to under-ride the lighter fluid giving rise to an inclined interface. This dynamical behavior produces a marked surface convergence. In our investigations in Delaware Bay, we have observed that these convergences result in the concentration of foam, surface films and oil slicks at fronts.

Surface films and their resulting coalescence as foam lines are a complex mixture of organic and metallic compounds which are orders of magnitude more concentrated in pollutants than their underlying waters. The organic portion of these materials is made up of both natural and anthropogenic compounds, including a host of hydrocarbons, fatty acids, alcohols, and even pthalates (Garrett, 1967; Szekielda et al., 1972). Of the nine metals which federal agencies list as toxic to marine and estuarine organisms (FWPCA, 1968; NAS-NRC, 1975) at least seven are found concentrated in surface films. Barker et al. (1972) determined that zinc and copper could concentrate by factors of ten to a hundred in surface microlayers compared to underlying Hawaiian water. Szekielda et al. (1972) found that when such microlayers were collapsed into foam lines along estuarine fronts, metal enrichment thousands of times greater than the original values could result for chromium, copper, lead, mercury, silver, and zinc. These workers showed that phytoplankton chlorophyll also collects along such boundaries, and is carried down into the water column by the down-welling convergence.

Therefore no serious effort to model the circulation dynamics and pollutant transport in Delaware Bay and similar estuaries should neglect the effect of frontal systems. The purpose of this section is to demonstrate how remote sensing techniques have been used to establish the location, frequency of occurrence, extent, movement, shear and convergence properties of coastal fronts and their effect on certain pollutants, such as oil slicks.

2.1 Description of the Delaware Estuarine System

The physical oceanography and morphology of the Delaware Estuary have been reviewed by Polis and Kupferman (1973). There is some terminological confusion about what constitutes the Delaware Estuary with various authors using discordant definitions. Polis and Kupferman established a convenient nomenclature for the Delaware system. The following terms provide a fixed geographic basis for discussion:

Delaware Estuary: The entire water area from Capes May and Henlopen to Trenton (the head of tide, see Figure 2.1).

Delaware Bay: The water area from Capes May and Henlopen to a line between the stone markers at Liston Point, Delaware and Hope Creek, New Jersey.

Tidal River: The portion of the Delaware Estuary above the Delaware Bay.

The following terms are based on dynamical considerations and are more useful for physical oceanographic discussions:

Lower Estuary: That portion of the Delaware Estuary to the furthest upstream influence of oceanic salinity. This upstream limit is defined as the point where the chloride content of the water drops below 250 parts per million. Chloride is the ion found in greatest concentration in sea water. 600 ppm chloride is the commonly accepted maximum for potable water. The location at which this chloride level is found varies with river flow and tidal stage. It is normally found in the region between Wilmington and Philadelphia.

Upper Estuary: That portion of the Delaware Estuary upstream of the Lower Estuary.

The estuary has an overall length of 213 km. Delaware Bay proper has a length of approximately 76 km, a maximum width of 49 km and a maximum depth of 46 m below mean low water. Its mean depth is approximately 10.4 m. The bottom topography is characterized by alternate shoals and fingers of deep water, especially on the Delaware side of the bay, as can be seen in Figure 2.2. This topography is intimately related to the generation of fronts.

2.2 Oceanography of Estuarine Fronts

From the oceanographic point of view, estuarine fronts represent the surface expression of regions of extremely high gradient (verging on discontinuity) in various parameters of physical interest, the most important of these being the velocity and density fields. Indeed, this characterization may well be taken as the oceanographic definition of a front.

In Delaware Bay, surface and water column observations tend to show a pattern in the relationship between the time of occurrence in terms of tidal current phase and the geographical location of the front. Flood associated fronts are more prominent on the New Jersey side of the Bay while fronts in the deeper channels of the Delaware side are most frequent during the ebb portion of the tidal cycle. The occurrence of flood associated fronts on the New Jersey side coupled with their absence on the Delaware side may be explained in some measure by the action of Coriolis force. This causes the New Jersey side to have a larger tidal range and its channels to have unusually strong flood currents (Polis et al., 1973).

The focus of detailed kinematic and dynamical studies has, however, been on the Delaware side where interest (and funding) has been drawn by extensive oil lightering operation. What follows is based upon the preliminary analysis of a number of experiments conducted by the authors in deep channels of Delaware Bay.

An examination of low altitude aerial photographs reveals that some fronts are associated with a foam line (Figure 2.3) while others have their visual manifestation in a sharp color boundary unassociated with a foam line (Figure 2.4). Often, foam and color boundaries are found parallel to each other, but separated by a few meters as shown in Figure 2.5. The foam found in some fronts is generally associated with lines of detrital material, predominantly marsh grass fragments, but these detrital lines are often displaced from the foam toward the paralleling color boundary. All of this was taken as presumptive evidence of a convergence; however, the displacement of foam (surface), detrital (near surface--upper 2-3 mm) and color (bulk) boundaries argue for the distortion or stretching of the convergence zone in the surface boundary layer as shown in Figure 2.6. From our first encounters with fronts, we had known that they were associated with extremely strong salinity, and hence density, differences (Szekielda et al., 1972). Figure 2.6 therefore shows the convergence being associated with a density interface. For reasons of continuity it is necessary that, except at the exact surface (marked by the foam line), the density interface be below the line of convergence.

Given this picture of the foam marked boundaries, we had assumed that the foamless color boundaries were essentially incipient zones of convergence which had not yet had time to collect noticeable foam and detritus. As will be seen below we now have reason to abandon, or at least to severely modify, this interpretation.

Our assumption of convergence associated with the fronts was confirmed by experiments using anchored and drifting dye packets which showed that one front on the Delaware side had a convergence velocity with respect to the frontal interface of 12 cm/sec while the interface moved laterally at the rate of 54 cm/sec so that the lateral current component was 66 cm/sec on

the back side of the advancing front. These results were reported by Kupferman et al. (1973).

In October 1974, an experiment was undertaken to attempt to understand the intratidal cycle dynamics of the deep channel in Delaware Bay. During the course of that experiment, a front passed a station occupied by one of the boats in that experiment (Station S in Figure 2.7). Figure 2.8 shows the isohalines as a function of time and depth. From this it is clear that the frontal structure does not extend to the bottom of the channel in general, but more important, that it is associated with the normal estuarine pycnocline (region of high vertical density gradient) generally ascribed the two-layered estuarine circulation.

In an experiment conducted in January 1975, the three dimensional structure of a complex frontal system in this same region was mapped out. For the purposes of this paper it will suffice to show a pair of cross channel sections of the frontal system as manifested in its lateral velocity structure. The cross-channel velocity component, v_y, is taken as positive toward the Delaware shore. Figures 2.9 and 2.10 show isotachs of v_y in a cross-channel section looking upstream through Stations Wo-1, Wo-2, and Wo-3 (see Figure 2.7 for station locations) at 1115 and 1340 hours respectively. As these stations were occupied successively by the R.V. Wolverine, the vertical structure for Stations Wo-1 and Wo-2 are based on temporal interpolations of earlier and later observations; however, the sections seem to be consistent with all available data. It will be noticed (1) that there are both zones of convergence and of divergence, and (2) that the entire structure appears to be migrating toward the New Jersey shore. This is borne out by the aerial photographs taken as a part of this experiment. Upon close examination the photographs also show a color boundary

associated with the divergence on the right. The divergence on the left apparently had no clear visual manifestation. Thus it now appears that the color boundaries lacking foam may be associated with divergences. The photographs also show another foam line outside (to the left) of Station Wo-1. Thus we have in this channel at least two divergences and two convergences. All of these observations were taken on the ebb portion of the tidal cycle.

On the flood portion of the cycle, the fronts on the Delaware side of the Bay break up. Thus while there still exist weak color boundaries on the scale seen by LANDSAT, surface observations indicate a very patchy and disorganized picture in the upper few meters of the water column. Thus it appears from boat observations that the long, linear frontal structures generated on ebb tide in this region degenerate into meanders, eddies or lenses of lighter water which become largely mixed into a vertically homogeneous water column by the end of the flood, as shown in Figure 2.8.

2.3 Effect of Fronts on Oil Slick Movement

Approximately 70 percent of all the oil that is delivered to the east coast of the United States moves by water up the Delaware Bay and River. Much of this oil is transferred from large deep-draft tankers to barges (lighters) or to small tankers to reduce the draft of the large tankers and allow navigation up the Bay and River for unloading at docks. This transfer operation takes place within Delaware Bay in the anchorage area off Big Stone Beach (see Figure 2.1). In a typical year, more than 50 million short tons of crude petroleum are transported through the Bay using the Big Stone anchorage area within the bay (Wang et al., 1976).

Due to the growing demand for imported oil, the oil transport through Delaware Bay and transfer activities in the Bay are expected to increase

markedly in the future. Oil extracted from the outer continental shelf may also increase the transfer activities in the region. National and regional concern over such development focuses in large measure on environmental vulnerability due to oil spills. Central to environmental repercussions, facility development, and clean-up operations, is information regarding the physical movement and distribution of an oil spill.

A computer simulation model has been developed for tracing oil spills in the Delaware Bay (Wang et al., 1976). The model takes into account two aspects of transport: drifting and spreading. The modeling of drift is based on the fact that oil on water drifts under the combined influence of water current, wind effects, and the earth's rotation. The physical processes governing the spreading of the slick are divided into three stages. In the initial stage, the spreading is predominantly governed by the balance of the forces of gravity and inertia. In the second stage, the spreading involves the balance of viscous and inertial forces. In the third and final stage of the spreading, a turbulent diffusion model is employed. Based on these processes and the approximation of radial symmetry, the rate of spreading is computed.

The input requirements include the boundary conditions (the geometry and bottom topography), the tidal current, the wind conditions, and the nature of the oil spill - viz., the size of the spill, location of the initial spill and the nature of the oil. Historical tidal current information and present wind conditions in the Delaware Bay region are now being used as input.

The wind conditions can be entered into the model in either of two ways: either deterministically, or stochastically to make Monte Carlo calculations based on historical wind data. The first way is used in an

oil tracking routine, while the second yields information on the probability of various oil spill distributions.

The interactive nature of the model allows for information transfer between the computer and the users who may or may not be familiar with computer programming. The details of oil spill tracking are displayed on a television-type screen. A number of output options are available.

In order to verify and improve the model, aircraft and boats were used to track actual oil slicks under various conditions of wind, current, waves, etc. During these field verification exercises it became obvious that by capturing and holding oil slicks, frontal systems significantly influence the dynamic behavior of oil slicks in Delaware Bay. The tendency of oil slicks to line up along fronts during certain parts of tidal cycle was illustrated by an oil spill which occurred as a result of a lightering operation in the anchorage area on 10 January 1975, at the same time as the data shown in Figures 2.9 and 2.10 were obtained. As shown in Figure 2.11, at 0950 hours the spill consisted of four large slicks and numerous smaller ones almost randomly dispersed throughout the area. The wind was about 10 knots from the east-southeast. The flood tide cycle was coming to an end with a near slack current, as measured with current meters and air-tracked small drogues. At this time no boundaries were observed. As shown in Figure 2.12 by 1100 hours the current had turned to the ebb direction with a velocity of 0.6 knots. Two convergent boundaries were clearly visible on either side of the oil slicks and were starting to attract some of the slicks. Results of an oceanographic study of these boundaries were discussed in the previous section and the right boundary corresponds to the convergence BB in Figures 2.9 and 2.10. Changing to a smaller scale (higher altitude photography) one can see from Figure 2.13 that by 1500 hours most of the oil was aligned along the boundaries and stretched into two five-mile long slicks.

2.4 Mapping Fronts with Satellites

In order to modify the predictive model to include the effect of fronts on oil slick movement, one must determine the location of fronts in the Bay and their relationship to the tidal cycle. Aircraft have been most useful in finding fronts, photographing them, and guiding boats to collect data in frontal zones. However, to map the extent and repeatability of fronts over the entire bay under different tidal conditions, satellite imagery is more effective. Imagery and digital tapes from thirty-six passes over Delaware Bay of the Landsat-1 and Landsat-2 satellites were used in our work. The Landsat imagery was produced by the four-channel multispectral scanner (MSS) having the following bands:

Band 4	0.5-0.6 Microns
Band 5	0.6-0.7 Microns
Band 6	0.7-0.8 Microns
Band 7	0.8-1.1 Microns

From an altitude of 920 km, each frame covered an area of 185 km by 185 km and had a linear resolution of about 80 meters. In addition to the nine-track 800 bpi magnetic tapes, reconstructed negative and positive transparencies in 70 millimeter format and prints in nine-inch format were obtained from NASA. Before visual interpretation, some of the imagery was enhanced optically, using density slicing and color additive techniques. Annotated thematic maps were prepared by computer analysis of digital tapes and by direct photo-interpretation of the transparencies reconstructed by NASA (Klemas et al., 1974). Landsat image radiance of Band 5 was also correlated with suspended sediment concentration and Secchi depth data obtained from boats and helicopters during the satellite overpasses (Klemas et al., 1972). A suspended sediment concentration map based on Landsat image radiance correlation with water sample analyses is shown in Figure 2.14.

Figures 2.15 and 2.16 contain Landsat pictures and NOAA-NOS tidal current charts for Delaware Bay. Only MSS Band 5 images are shown, since this "red" band was found to give the best contrast in delineating suspended sediment concentration in the upper one meter of the water column. Each LANDSAT picture is matched to the nearest predicted tidal current chart within ±30 minutes. The current charts indicate the hourly directions by arrow, and the velocities of the tidal currents in knots. The Coast and Geodetic Survey made observations of the current from the surface to a maximum depth of 20 feet in compiling these charts (National Ocean Survey, 1972). The current magnitudes shown on the charts are somewhat higher than mean and need to be scaled down as explained in the introduction to the charts (National Ocean Survey, 1960).

The satellite picture in Fig. 2.15 was taken on October 10, 1973, two hours after maximum flood at the entrance of Delaware Bay. Masses of highly turbid water are visible around the shoals near the mouth of the bay and in the shallow areas on both sides of the bay. Since at that time strong currents and considerable waves were prevailing in most of the bay, some of the sediment in suspension seems to be locally generated over shoals and shallow areas of the bay resulting in a higher degree of backscatter from shallower waters. During flood tide at the mouth of the bay, considerable correlation was found between the depth profile and image radiance, even though the water depth exceeded the Secchi depth by at least a factor of three in all areas. Maximum velocity of flood currents is occurring in the upper portion of the bay, where sharp boundaries parallel to edges of the deep channel can be seen. The boundaries are visible in the satellite imagery primarily because water masses near the shore appear more turbid than the water in the middle of the river. The distinctness of the

boundaries implies a strong gradient in suspended sediment concentration across the boundary. The direction and shape suggest that shear is present. Unfortunately the spatial resolution of the Landsat scanner is too poor to determine whether these boundaries are capped by foam, which would indicate lateral convergence. An aircraft photograph of a similar frontal system is shown in Figure 2.17.

The satellite overpass on February 13, 1973, occurred about one hour after maximum ebb at the mouth of Delaware Bay. The corresponding Landsat image and predicted tidal currents are shown in Figure 2.16. Strong sediment transport out of the bay in the upper portion of the water column is clearly visible, with some of the plumes extending up to 20 miles out of the bay. Small sediment plumes along New Jersey's coast clearly indicate that the direction of the nearshore current at that time was towards the north. The image in Figure 2.16 contains good examples of tidal fronts and flow-lines. In particular, note the sharp demarcation of the tidal plumes at the mouth of Delaware Bay. Strong gradients in suspended sediment concentration can be seen across these fronts with gradients in density, salinity and occasionally temperature likely.

In order to determine where in the bay fronts tend to form during different portions of the tidal cycle, thirty-six Landsat images such as the ones shown in Figures 2.15 and 2.16 were analyzed. Note that each satellite image was obtained on a different day. The tidal conditions in each satellite image were matched to one of the twelve U. S. Coast and Geodetic Survey tidal current charts, where each chart represents current conditions in Delaware Bay during a one-hour segment of the tidal cycle. Thus an average of three satellite images were associated with each of the twelve current charts. As shown in Figures 2.18 through 2.29, the fronts discerned in each image were superimposed on the appropriate tidal current chart.

The identification of fronts was based primarily on strong turbidity gradients or discontinuities mainfested by changes in image grey tone. As discussed in a previous section, some of the fronts are likely to have foam lines, temperature gradients and salinity gradients associated with them. Foam lines, which can be mapped from aircraft, are too thin to be resolved by Landsat. Temperature and salinity gradient monitoring would require different sensors than those presently on Landsat. The increased spatial resolution and spectral range of the Thematic Mapper being developed by NASA for Landsat follow-on missions for the 1980-90 time period (NAS-NRC, 1976) would significantly improve the identification of coastal fronts.

Two types of boundaries were distinguished -- "strong" and "weak", depending on the magnitude of the turbidity gradient or discontinuity. The strong boundaries not only contain strong gradients but also are likely to exhibit considerable shear. The "weak" boundaries are either strong boundaries whose contrast has been degraded by atmospheric effects; or convergent boundaries observed during their formative or decaying states; or divergent boundaries and, in a few cases, edges of river plumes.

The formation and decay of ebb-associated fronts on the Delaware side of the bay, particularly the lightering area, is illustrated in Figures 2.24 through 2.29. The mapped behavior of the fronts in this area agrees with model predictions and boat observations (Kupferman et al., 1973). Surface and water column observations tend to show a pattern in the relationship between the time of occurrence in terms of tidal current phase and the geographical location of the front, with flood-associated fronts being more prominent on the New Jersey side of the bay, while the fronts in the deeper channels of the Delaware side are more frequent during the

ebb portion of the tidal cycle. The occurrence of flood-associated fronts such as shown in Figures 2.18 through 2.23 on the New Jersey side, coupled with their frequent absence on the Delaware side, may be explained in some measure by the action of Coriolis force. This causes the New Jersey side to have a larger tidal range and its channels to have unusually strong flood currents. As predicted, the formation of flood-associated fronts on the New Jersey side of the bay is shown in Figures 2.18 through 2.23.

The twelve charts containing current velocities and boundaries shown in Figure 2.18 through 2.29 are presently being used to establish locations where boundaries tend to prevail. A subroutine is being developed for the oil slick movement model to handle oil slicks that enter these front-infested areas. The subroutine will include dynamic effects, such as shear currents, at a finer scale. At the present time Landsat appears to offer the most effective means of identifying front-infested areas, i.e. where fronts tend to form, how extensive they are, how long they prevail, how much they move about, and how strong and abrupt their gradients are.

2.5 Conclusions

Imagery from Landsat-1 and Landsat-2 proved valuable in mapping the location, type and extent of estuarine fronts over all portions of the tidal cycle. Satellite observations of flood-associated fronts on the New Jersey side of the Bay and ebb-associated fronts on the Delaware side, where studies were being conducted, agreed with boat measurements and model predictions. Since estuarine fronts influence the movement of oil slicks and the dispersion of other pollutants, clean-up operations depending on the use of oil slick drift prediction models will benefit from aircraft tracking the actual slicks and from Landsat observations of surface currents and frontal systems. Neither ships nor aircraft alone were as effective in providing a complete, synoptic and repetitive overview as did the satellite.

2.6 References

Barker, D. R., H. Zeithlin and R. A. Duce. (1972) Metal ion concentrations in sea surface microlayer and size-separated atmospheric aerosol samples in Hawaii. J. Geophys. Res. 77: 5076-5086.

Dyer, K. R. (1972) Estuaries: A Physical Introduction. John Wiley and Sons, New York.

Federal Water Pollution Control Administration. (1968) Water Quality Criteria. Washington, D.C.

Garrett, W. S. (1967) Deep Sea Res. 14: 221.

Klemas, V., D. Bartlett, W. Philpot, and R. Rogers. (1974) Coastal and estuarine studies with ERTS-1 and Skylab. Remote Sens. Environ. 3: 153-174.

Klemas, V., M. Otley, W. Philpot and R. Rogers. (1974) Correlation of coastal water turbidity and circulation with ERTS-1 and Skylab imagery. Proc. 9th Internatl. Symp. on Remote Sens. Environ., Ann Arbor, Mich.

Kupferman, S. L., V. Klemas, D. F. Polis and K. H. Szekielda. (1973) Dynamics of aquatic frontal systems in Delaware Bay (Abstract). Trans. AGU 54: 302.

Mairs, R. L. and D. K. Clark. (1973) Remote sensing of estuarine circulation dynamics. Photogram. Eng. 39(9): 927-938.

NAS-NRC, Commission on Natural Resources, Ocean Affairs Board. (1975) Assessing potential ocean pollutants. Rept. of Study Panel on Assessing Potential Ocean Pollutants, Natl. Acad. of Sci., Washington, D.C.

NAS-NRC, Commission on Natural Resources. (1976) Resource and environmental surveys from space with the thematic mapper in the 1980's. A report prepared by the Comm. on Remote Sens. Programs for Earth Resource Surveys, Natl. Acad. of Sci., Washington, D.C.

National Ocean Survey. (1960) Tidal current charts - Delaware Bay River. Environ. Sci. Serv. Admin., 2nd ed., U. S. Dept. Commerce.

National Ocean Survey. (1972, 1973) Tidal current tables, Atlantic coast of North America. Natl. Oceanic and Atmos. Admin., U. S. Dept. Comm.

Polis, D. F. and S. L. Kupferman. (1973) Physical Oceanography. In: Vol. 4, Delaware Bay Rept. Series. D. F. Polis, ed. College of Marine Studies, Univ. Delaware.

Pritchard, D. W. (1952) Estuarine Hydrography. Advan. Geophy. 1: 243-280.

Shuster, C. N. (1959) A biological evaluation of the Delaware River estuary. Info. Series, Publ. No. 3, Univ. Delaware Marine Lab. Sept. 1959.

Szekielda, K.-H., S. L. Kupferman, V. Klemas and D. F. Polis. (1972) Element enrichment in organic films and foam associated with aquatic frontal systems. J. Geophys. Res. 77: 5278-5282.

Wang, H., J. R. Campbell and J. D. Pitmars. (1976) Computer modeling of oil drift and spreading in Delaware Bay. Univ. Delaware Rept. CMS-RANN-1-76, March 1976.

2.7 List of Figures

Figure 2.1: The Delaware Estuary.

Figure 2.2: Submerged contours of Delaware Bay. Tongues of deeper water radiante from the bay entrance into the bay.

Figure 2.3: Estuarine front with foam line photographed from an aircraft.

Figure 2.4: Estuarine front without foam line photographed from an aircraft at an approximate scale of 1:10,000 in the middle of the lower portion of the bay. Note the shear displacement of ship wakes as they cross the boundary.

Figure 2.5: Front with a displaced foam line photographed from an aircraft at a scale of about 1:20,000, eight kilometers outside the mouth of the bay.

Figure 2.6: Schematic diagram of a vertical section perpendicular to a frontal convergence zone. Note displacement of surface, near surface and main zones of convergence as marked by foam, detritus, and color lines respectively.

Figure 2.7: Station locations for boat observations of fronts October 1974 and January 1975.

Figure 2.8: Salinity in parts per thousand versus time and depth for station S, 1 October 1974. Dots indicate water samples taken. Note change from vertical homogeneity to stratification with frontal passage, also overturning during flood between 0715 and 0930 hours.

Figure 2.9: Isotachs of cross-channel velocity component, v_y, for a section looking up-bay at 1115 hours, 10 January 1975. Three lines of $v_y = 0$ are labeled AA, BB and CC. Of these, AA and CC represent regions of horizontal divergence while BB is the frontal convergence marked by a foam line.

Figure 2.10: Isotachs of cross-channel velocity component, v_y, for a section looking up-bay at 1340 hours, 10 January 1975. Lines AA, BB and CC are those similarly labeled in Figure 2.9; however, they are now deeper and further to the right as a result of the advance of the frontal system.

Figure 2.11: On 10 January 1975, the shown oil slick pattern was encountered at the oil lightering area in lower Delaware Bay. At 0950 hours flood tide currents were near slack and no boundaries were observed.

Figure 2.12: By 1100 hours the tidal currents assumed an ebb direction, and the oil slicks were attracted by convergent boundaries which had appeared around 1030 hours. Results of oceanographic investigations of these particular boundaries are shown in Figures 2.9 and 2.10.

Figure 2.13: A higher altitude view of the area shows most of the oil lined up in 5-mile long narrow slicks along the two boundaries.

Figure 2.14: Suspended sediment concentration map for Delaware Bay obtained by correlating Landsat imagery radiance values with water samples (Klemas et al., 1972).

Figure 2.15: Predicted tidal currents and Landsat-1 MSS Band 5 image of Delaware Bay obtained on 10 October 1972 (I.D. No. 1079-15133).

Figure 2.16: Predicted tidal currents and Landsat-1 MSS Band 5 image of Delaware Bay taken on 13 February 1973 (I.D. No. 1205-15141).

Figure 2.17: Estuarine front similar to that shown in Figure 15, photographed from an aircraft at a scale of 1:80,000 near Woodland Beach, Delaware. This frontal system is at least 6 km long, has an average distance of 2 km from the shoreline, and separates more turbid water near shore from the bay's clearer water.

Figures 2.18-2.29: Location and extent of frontal systems in Delaware Bay, derived from Landsat images such as Figure 2.15 and mapped on NOAA-NOS tidal current charts.

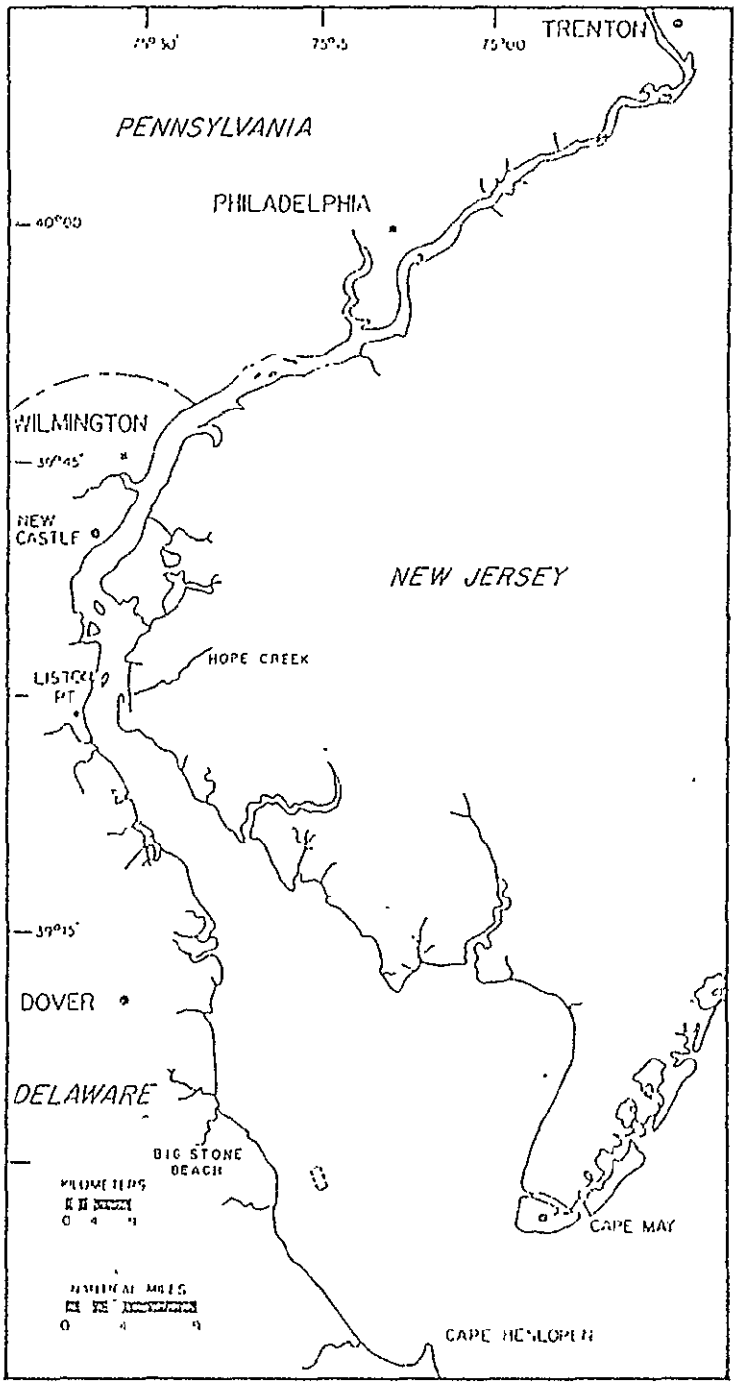

Figure 2.1 The Delaware Estuary

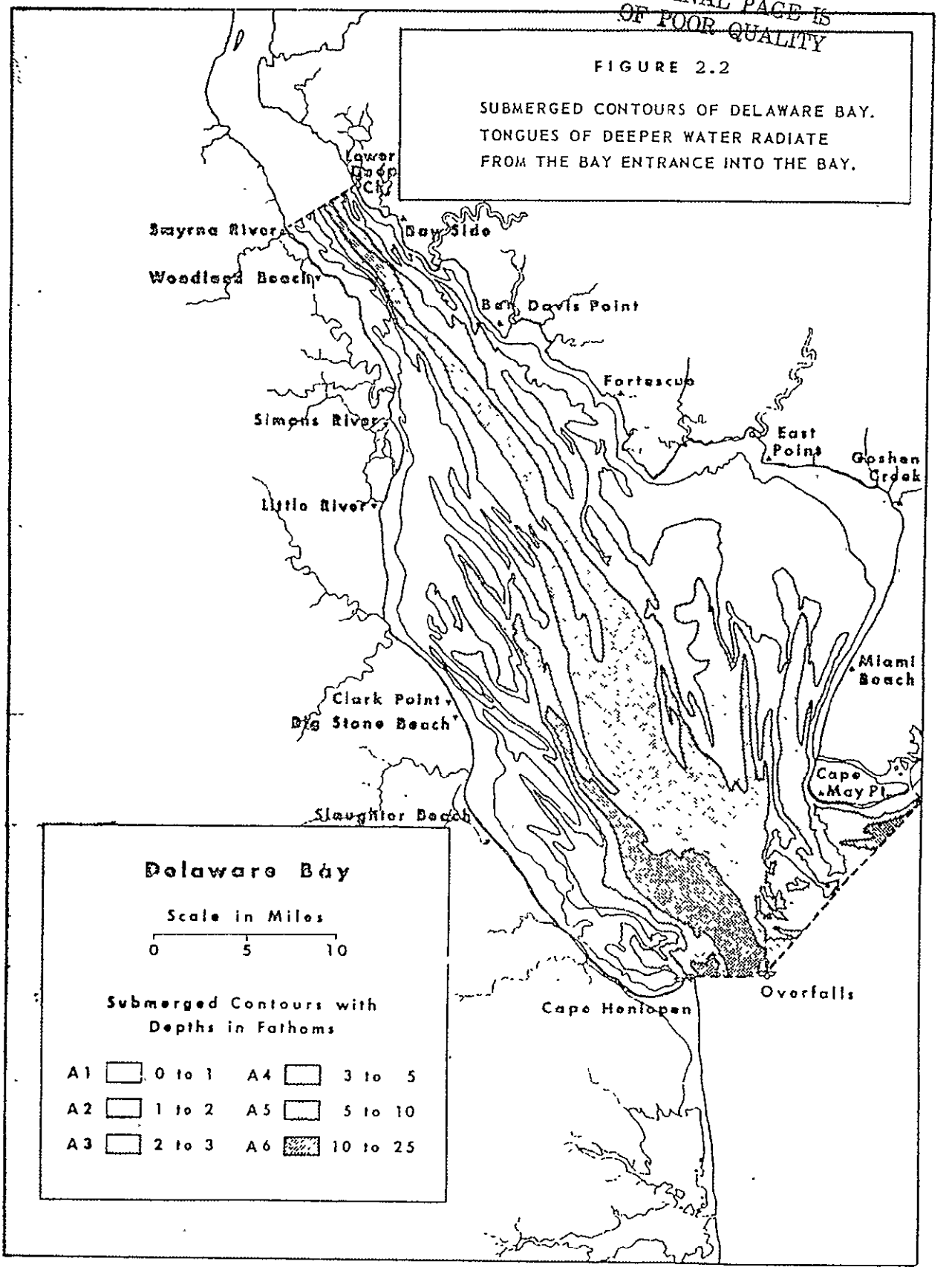

FIGURE 2.2

SUBMERGED CONTOURS OF DELAWARE BAY. TONGUES OF DEEPER WATER RADIATE FROM THE BAY ENTRANCE INTO THE BAY.

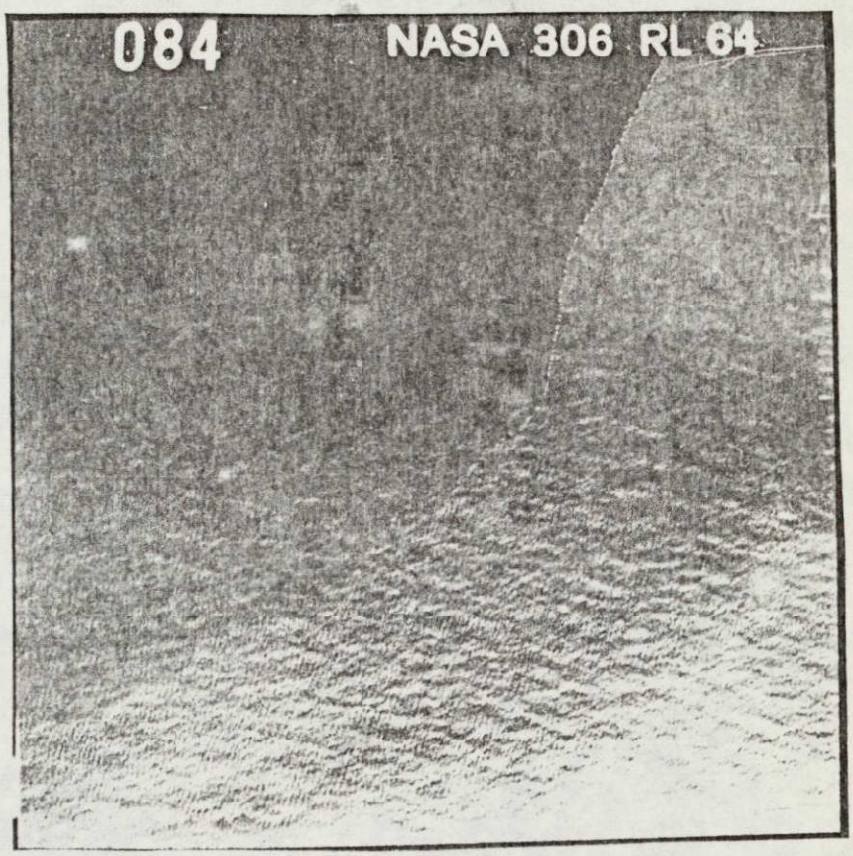

Figure 2.3. Estuarine front with foam line photographed from an aircraft.

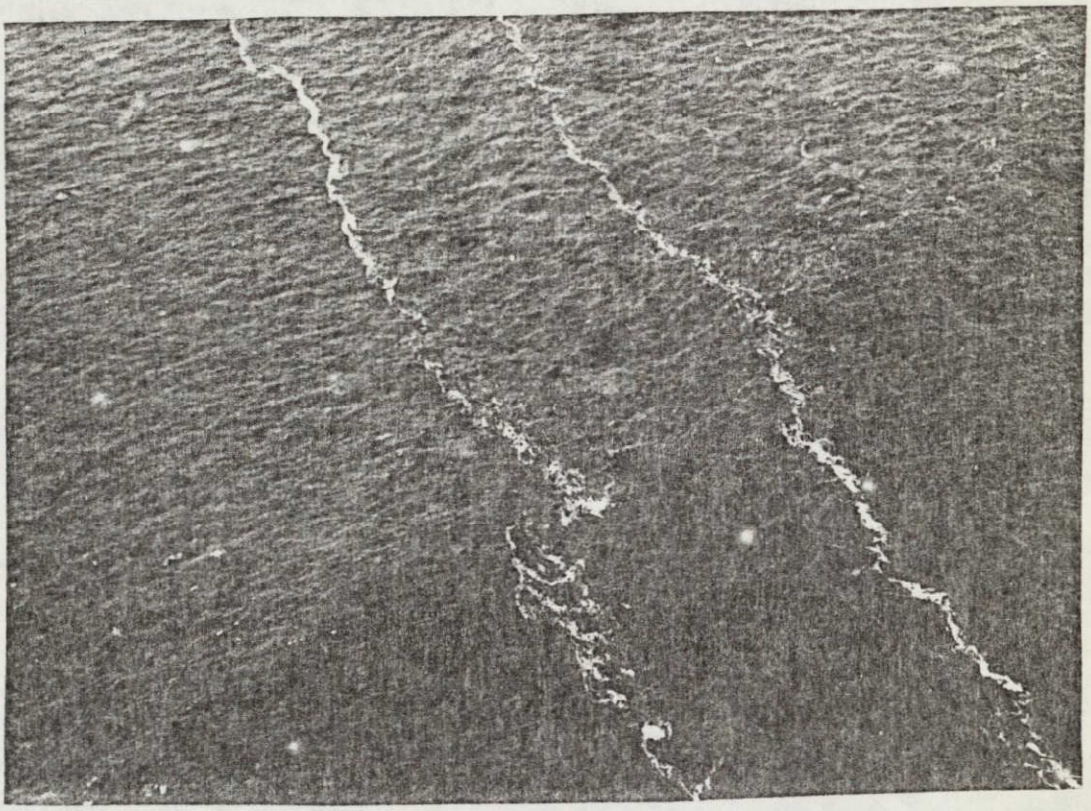

Figure 2.4. Estuarine front without foam line photographed from an aircraft at an approximate scale of 1:10,000 in the middle of the lower portion of the bay. Note the shear displacement of ship wakes as they cross the boundary.

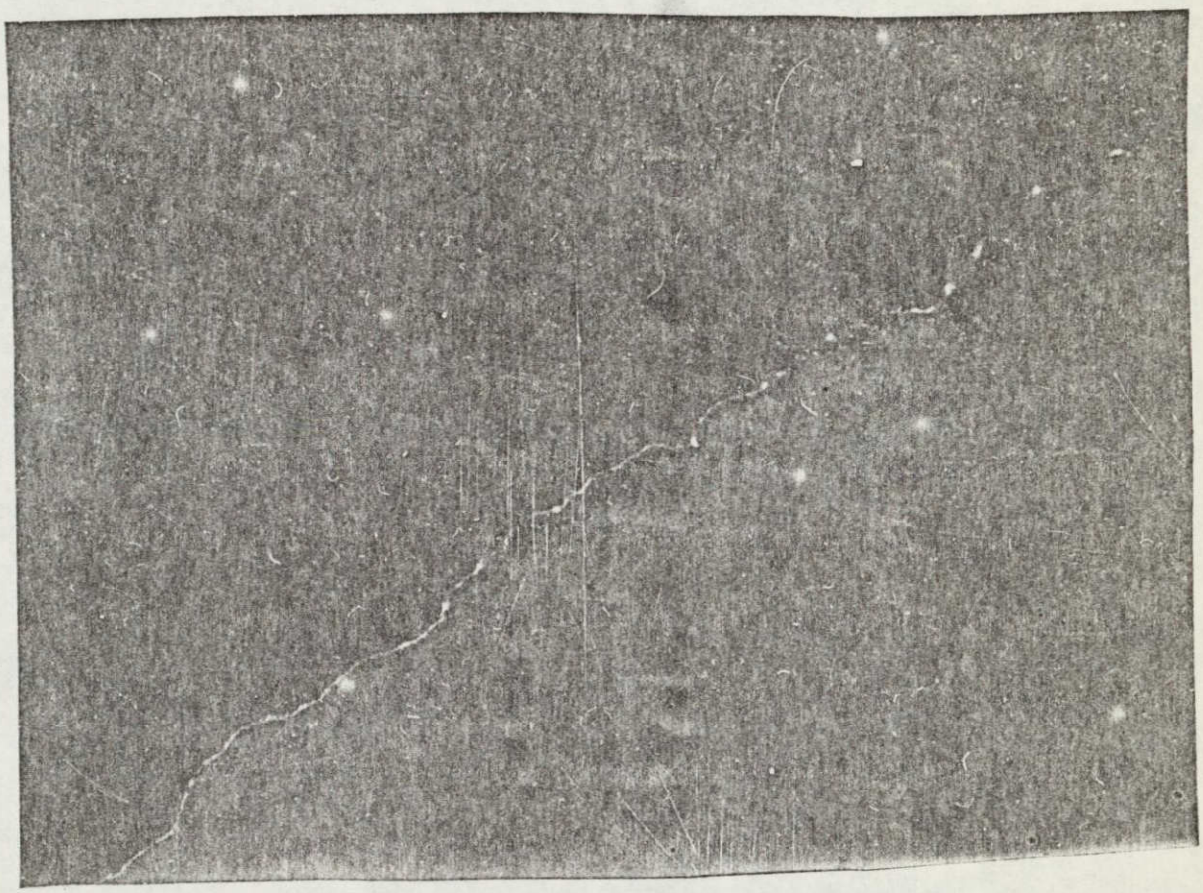

Figure 2.5. Front with a displaced foam line photographed from an aircraft at a scale of about 1:20,000, eight kilometers outside the mouth of the bay.

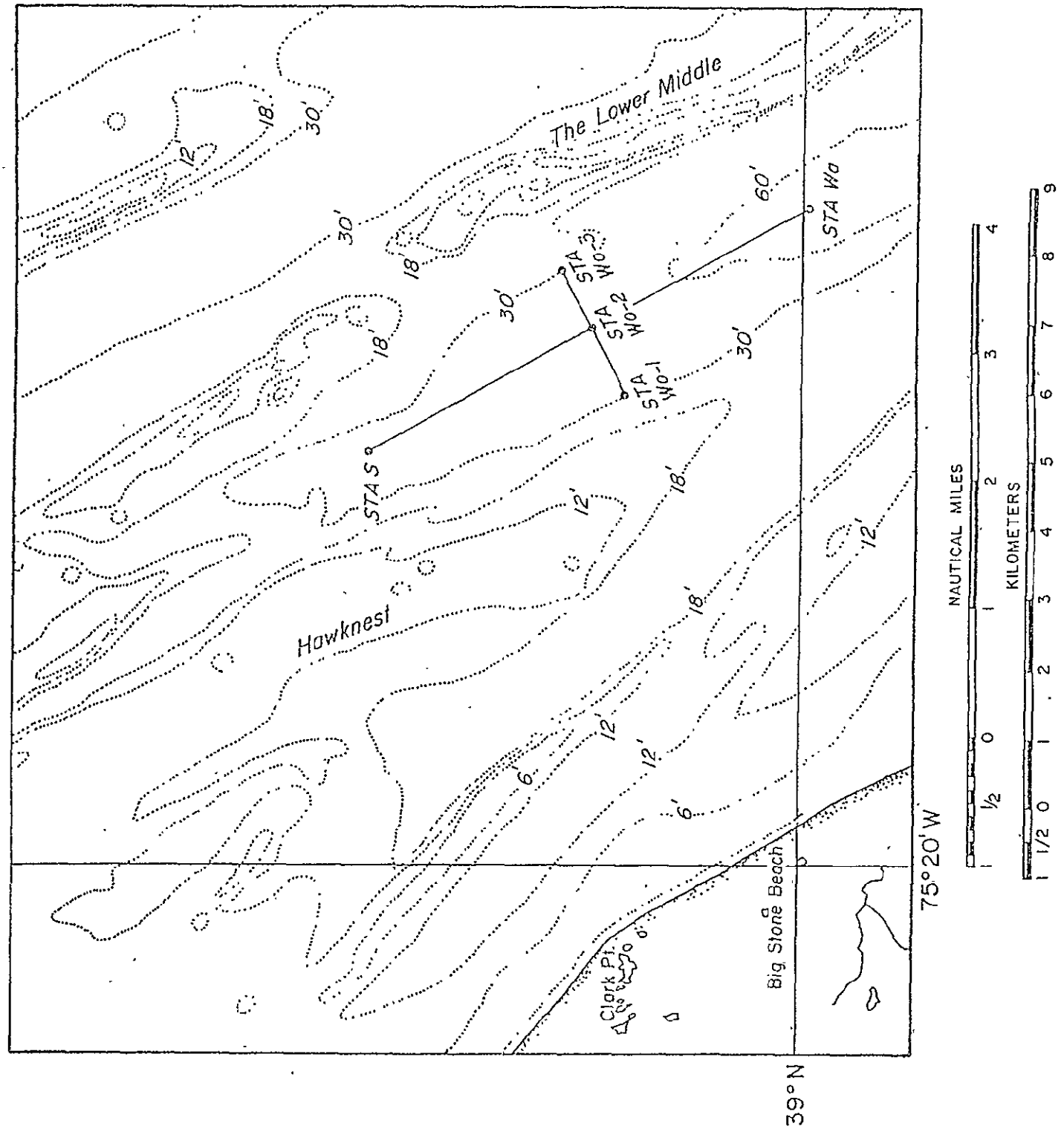

Figure 2.7 Station locations for boat observations of fronts October 1974 and January 1975.

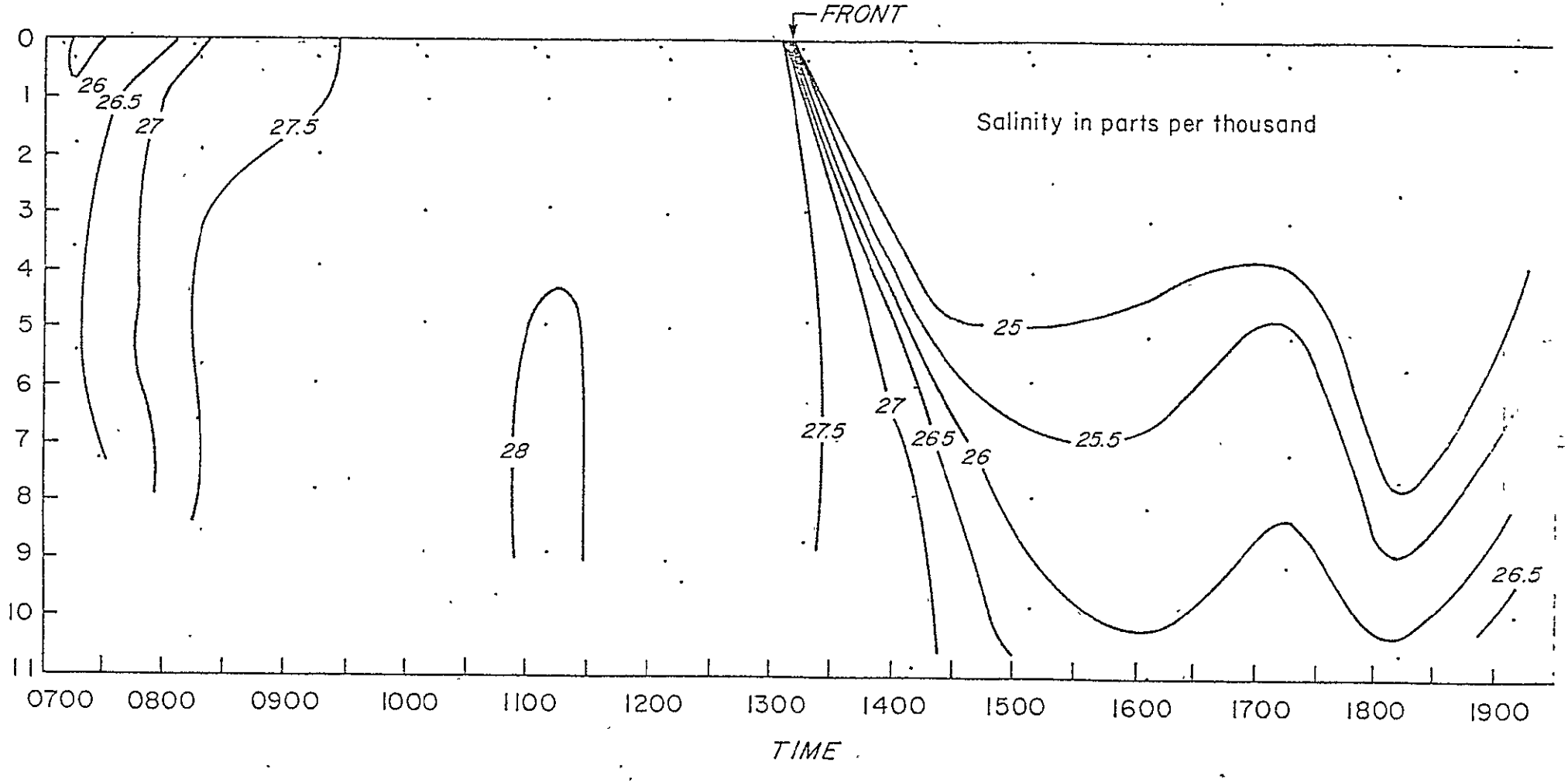

Figure 2.8 Salinity in parts per thousand versus time and depth for Station S, on 1 October 1974. Dots indicate water samples taken. Note change from vertical homogeneity to stratification with frontal passage, also overturning during flood between 0715 and 0930 hours.

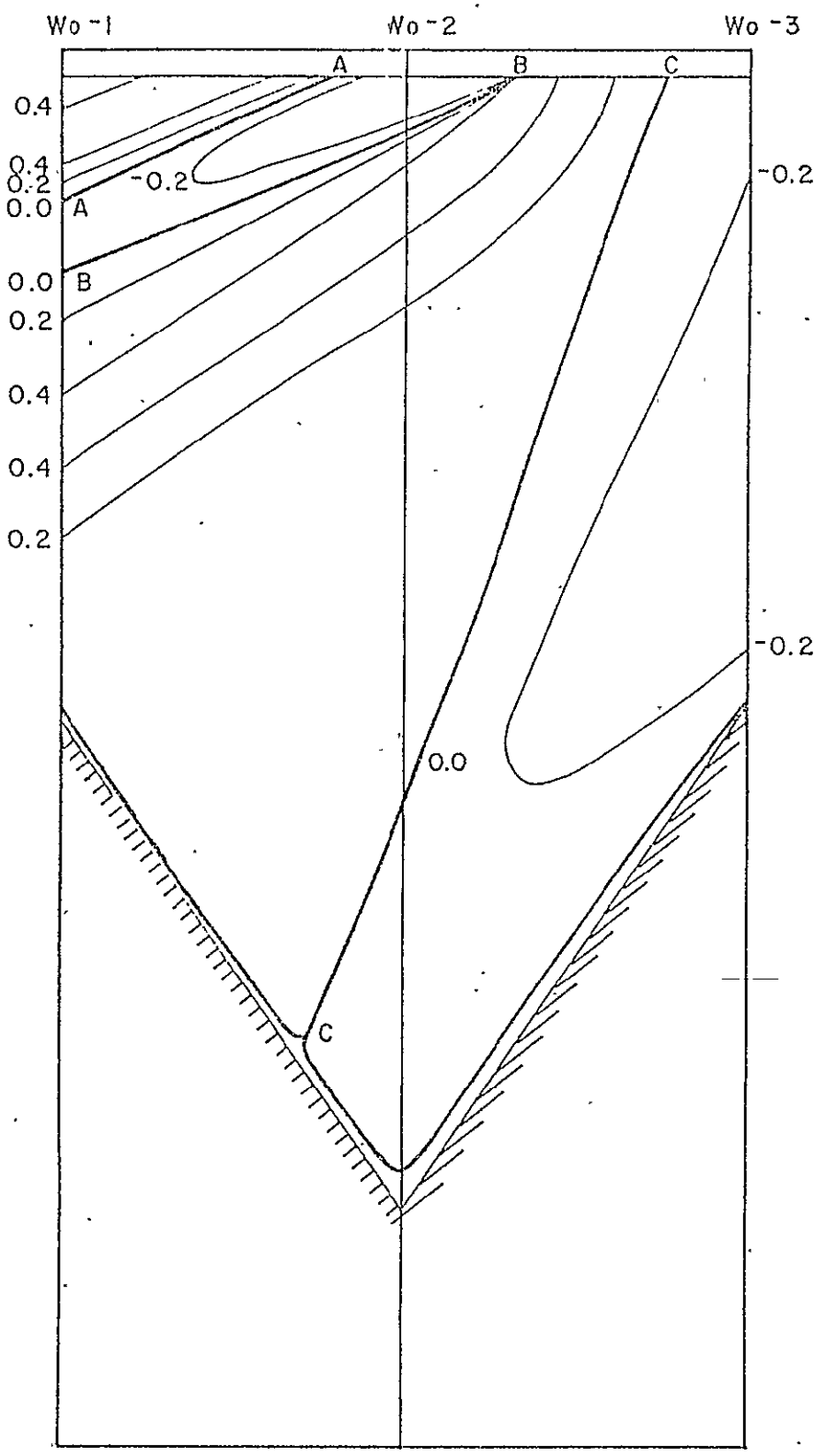

Figure 2.9 Isotachs of cross-channel velocity component, v_y, for a section looking up-bay at 1115 hours, 10 January 1975. Three lines of $v_y = 0$ are labeled AA, BB and CC. Of these, AA and CC represent regions of horizontal divergence, while BB is the frontal convergence marked by a foam line.

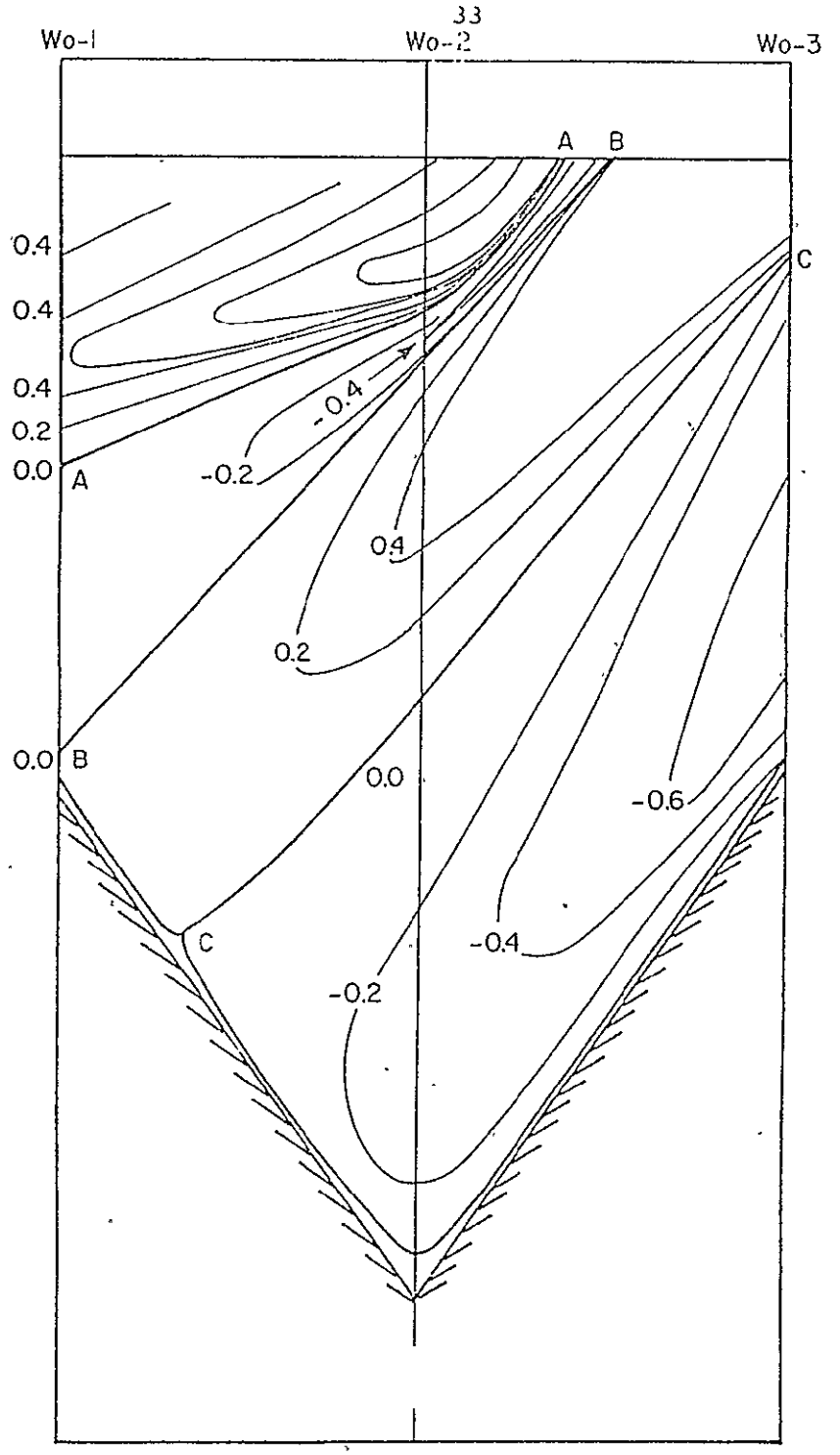

Figure 2.10 Isotachs of cross-channel velocity component, v_y, for a section looking up-bay at 1340 hours, 10 January 1975. Lines AA, BB and CC are those similarly labeled in Figure 9; however, they are now deeper and further to the right as a result of the advance of the frontal system.

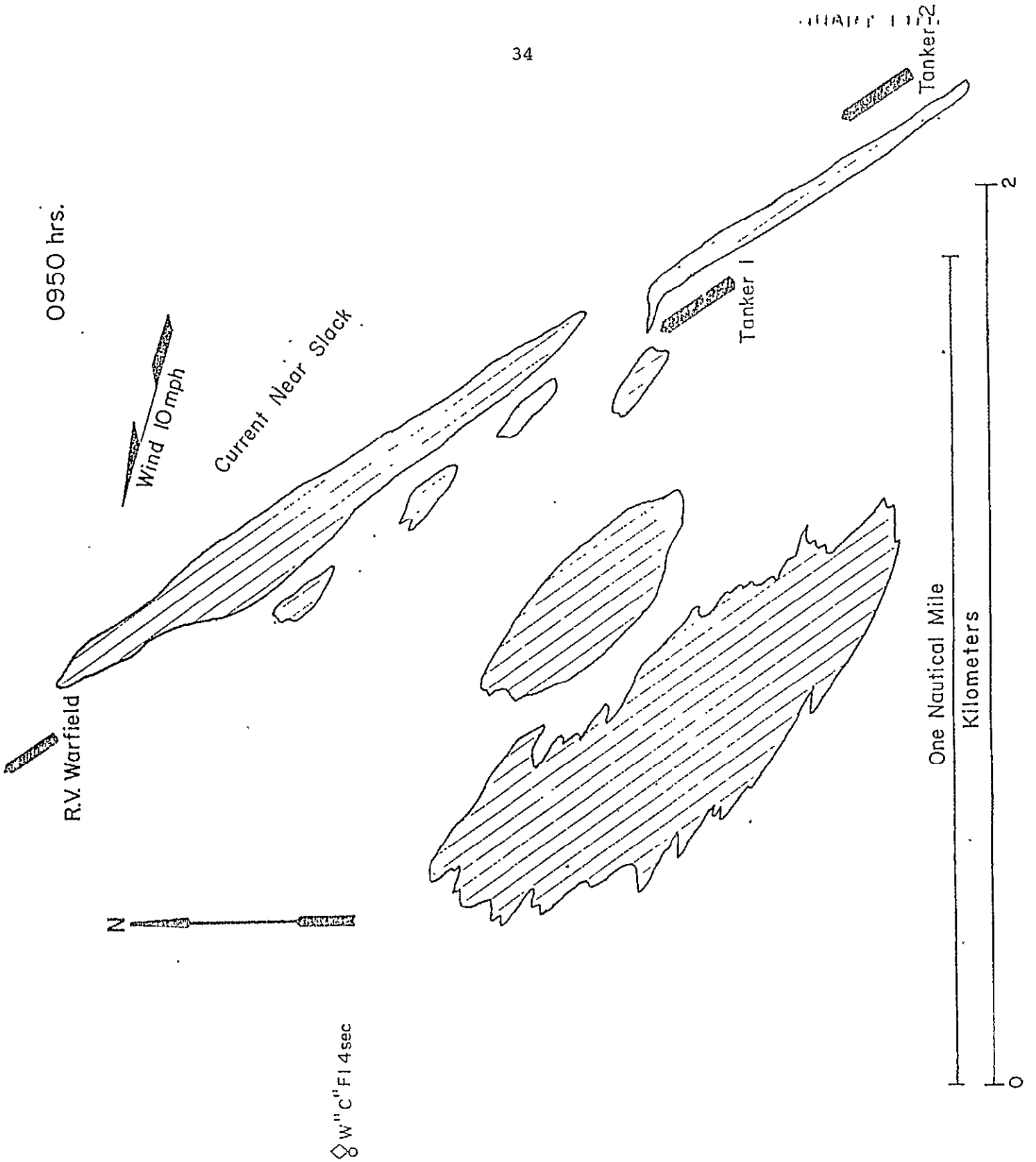

Figure 2.11. On 10 January 1975, the shown oil slick pattern was encountered at the oil lightering area in lower Delaware Bay. At 0950 hours flood tide currents were near slack and no boundaries were observed.

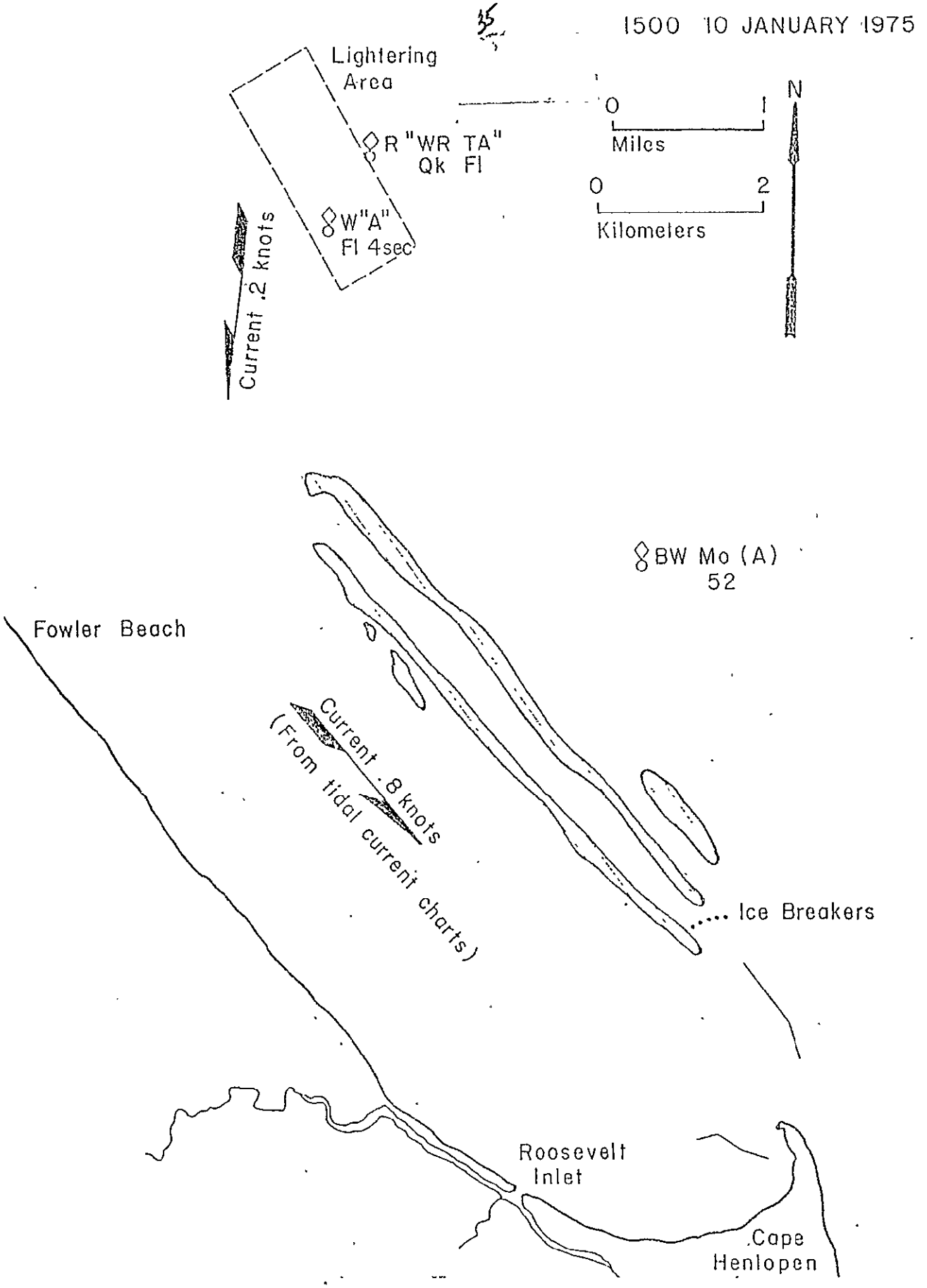

Figure 2.13. A higher altitude view of the area shows most of the oil lined up in five-mile long narrow slicks along the two boundaries.

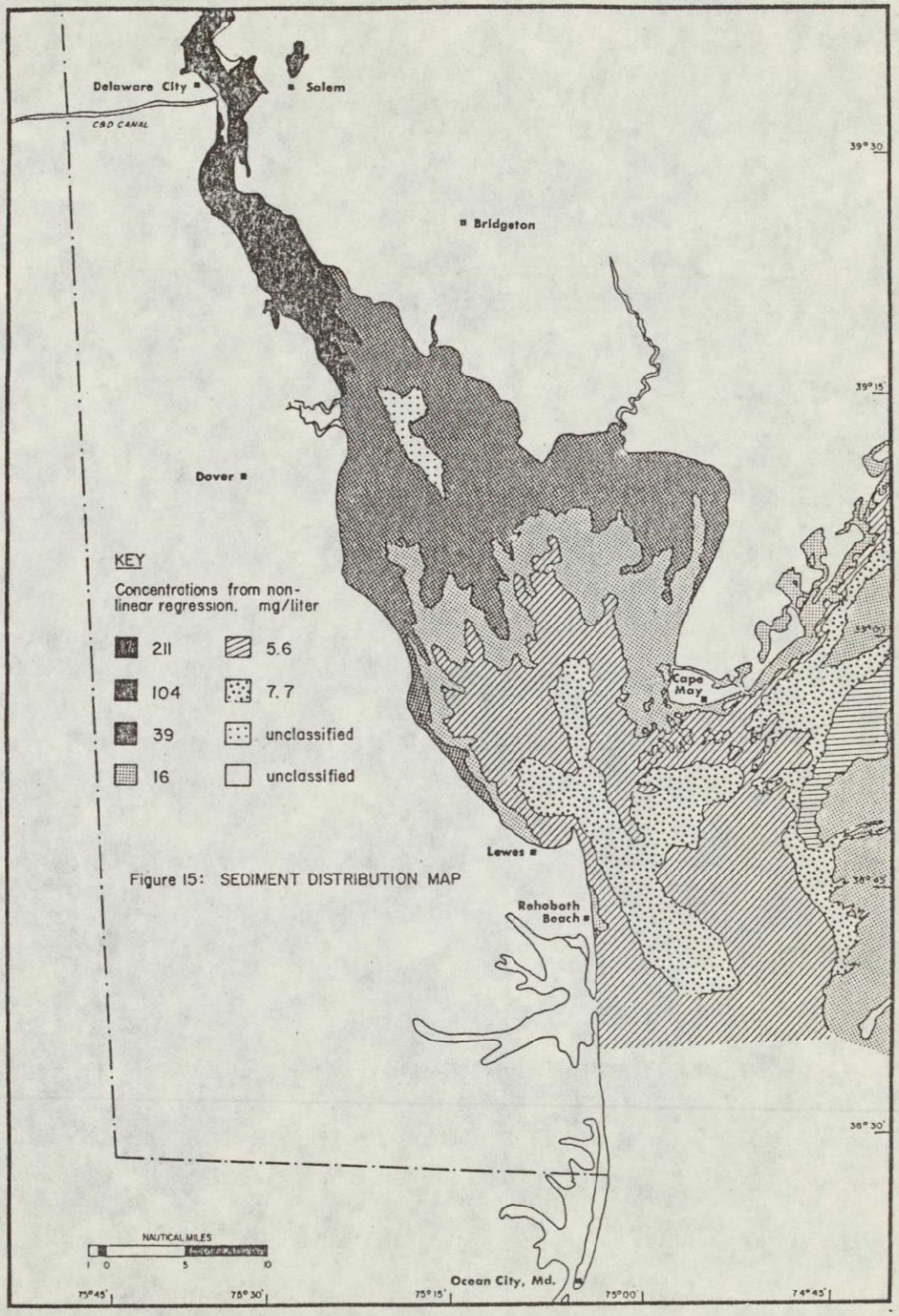

Figure 2.14. Suspended sediment concentration map for Delaware Bay obtained by correlating Landsat imagery radiance values with water samples (Klemas et al., 1972).

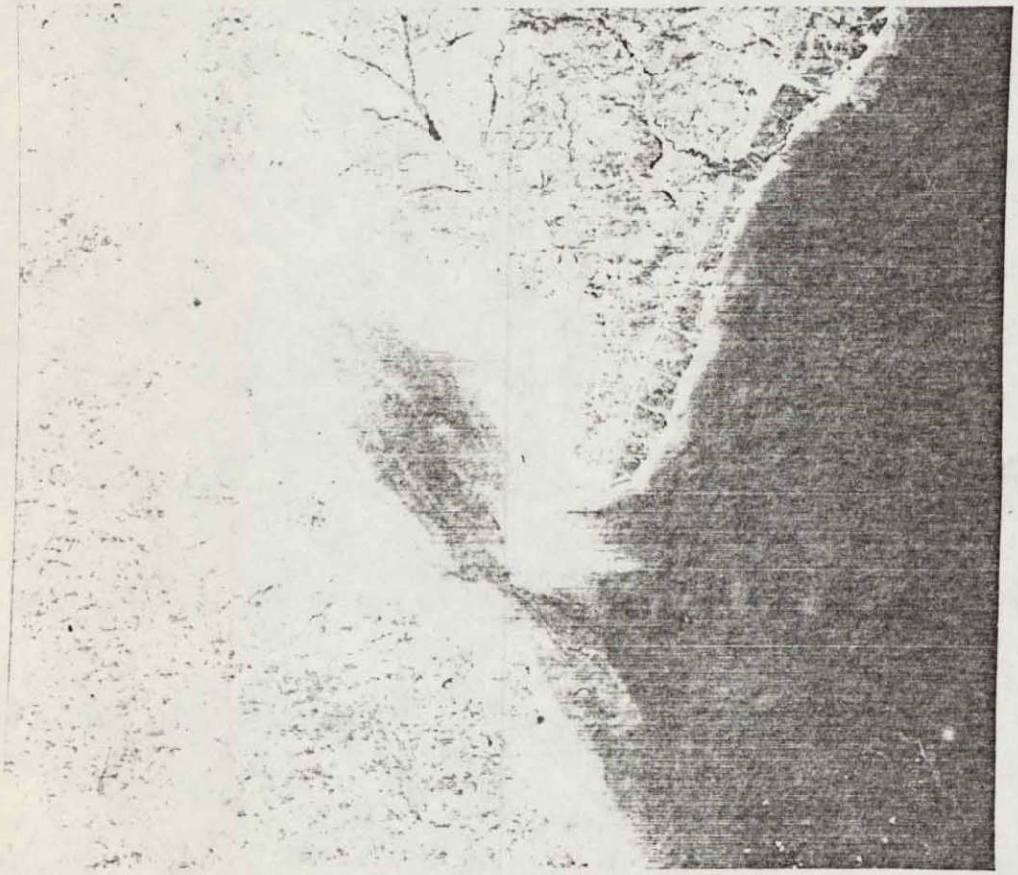

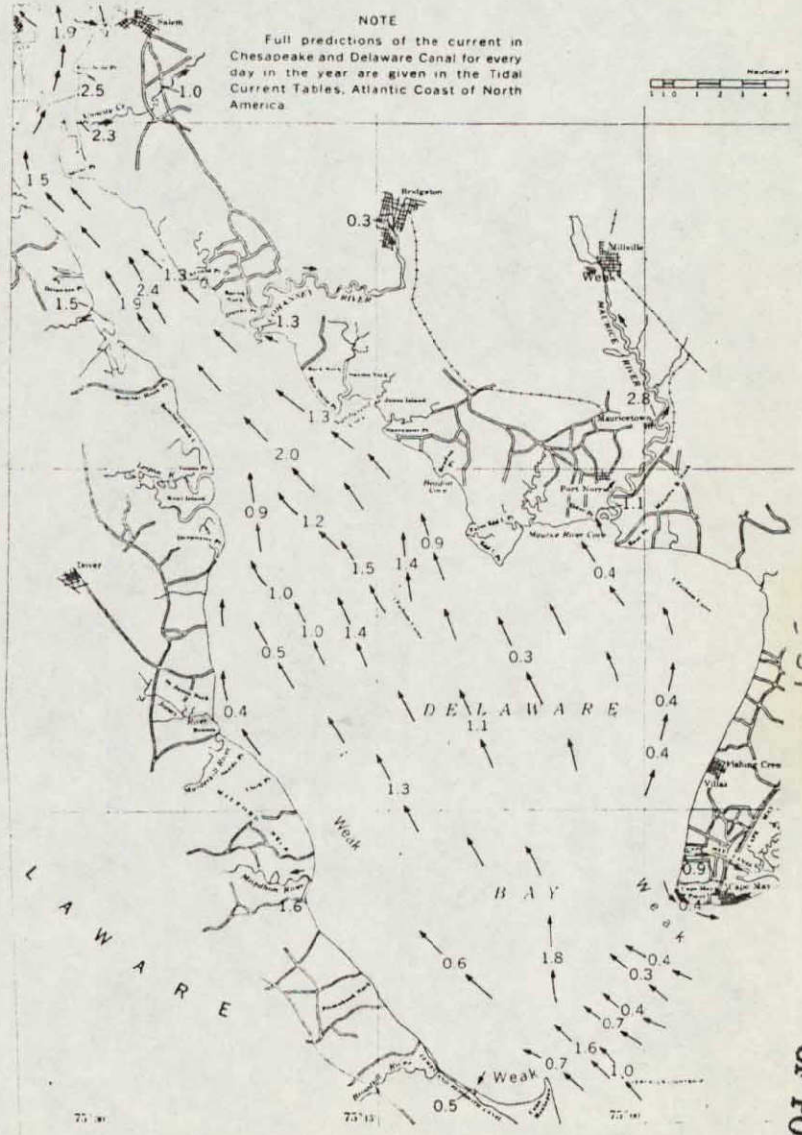

Figure 2.15. Predicted tidal currents and Landsat-1 MSS Band 5 image of Delaware Bay obtained on 10 October 1972 (I.D. No. 1079-15133).

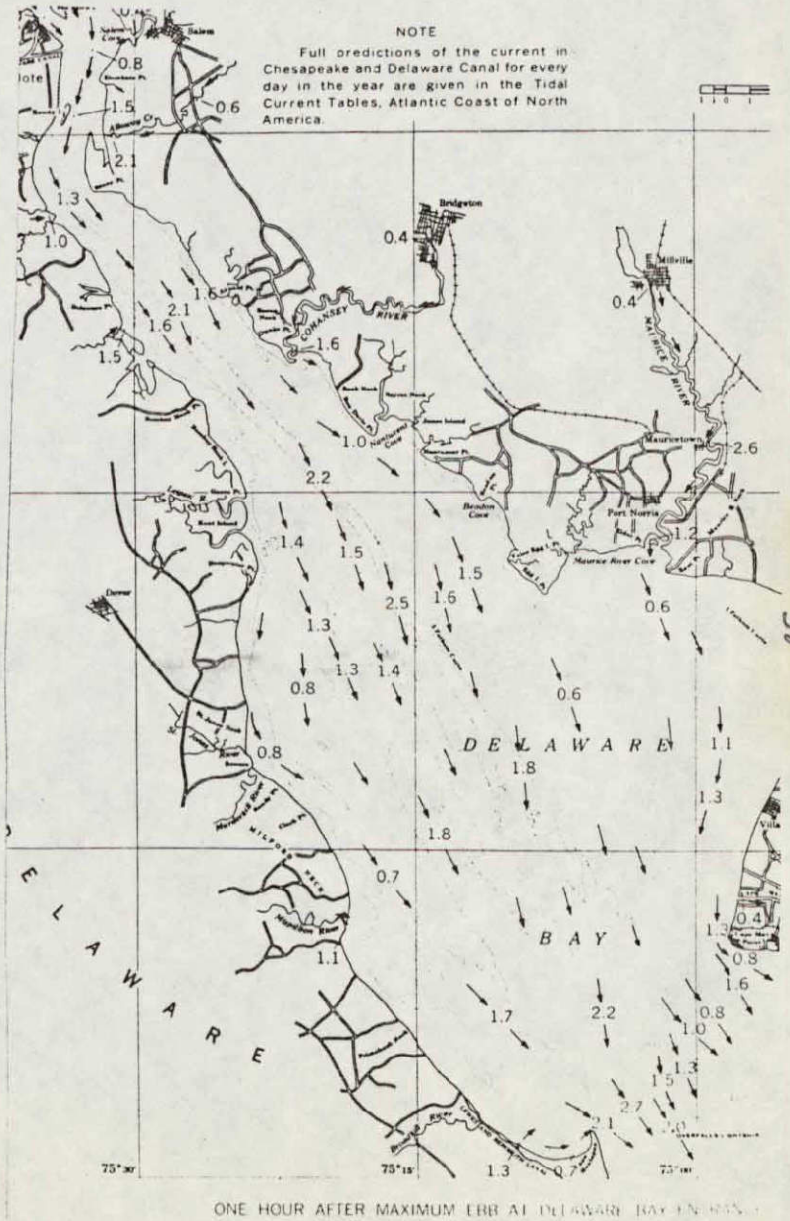

Figure 2.16. Predicted tidal currents and Landsat-1 MSS Band 5 image of Delaware Bay taken on 13 February 1973 (I.D. No. 1205-15141).

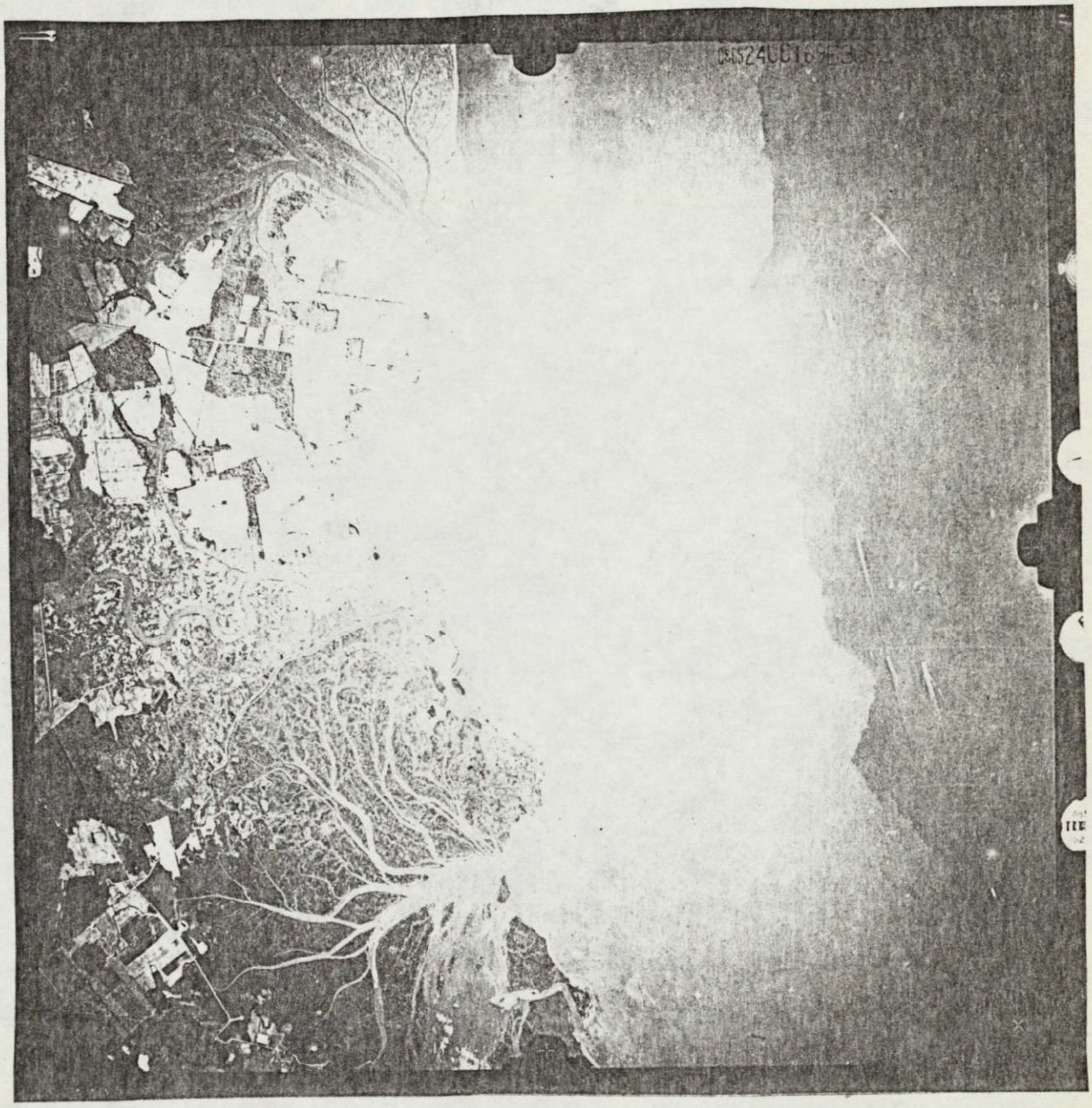

Figure 2.17. Estuarine front similar to that shown in Figure 2.15, photographed from an aircraft at a scale of 1:80,000 near Woodland Beach, Delaware. This frontal system is at least 6 km long, has an average distance of 2 km from the shoreline, and separates more turbid water near the shore from the bay's clearer water.

Figure 2.19

Boundaries visible in Landsat images of Delaware Bay taken one hour before maximum flood at the entrance of the bay.

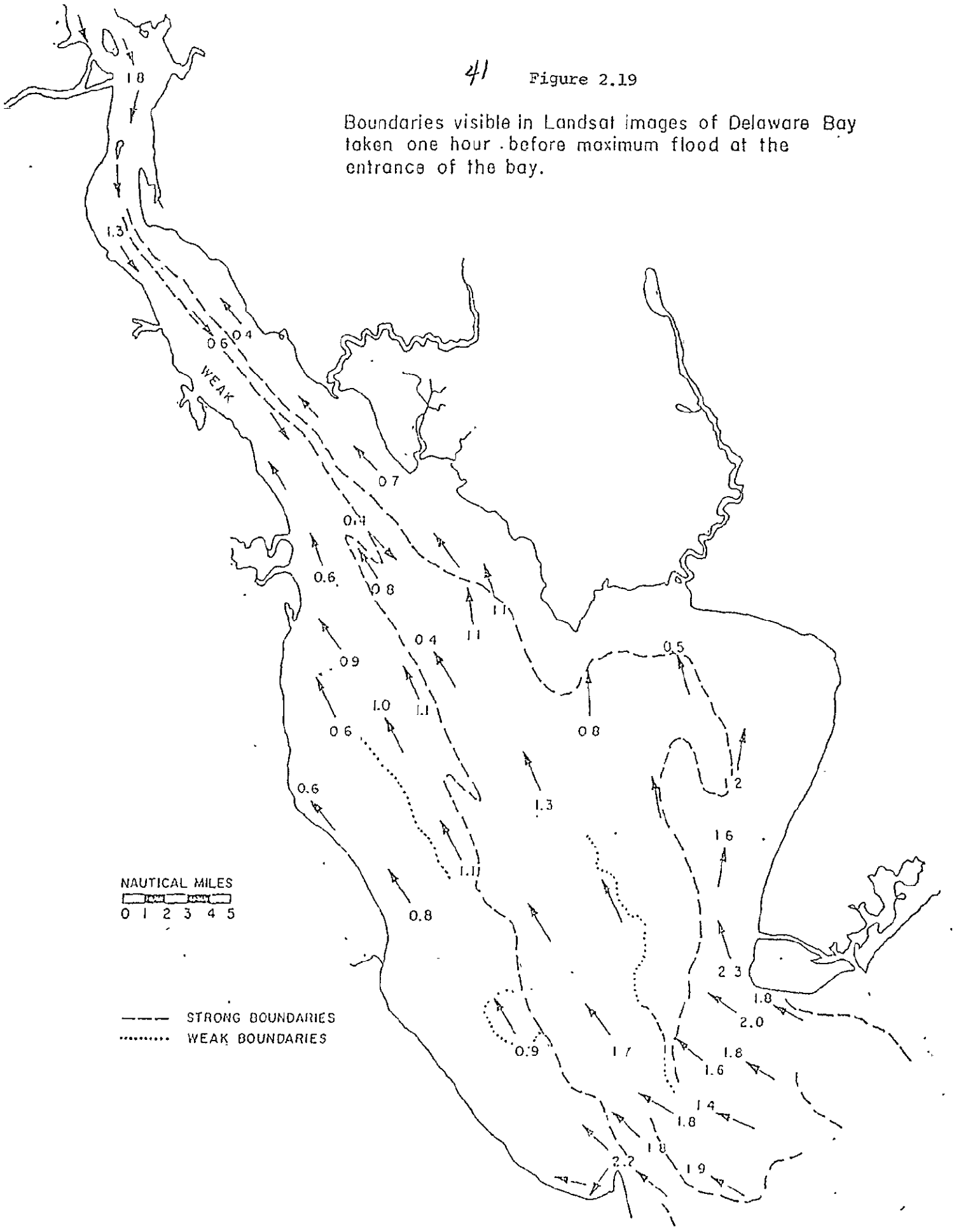

Figure 2.20

Boundaries visible in Landsat images of Delaware Bay taken at maximum flood at the entrance of the bay.

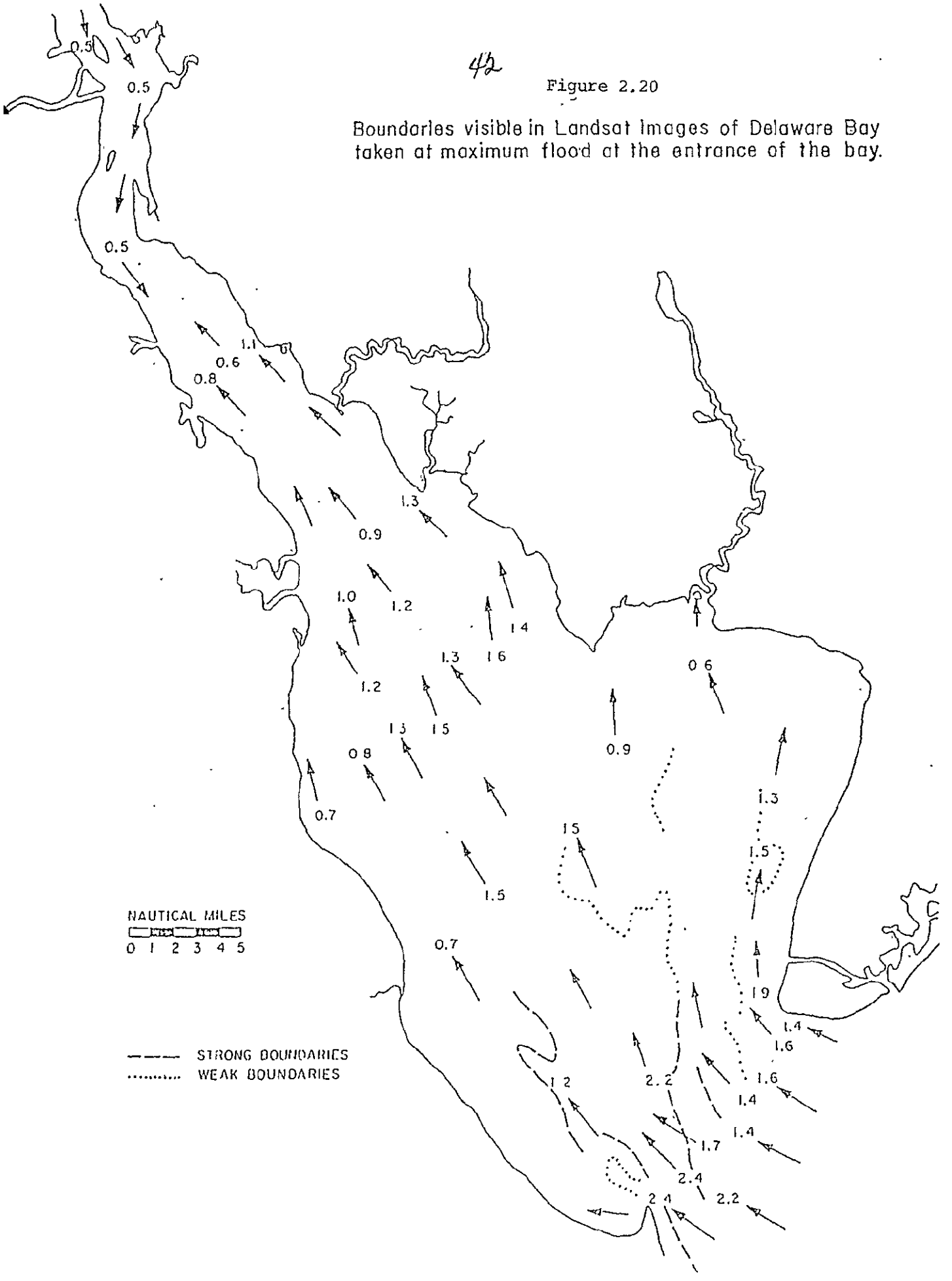

Figure 2.21

Boundaries visible in Landsat images of Delaware Bay taken one hour after maximum flood at the entrance of the bay.

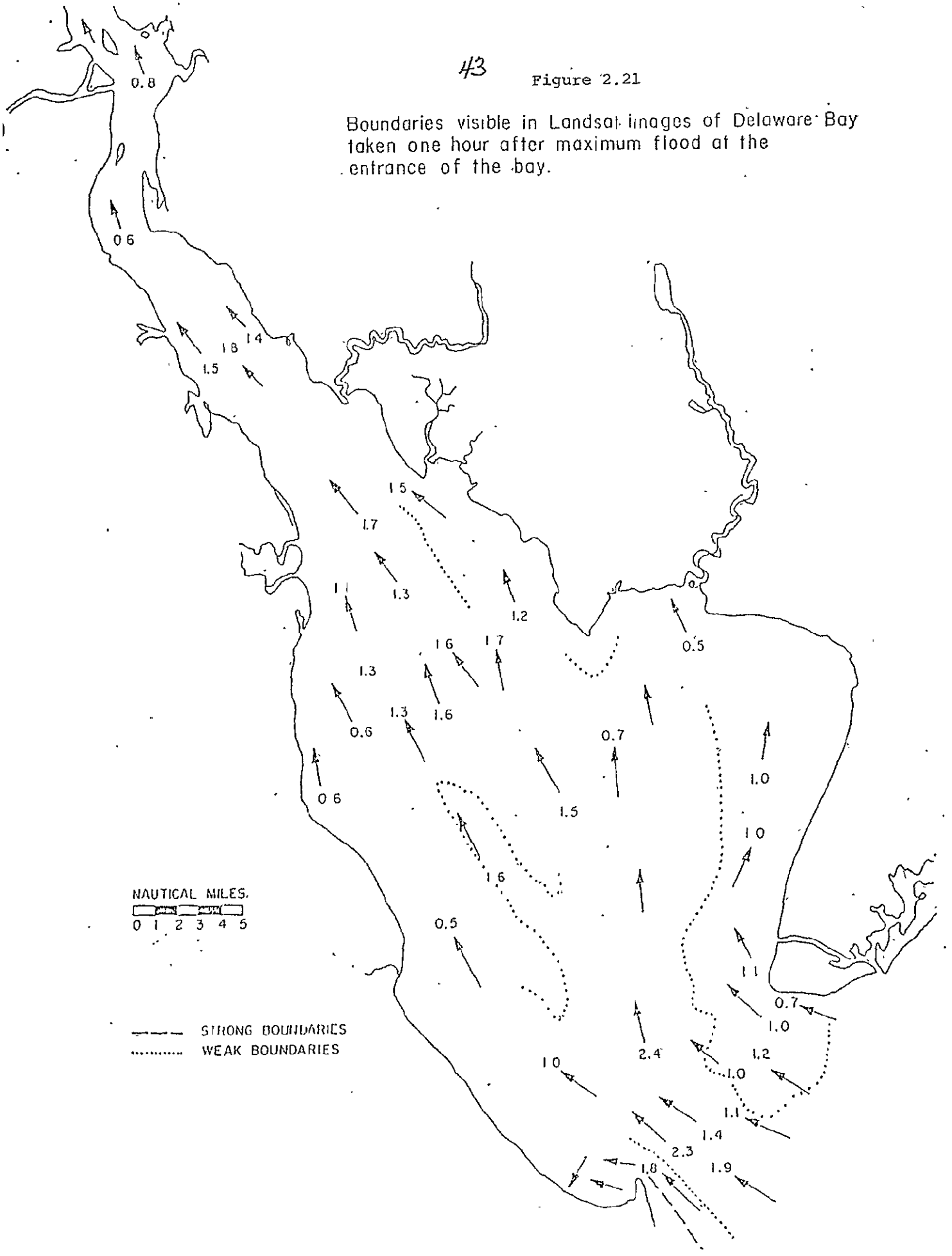

Figure 2.22

Boundaries visible in Landsat images of Delaware Bay taken two hours after maximum flood at the entrance of the bay.

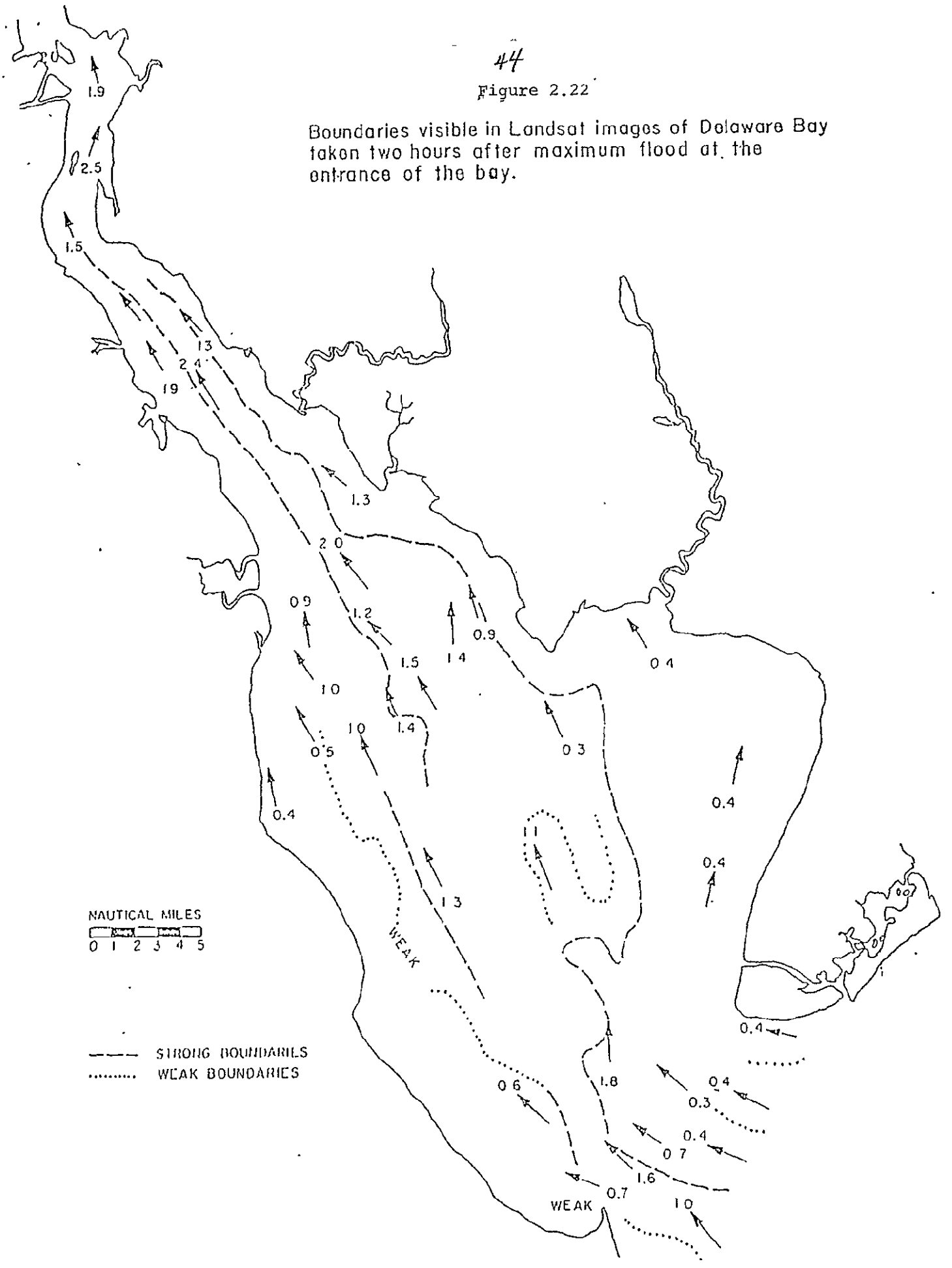

Figure 2.23

Boundaries visible in Landsat images of Delaware Bay taken three hours after maximum flood at the entrance of the bay.

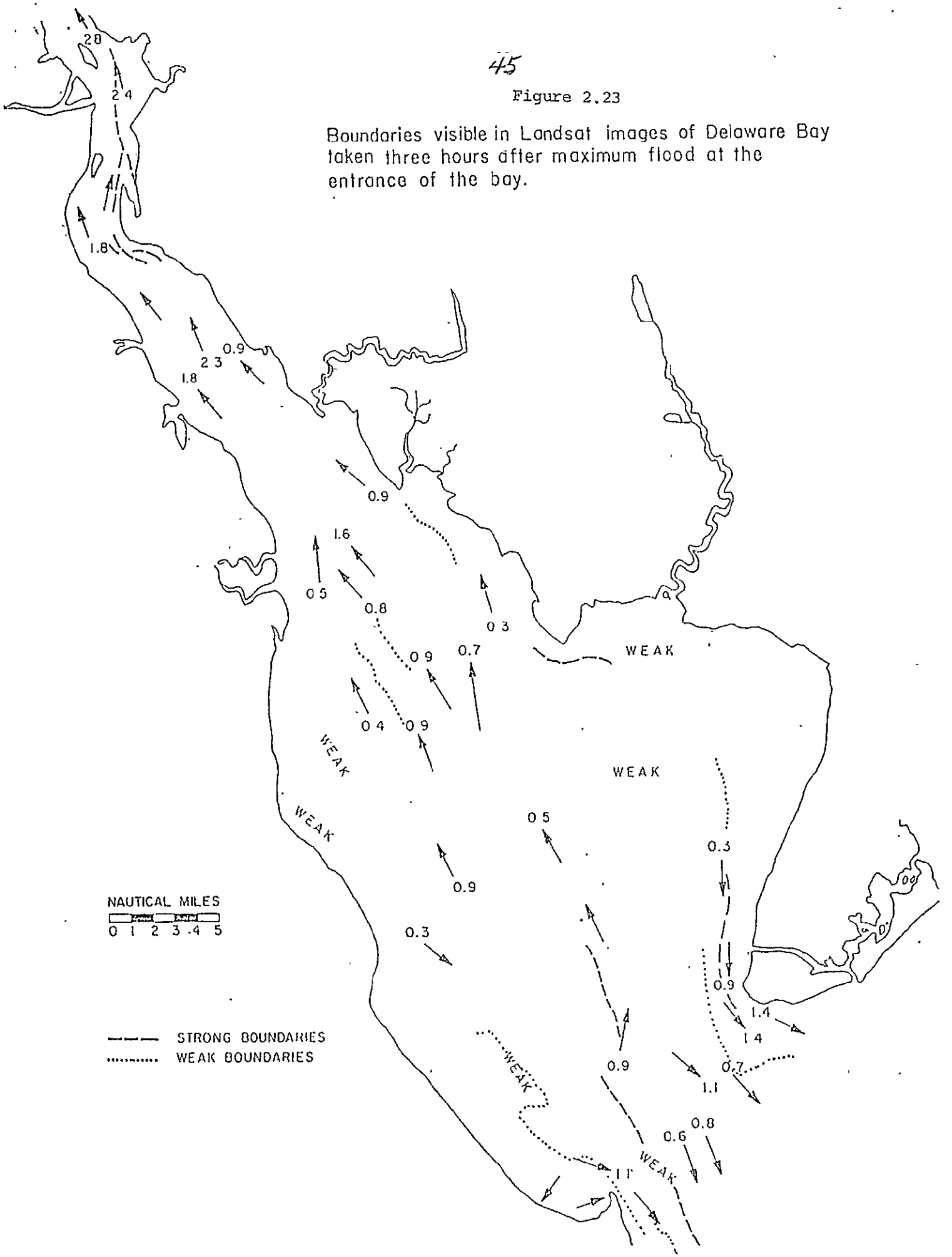

Figure 2.24

Boundaries visible in Landsat images of Delaware Bay taken two hours before maximum ebb at the entrance of the bay.

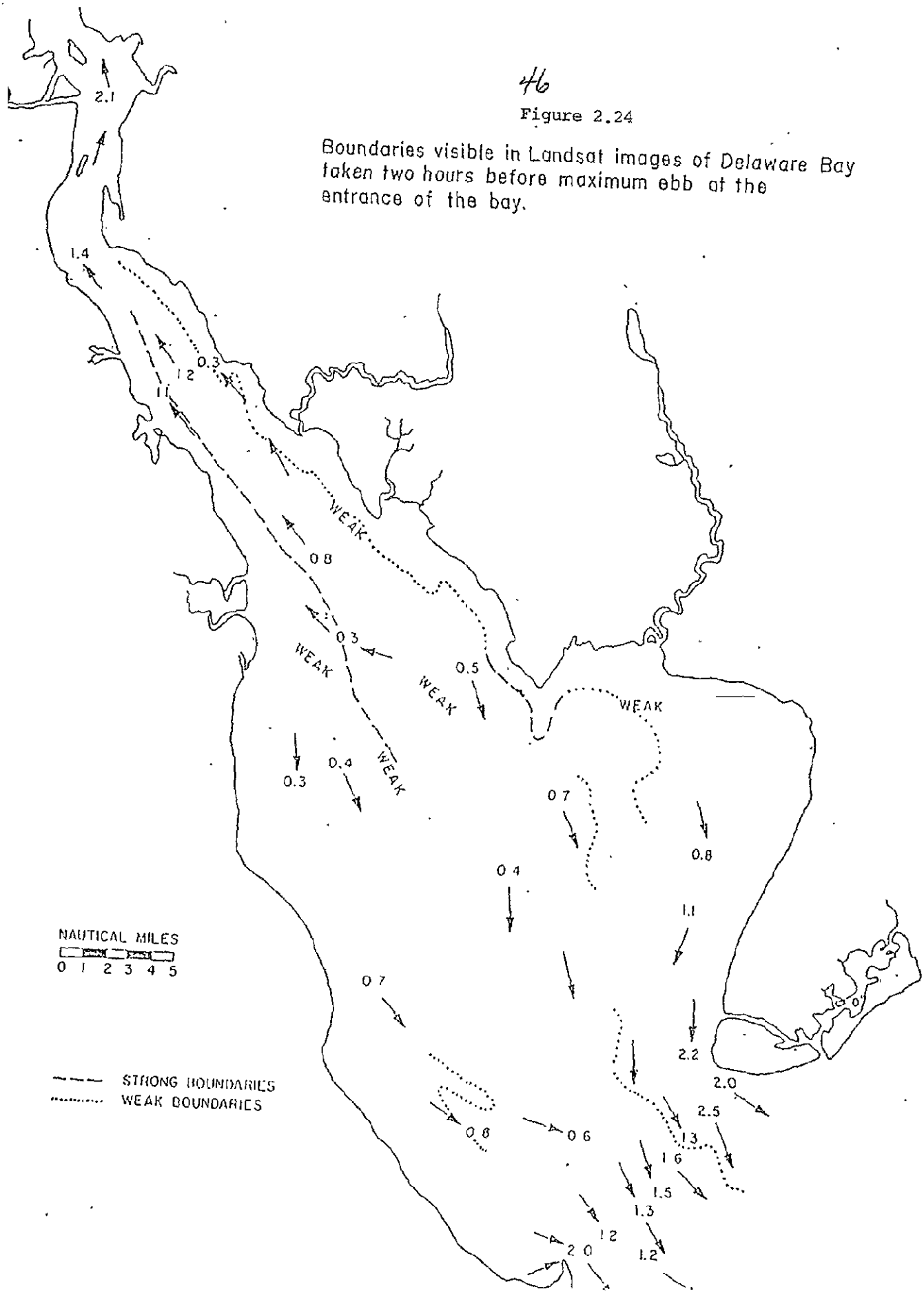

Figure 2.25

Boundaries visible in Landsat images of Delaware Bay taken one hour before maximum ebb at the entrance of the bay

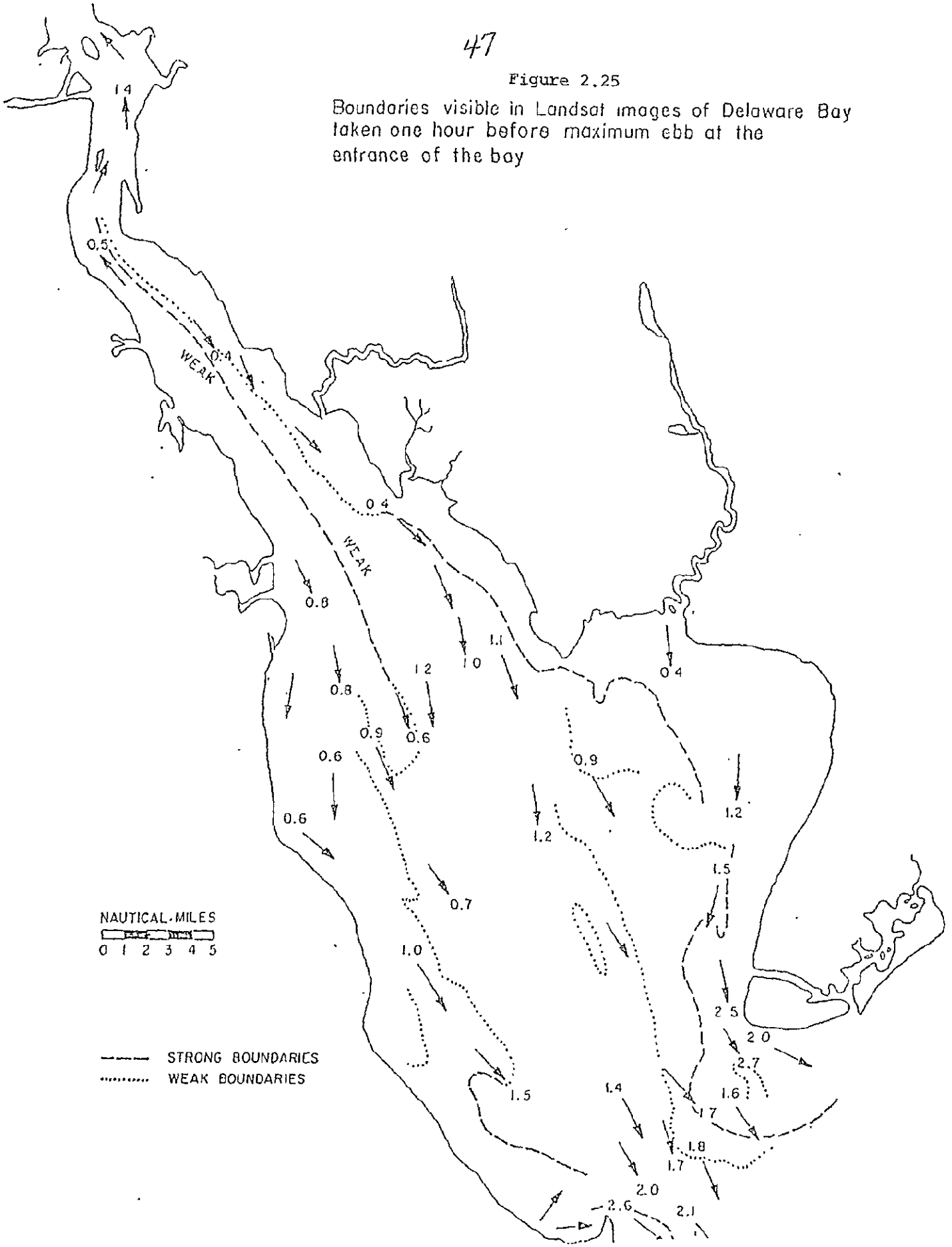

Figure 2.26

Boundaries visible in Landsat images of Delaware Bay taken at maximum ebb at the entrance of the bay.

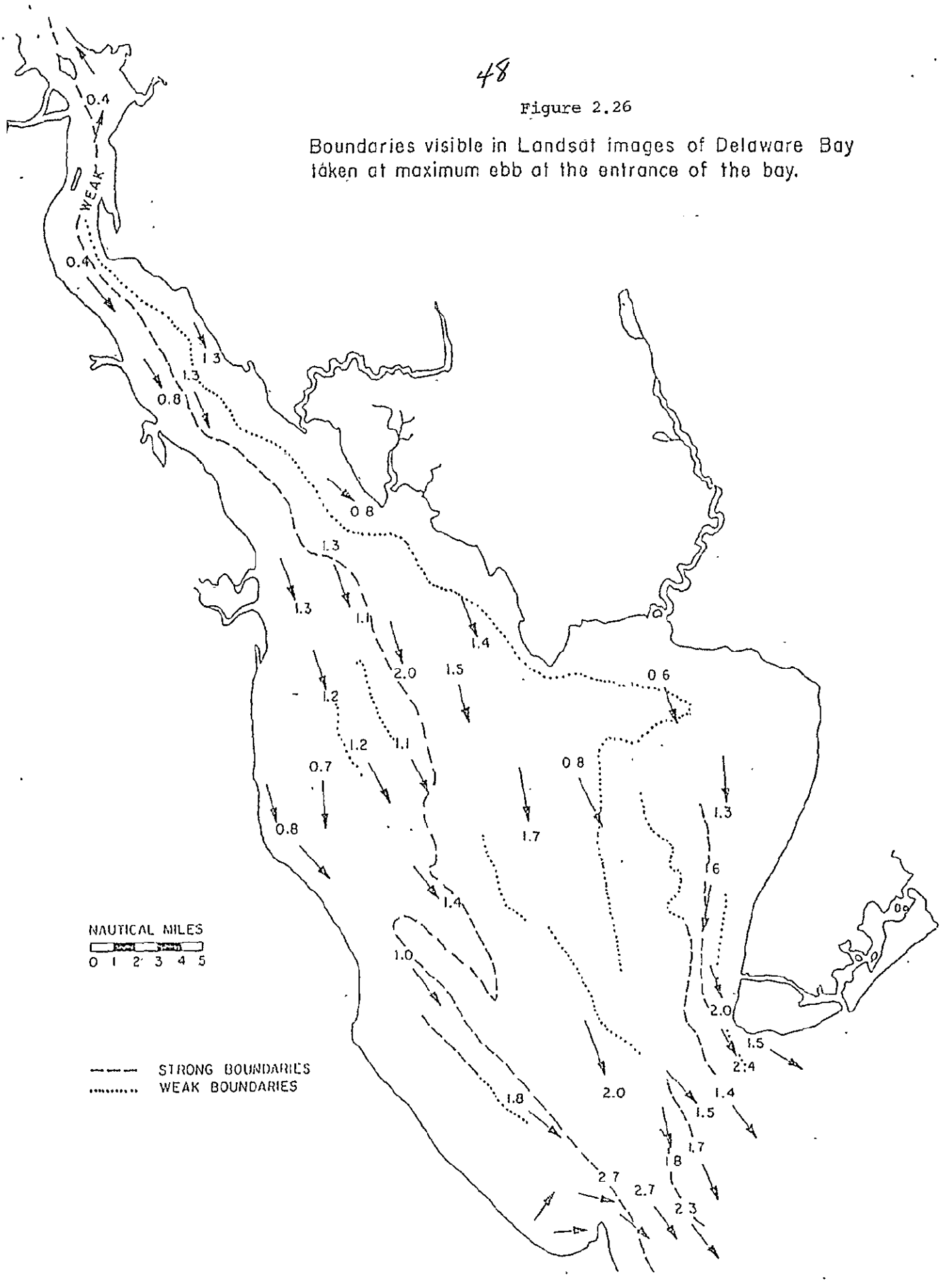

Figure 2.27

Boundaries visible in Landsat images of Delaware Bay taken one hour after maximum ebb at the entrance of the bay.

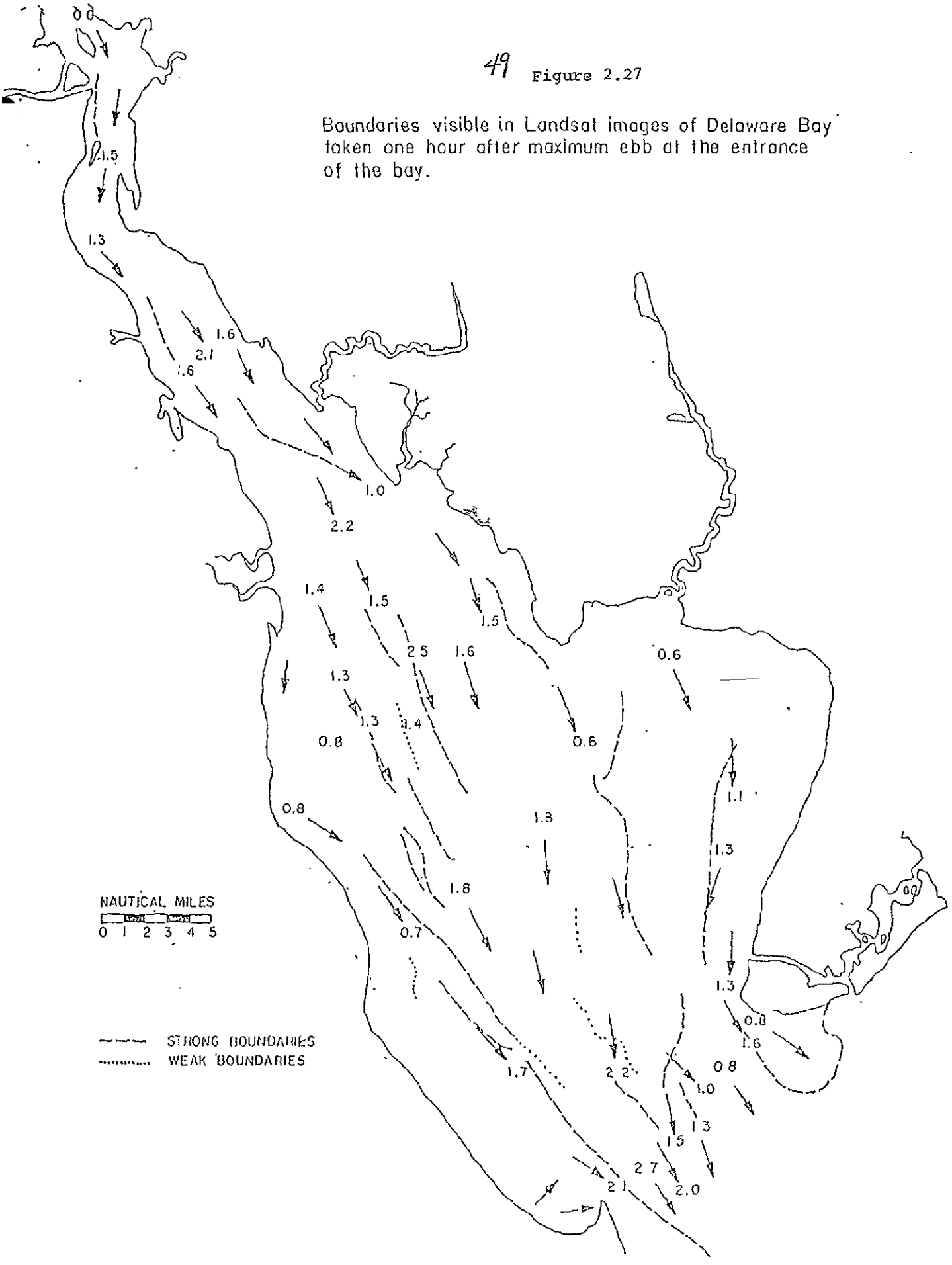

Figure 2.28

Boundaries visible in Landsat images of Delaware Bay taken two hours after maximum ebb at the entrance of the bay.

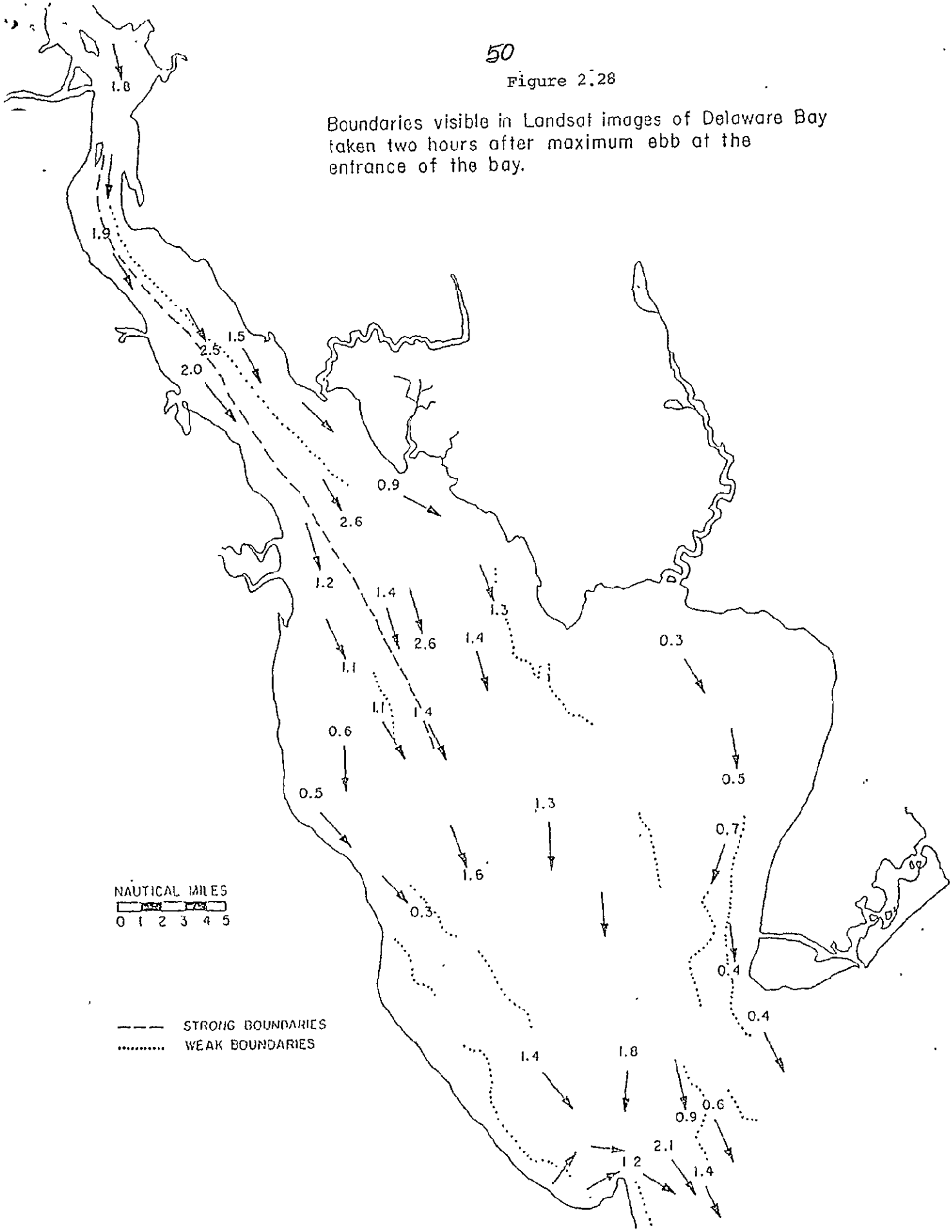

Figure 2.29

Boundaries visible in Landsat images of Delaware Bay taken three hours after maximum ebb at the entrance of the bay.

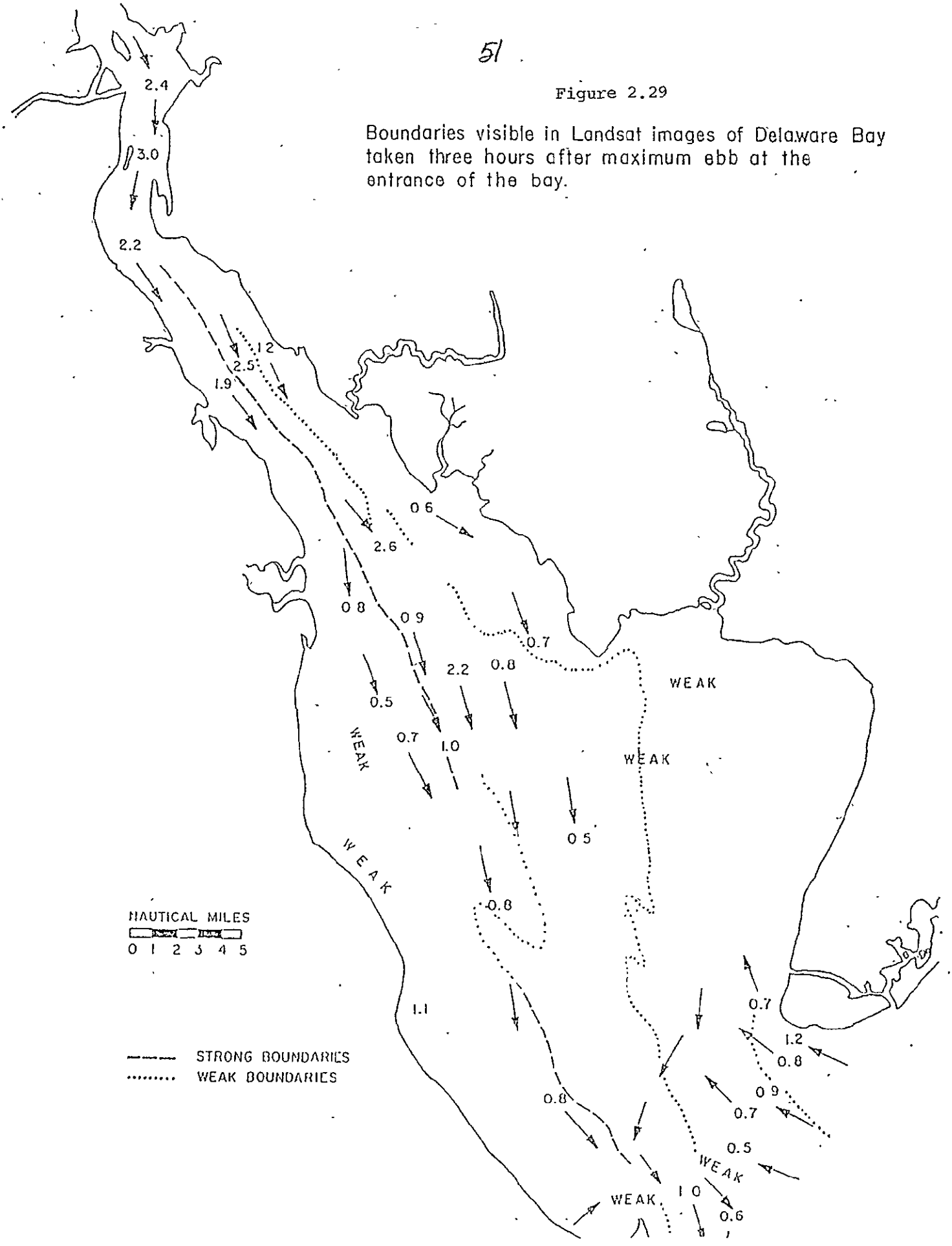

III. DETERMINATION OF THE CONCENTRATION OF SUSPENDED SEDIMENT BY REMOTE SENSING

3.0 Introduction

The ability to collect synoptic data is particularly important to estuarine investigations where significant changes can take place within a period of less than half an hour. Aircraft and satellite data have been used in a number of studies of the sediment distribution patterns in estuarine environments (Klemas et al., 1974b, Johnson 1975). One of the major problems encountered in this work arises from the fact that changes in atmospheric transmittance and reflectance change the apparent radiance measured by the satellite, making comparison of different sites or the same site on different days difficult. This section suggests a possible method for normalizing the aircraft or satellite data such that some intercomparisons may be made.

3.1 Signal at the Remote Sensing Instrument

The radiance measured by an aircraft or satellite sensor is a composite of skylight, light specularly reflected at the water surface and upwelling light from below the water surface. In using this radiance as a measure of the distribution pattern of suspended matter we make the tacit assumption that the components of radiance due to sky light and specular reflection are constant or, at worst, slowly varying over the area of interest. This is generally reasonable, especially on clear days. It is good locally even on hazy or partially cloudy days.

A second assumption is that the variations in the upwelling radiance are due predominantly, if not entirely, to variations in the concentration of the suspended matter in the water. Even though this seems to be the case for Delaware Bay, it is not necessarily true. To illustrate this point,

consider clear ocean water. Since there are very few particulates in the water, the backscattering is primarily due to the water itself and is very low level. Thus clear water appears black on Landsat imagery in all bands.

3.2 Interaction of Light with Water

Particles which are large with respect to the wavelength scatter light far more efficiently than the water itself. As the amount of suspended material in the water increases, then the backscatter should increase making water with a high suspended load appear bright. However, both suspended and dissolved material absorb light, and absorption has a controlling influence in the amount of light backscattered. In fact, assuming that the illumination is constant over the scene, the change in upwelling radiance is essentially related to the relative strength of absorption and scattering by the water. The usual measure of this relative strength in optical oceanography is the single-scattering albedo ω_o which is the percentage of light removed from a beam by scattering alone and is given by:

$$\omega_o = b/c; \; c = a + b \tag{3.1}$$

where b is the total scattering coefficient, a is the beam absorption coefficient and c is the beam attenuation coefficient. Thus, assuming constant illumination, if ω_o remains constant then upwelling irradiance remains constant even when the turbidity of the water changes.

To understand what this means, let us consider clear water again. In clear water absorption dominates over scattering, that is, $\omega_o < 0.5$ outside the blue region. For band 4, $\omega_o \simeq 0.35$ and for band 5, $\omega_o \simeq 0.08$ (Tyler et al., 1972). Particulates, although they will absorb light to a certain extent, will usually scatter light far more efficiently. This being the case,

a small amount of particulate matter added to clear water will sharply increase the scattering without significantly changing the absorption and ω_o increases sharply. As more and more particulates are added to the water, light will penetrate the water less and less and the effect of absorption by the water will decrease relative to the absorption by the particles. Eventually, when the concentration of particulates becomes high enough, absorption by the particles could actually dominate the absorption by the water at the visible wavelengths. This implies that ω_o -- and the upwelling radiance -- will increase rapidly at first when absorption by water dominates, increases more slowly as the absorption by the particulates becomes roughly equivalent to that of water, and eventually approaches a maximum value when the particulate concentration is so high that absorption by the particulates is totally dominant over the absorption by the water.

3.3 Relationship Between Concentration and Radiance

There are several inferences that can be drawn from this analysis. First, if the radiance due to pure water is N_w, then, as there is an increase in the concentration x of a substance which scatters light more efficiently than water, the radiance increases, assymptotically approaching some maximum value N_s which is typical of this substance. At the same time the penetration depth decreases and the radiance due to scattering by the water itself decreases assymptotically approaching zero. (Gordon and McCluney (1975) have defined the penetration depth for remote sensing, z_{90}, as the depth above which 90% of the diffusely reflected irradiance originates.) This suggests a relationship of the general form.

$$N_u = N_s (1-e^{-d_s x}) + N_w (1-e^{-d_w z_{90}}) \qquad (3.2)$$

where d_s is a constant related to the scattering efficiency of the particular substance in the water and d_w is related to the amount of backscattering by clear water. Since z_{90} will be a function of the concentration x, the second term of equation (3.2) could be replaced giving:

$$N_u = N_s\ (1-e^{-d_s x}) + N_w e^{-d_w' x} \qquad (3.3)$$

The apparent radiance for the Landsat sensors also includes the light backscattered by the atmosphere and the light specularly reflected at the water surface. If we notate the sum of these two sources as N_a, then the total radiance seen by the satellite is given by:

$$N_{tot} = N_u + N_a = N_s\ (1-e^{-d_s x}) + N_w e^{-d_w' x} + N_a \qquad (3.4)$$

Figure 3.1 illustrates this functional relationship. It is apparent from Figure 3.1 that the determinations of concentration made using radiance values are going to be less accurate as the radiance approaches L_s. This inaccuracy is aggravated by the nature of the Landsat digital imagery. In order that the sensors not saturate from the radiance from land areas, the gain settings are lower than would be ideal for water. The dynamic range of the sensors is rather limited for water. Since the increments in radiance are rather coarse, the uncertainties in determining concentration for higher radiance values are considerable.

Returning to equation (3.4), we find that as $x \to 0$, $N_{tot} \to N_w + N_a$, and as $x \to \infty$, $N_{tot} \to N_s + N_a$. From the data presented by Klemas et al. (1974b) for the Landsat overpass of Delaware Bay on 7 July 1973 (Table 3.1), we may estimate the value of N_{tot} for these two cases. For clear water

$N_{tot} = N_w + N_a \sim 0.2$ mw/cm^2-ster and for very turbid water $N_{tot} + N_s + N_a \sim$ 0.6 mw/cm^2-ster. Austin (1976) presents curves of path radiance and reflected radiances from which we may estimate N_a for band 5. $N_a \simeq$ 0.1 mw/cm^2-ster in band 5 means that $N_s \simeq 0.5$ and $N_w \simeq 0.1$. Equation (3.4) now becomes

$$N_{tot} = 0.5\ (1-e^{-d_s x}) + 0.1e^{-d_w x} + 0.1 \qquad (3.5)$$

For sufficiently large concentrations of suspended matter the contribution of the water to the total upwelling radiance is probably negligible and equation (3.5) becomes

$$N_{tot} = 0.5\ (1-e^{-d_s x}) + 0.1 \qquad (3.6)$$

The largest measured value of suspended matter reported by Klemas et al. (1974b) was 70 mg/l which corresponded to a band 5 radiance of 0.486 mw/cm^2. From experience we know that a concentration as high as 70 mg/l in Delaware Bay means the Secchi depth is no more than a few centimeters so, although there will be some error introduced by ignoring the radiance from the water, the error should be small. Thus, we have

$$0.486 \simeq 0.5\ (1-e^{-70d_s}) + 0.1 \qquad (3.7)$$

from which we have, solving for d_s

$$d_s \simeq 0.02112 \qquad (3.8)$$

Substituting this value of d_s back into equation (3.5) and using the lowest measured value of suspended matter and the corresponding radiance from Table 3.1.

TABLE 3.1 This table shows the actual radiance values in each band, the four measured concentrations and the extrapolated concentration values. The values in parenthtesis are for areas whose spectral signature varies only slightly from the sediment signature pattern. No sediment values are given for regions with anomalous signatures. (From Klemas et al., 1974b).

Reference Spectrum	Band 4	Band 5	Band 6	Band 7	Suspended Load mg/l Measured	Calculated
1	.659	.358	.178	.211	25	25
2	.642	.341	.153	.147	20	20
3	.587	.310	.164	.187		15
4	.703	.410	.223	.255	40	35
5	.719	.406	.177	.145		
6	.539	.250	.125	.112		6
7	.504	.223	.108	.093		3
8	.496	.247	.157	.150		
9	.782	.486	.251	.280	70	60
10	.790	.530	.301	.335		85
11	.853	.613	.341	.370		>150
12	.797	.549	.368	.492		
13	.627	.343	.222	.374		
14	.462	.192	.096	.104		0

$$0.341 = 0.5\ (1-e^{-(0.0211)(20)}) + 0.1e^{-20d_w'} + 0.1 \qquad (3.9)$$

Solving for d_w', we have

$$d_w' = 0.0187 \qquad (3.10)$$

The lowest measured value of suspended matter is used since the term with d_w' is most significant for low concentrations. Thus, the determination of d_w' is more accurate.

Finally, substituting these constants in equation (3.5) we have a relationship between the radiance measured by the satellite and the concentration of the suspended matter in the water:

$$N_{tot} = 0.6 - 0.5e^{-0.02112x} + 0.1e^{-0.0187x} \qquad (3.11)$$

Equation (3.11) is plotted in Figure 3.2. The actual measured points are shown and the fit is remarkably good. The fit is worst for the higher concentrations because the estimate of d_s was made assuming that the radiance from the water was negligible. Apparently, at 70 mg/l, where the estimate was made, the radiance from the water is small but not quite negligible. This is especially true since errors become very large very quickly, i.e. a small error in the radiance gives a large error in the estimate of concentration. The coefficients could easily be adjusted to give a better fit to the measured values.

3.4 Discussion

The significance of all this is that the curve of Figure 3.2 is not just a least squares fit to available data but a semi-empirical relationship. The advantage is that the relationship should be repeatable as long as reasonable estimates can be made of the five constants. If we limit

observation to clear days N_a and N_w should be stable. The other three constants are dependent upon the optical properties of the substance in the water. In a region where the optical properties of the suspended material are reasonably constant with space, equation (3.4) should serve as an effective predictor of surface concentration.

Particularly interesting are the coefficients d_s and d_w'. Both are related to the relative strength of scattering and absorption in the water. The exact physical relationship is not clear at this time. However, in that both d_s and d_w' are obviously related to the optical properties of substances in the water, they may serve as a means of classifying different substances in the water.

Throughout this analysis, we have made several tacit assumptions which require some examination. The first assumption was that the radiance due to surface reflection is negligible compared to skylight and that both are constant over the 7 July 1973 Landsat scene. This means assuming that there is no variation in surface slicks on the water or in haze or aerosol distribution in the air. Even on a day as apparently clear as 7 July 1973 some variability in atmospheric backscatter is to be expected. In fact, in a land use study using Landsat data for this day (Klemas et al., 1974c), more haze was found to be over the northern portion of the bay than over the southern end. This variability suggests that estimates of N_a should be made for several parts of the Landsat scene. This is best done using surface-based measurements such as those outlined by Duntley et al. (1970).

We have also assumed that the water is vertically homogeneous when, actually, Delaware Bay often exhibits a great deal of stratification. However, what is important here is vertical homogeneity over the depth of penetration of light as seen by Landsat. This condition is probably

fulfilled. Using Gordon and McCluney's (1975) definition of penetration depth for remote sensing, Figure 3.3 shows the variation of the penetration depth, z_{90}, with wavelength for several types of coastal water. The curve labeled '9' represents the most turbid water of the examples presented. Band 4 (500-600 nm) is capable of the deepest penetration into the water, but the penetration depth also varies widely. The penetration depth of band 5 (600-700 nm) is both shallower and more restricted, ranging between 1.5 and 3.0 meters. Bands 6 and 7 penetrate the water even less. Estimates for band 7 range from millimeters to a few centimeters making it better suited for detecting surface slicks than suspended material. Water types 5 through 9 are probably typical of the waters in Delaware Bay. Vertical homogeneity over such shallow depths is a reasonable assumption.

The final, and perhaps the most crucial assumption, is that the suspended material throughout the bay is optically very similar. There is no a priori reason to expect that this should be true. However, Klemas et al. (1974b) classified the entire bay by its spectral characteristics. This was done by choosing a training set or clusters of pixels, in an area for which the radiance readings were relatively constant in each band. The average four-band spectrum was found for this set. Each pixel in the scene was then compared to this reference spectrum and if the spectra matched, the pixel was so classified. Another training set would then be chosen in order to define a second reference spectrum, and each pixel compared with it. This procedure was continued until essentially all the pixels had been classified.

The set of reference spectra are shown in Figure 3.4. The approximate positions of the training set from which each reference spectrum was derived is shown in Figure 3.5. Most of the reference spectra are of the same

general form and vary in a regular way which tends to support the contention that most of the material in the bay is optically very similar. The four reference spectra (1, 2, 4, and 9 on Figures 3.4 and 3.5) which correspond to the areas in which water samples were collected all belong to this group. Significant changes in the optical properties of the suspended material should cause noticeable changes in the spectrum -- other than a change in total intensity. Such a change is noticeable in reference spectra 5, 8, 12 and 13 which are shown as dotted lines in Figures 3.4.

Thus, it seems reasonable that areas which exhibit the same spectral shape may be compared using the same algorithm. This method requires ground truth for at least three concentrations of suspended matter: clear water, a very high concentration and some intermediate (low) value.

3.5 Conclusions

A method has been presented for making estimates of the concentration of suspended matter in Delaware Bay with only a limited amount of ground truth. The method makes use of the fact that there is normally a wide range of concentrations in bay waters to derive an equation relating radiance to concentration. There are two primary assumptions made: 1) atmospheric effects are effectively unchanging over the entire bay and 2) suspended material is optically the same throughout the bay -- verified by spectral characteristics.

If this approach proves workable it should be possible to compare Landsat data for different overpasses of the bay with only a few data points for each pass.

3.6 References

Austin, R. W. (1976) Remote sensing of spectral radiance. In: Optical Aspects of Oceanography. Jerlov and Nielsen, ed. Academic Press, N.Y.

Duntley, S. Q., C. F. Edgarton and T. J. Petzold. (1970) SIO Ref. 70-27, Scripps Inst. of Oceanography, La Jolla, California.

Gordon, H. R. and W. R. McCluney. (1975) Estimation of the depth of sunlight penetration in the sea for remote sensing. Appl. Optics 14(2): 413-416.

Johnson, R. W. (1975) Quantitative suspended sediment mapping using aircraft remotely sensed multispectral data. Proceedings, Earth Resources Survey Symp., Houston, Texas, June 1975.

Klemas, V., D. Bartlett, W. Philpot, R. Rogers and L. Reed. (1974a) Coastal and estuarine studies with ERTS-1 and Skylab. Remote Sensing of Environment 3: 153-174.

Klemas, V., D. Bartlett and R. Rogers. (1974b) Inventories of Delaware coastal vegetation and land use utilizing digital processing of LANDSAT imagery. Proceedings, Ninth Internatl. Symp. on Remote Sensing of Environment, Ann Arbor, Michigan.

Klemas, V., M. Otley, W. Philpot, C. Wethe, R. Rogers and N. Shah. (1974c) Correlation of coastal water turbidity and current circulation with ERTS-1 and Skylab imagery. Proceedings, Ninth Internatl. Symp. on Remote Sensing, Ann Arbor, Michigan.

Tyler, J. E., R. C. Smith and W. H. Wilson, Jr. (1972) Predicted properties for clear natural waters. J. Optical Society of America 62(1): 83-91.

3.7 List of Figures

Figure 3.1: Relative contribution to the total upwelling radiance due to scattering by water and substances in the water with increasing concentration.

Figure 3.2: Variation of radiance with the concentration of suspended material.

Figure 3.3: Variation of z_{90} with wavelength for various coastal water types.

Figure 3.4: Spectral signatures of the training sets. The signatures which are most similar in form and which are probably representative of different concentrations of the same type of sediment are shown by solid lines. The dotted lines are signatures which deviate from the sediment signature pattern.

Figure 3.5: Map of Delaware Bay. The solid lines show the transects along which ground truth was collected on July 7, 1973. The numbers show the points at which the training sets were chosen.

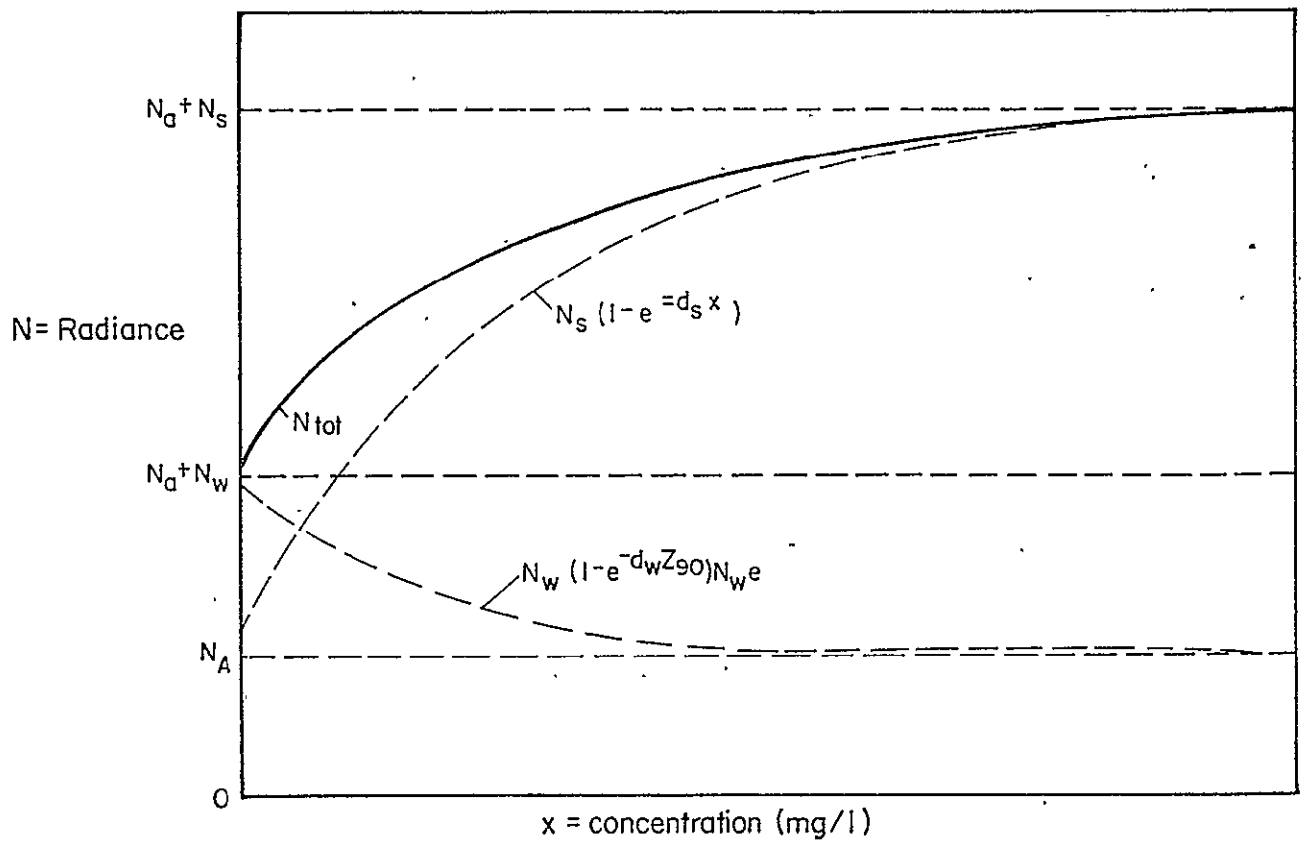

Figure 3.1. Relative contribution to the total upwelling radiance due to scattering by water and substances in the water with increasing concentration.

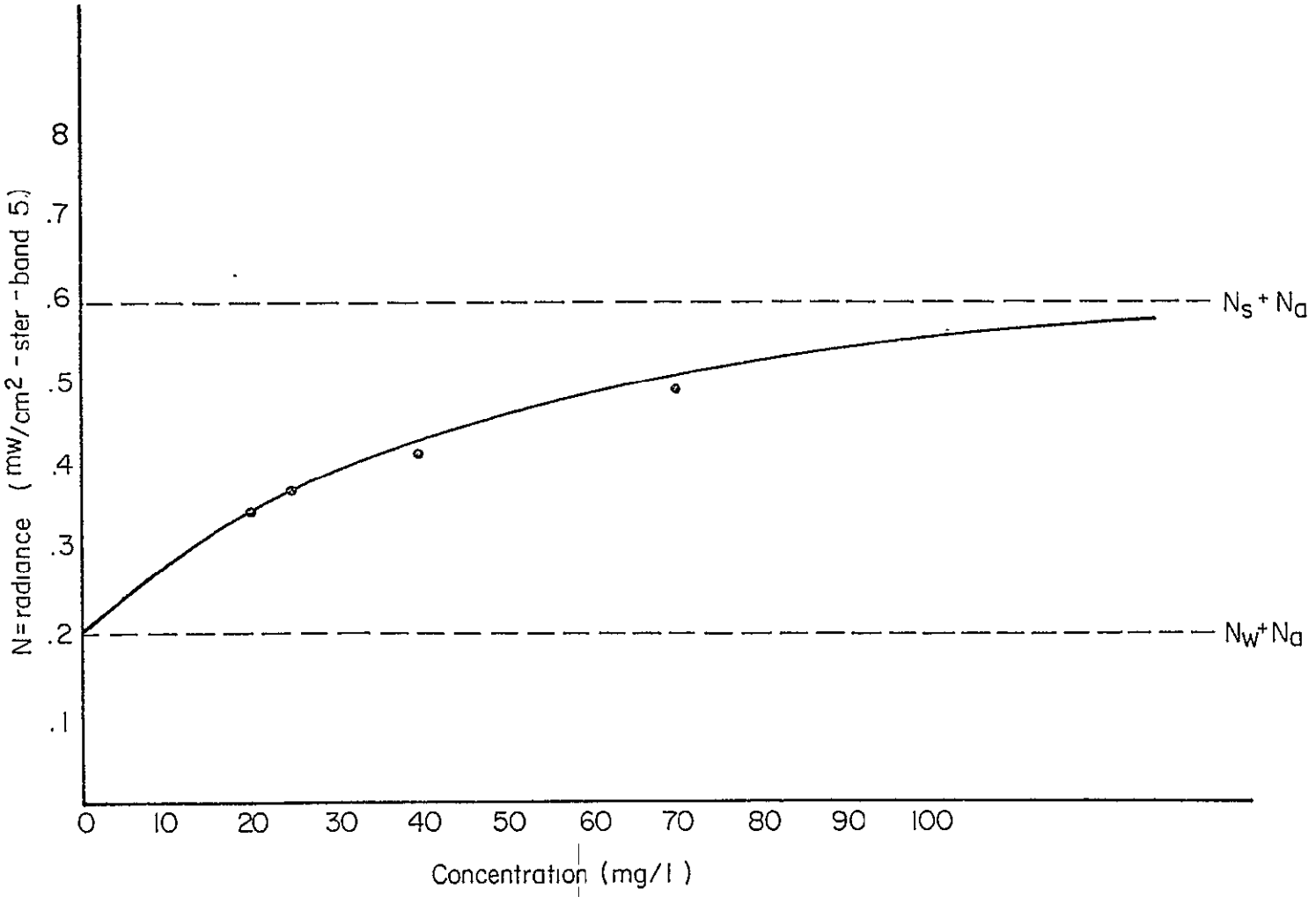

Figure 3.2. Variation of radiance with the concentration of suspended material.

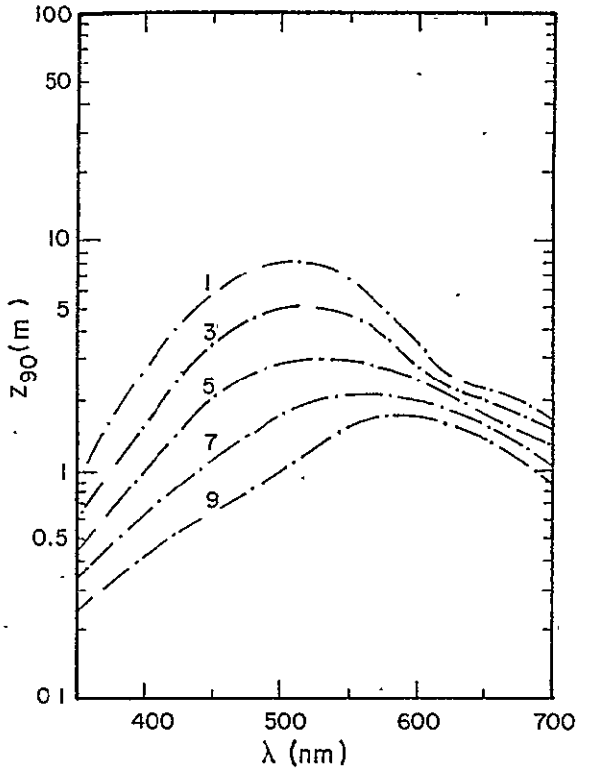

Figure 3.3. Variation of z_{90} with wavelength for various coastal water types. (From Gordon & McCluney, 1975)

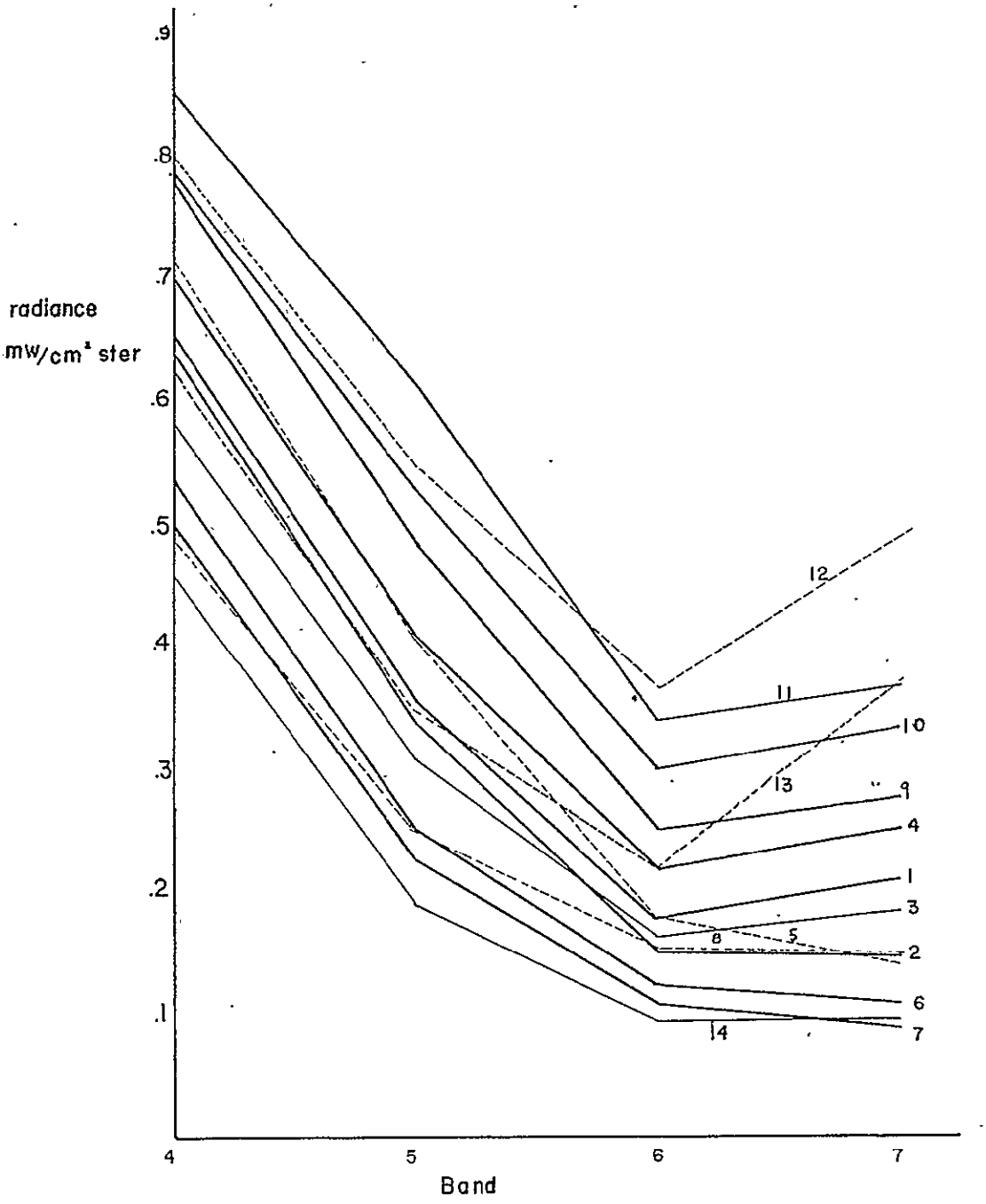

Figure 3.4

Spectral signatures of the training sets. The signatures which are most similar in form and which are probably representative of different concentrations of the same type of sediment are shown by solid lines. The dotted lines are signatures which deviate from the sediment signature pattern.

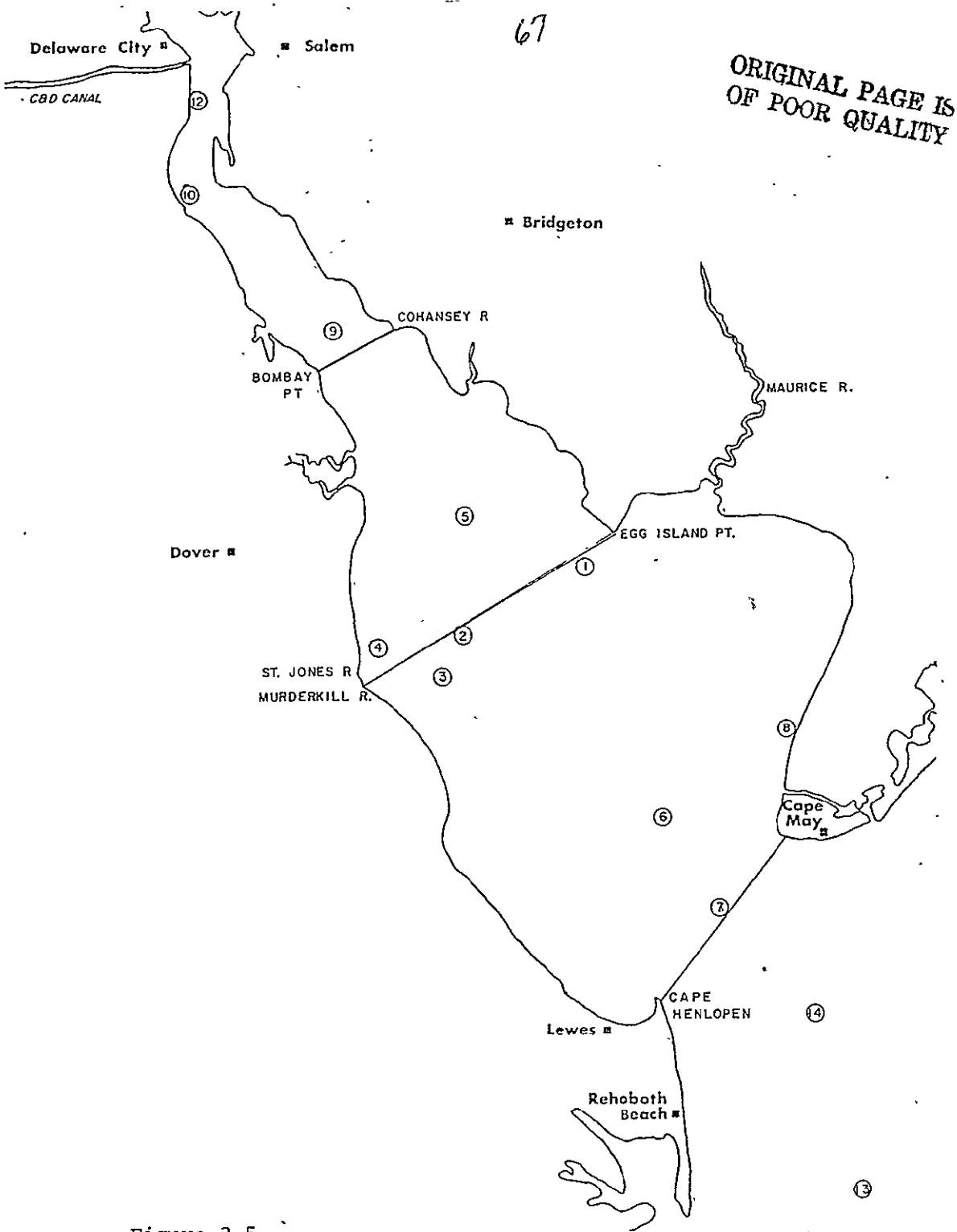

Figure 3.5 Map of Delaware Bay. The solid lines show the transects along which ground truth was collected on July 7, 1973. The numbers show the points at which the training sets were chosen.

IV. MONITORING THE DISPERSION AND MOVEMENT OF OCEAN DUMP PLUMES

4.0 Introduction

The continuing use of the continental shelf for waste disposal and the extraction of oil and other resources pose an environmental threat to the shelf regions. The offshore-onshore transport rates of pollutants, sediments, and nutrients strongly influence the ecology of the coastal zone. In order to keep the environmental impact within acceptable levels, it is important to understand the circulation and exchange processes on the shelf. Satellites can make synoptic observations of certain large scale processes indicative of pollution transport on the continental shelf. The objective of this study was to determine from Landsat imagery the drift and dispersion of plumes generated by the dumping of acid waste and to compare the satellite results with drogue and current meter data.

4.1 Waste Composition and Disposal

The barged wastes come from the manufacture of titanium dioxide pigment. The specially designed barge, described by Fader (1972) is 270 feet long, 60 feet wide, and 18 feet deep, and has a total capacity of about one million gallons (5,000 tons). Radio-controlled signals from a towing tug release the wastes from the unmanned barge in a designated disposal area.

Wastes flow from the barge by gravity at a controlled rate into a disposal area recommended by the U. S. Interior Department's Bureau of Commercial Fisheries (now the National Marine Fisheries Service, Department of Commerce). The waste disposal area encompasses a rectangle five by about eight nautical miles centered approximately 38 nautical miles southeast of Cape Henlopen, Delaware (Figure 4.1). The area is bounded by $38^{\circ}30'$ and $38^{\circ}35'$ north latitude, and $74^{\circ}15'$ and $74^{\circ}25'$ west longitude. The depth

throughout this area is between 125 and 150 feet (38 and 45 meters). The barge is towed to sea approximately two to three times a week. Until May of 1974 the discharge time was usually about 60 minutes at a speed of 6 knots, weather and other conditions permitting. Then, a new bow tie dump pattern was adopted with a discharge time of about five hours at a speed of eight knots. The waste originally was 17% to 23% acid (expressed as H_2SO_4) and 4 to 10 percent ferrous sulfate (Falk et al., 1974). During 1975 the composition of the waste was changed to a solution of 10% acid (expressed as HCl) and 4% iron as iron chloride salts (EPA, 1975). Similar wastes have been disposed at sea for 28 years in the New York Bight (Peschiera and Preiherr, 1968).

A limited amount of information on the waste disposal site is given by Hydrographic Office bathymetric charts and in papers by Bumpus (1965, 1969), Bumpus and Lauzier (1965), Bumpus, et al. (1973), Ketchum (1953), and Myers (1974). Their work included releases of bottom drifters and surface floats. Bumpus has established a line parallel to shore at approximately 30 to 35 fathoms inside of which bottom drifters move shoreward while drifters released outside of the line move offshore. This lines lies approximately 43 miles off the coast of Delaware. Myers (1974) found that isothermal conditions prevailed throughout the water column until mid-April, when a distinct thermocline formed between 18 and 23 meters depth.

A study conducted by Falk, et al. (1974) at the time when the waste was disposed in a one-hour period, included Eulerian type current measurements with current meters. They found that the ocean currents were southwesterly at the bottom. In the summer, the stratified surface waters moved north or northwesterly. The general movement of the waste field was to the southwest, except during late spring and summer when the wastes above the thermocline moved to the northwest.

4.2 Satellite Observations

The frequency of the dumping made it possible for Landsat satellites and aircraft to observe the waste plumes in various stages of degradation, ranging from minutes to days after dump completion (Figure 4.2). As shown in Table 4.1, 22 satellite images were found which show water discoloration in the general vicinity of the waste dump site. The spectral characteristics and position of the discoloration, the dump pattern and the time difference between the dump and photograph gave strong indications that the discolorations are the waste plume (Figure 4.3).

Several forms of Landsat imagery were used, ranging from the 70mm transparencies to the original magnetic tapes. Before visual interpretation, some of the imagery was enhanced optically. Maps and print-outs of the waste plumes were prepared by computer analysis of digital tapes and by direct photo interpretation of the transparencies.

Compared with the waste plume in Figures 4.3, imaged immediately after dump completion, the plume in Figures 4.4, imaged three and one-half hours after dump, is considerably more dispersed. Digital radiometric print-outs of the waste plumes are presently being correlated with concentrations of dissolved and particulate substances, such as iron, samples from boats at the time of the aircraft and satellite overpass. The change in concentration over cross-sections of the plume are used to determine dispersion properties of the waste. Spectrometers deployed from helicopters and boats have also been used to determine spectral signatures of waste plumes such as the one in Figures 4.3. Spectrometric measurements indicate that upon combining with seawater, the waste develops a strong reflectance peak in the 0.55 to 0.60 micron region, resulting in a stronger contrast in the LANDSAT Band 4 than the other bands. This spectral appearance seems to be caused by the formation of a sparse but optically persistent suspended ferric floc.

Table 4.1

WASTE PLUME CHARACTERISTICS DERIVED FROM LANDSAT IMAGERY

	Date	Hours After Dump	Lateral Extent (N.M.)	(N to S) Axis Orientation	Distance Between Centroids (N.M.)	Axis Orientation	Average Drift Velocity (knots)
1)	10/10/72	(9h38)	10.0	155°	8.5	250°	.88
2)	10/27/72	(14h08)	5.0	260°	4.0	225°	.28
3)	01/25/73	(3h03)	5.0	120°	4.5	275°	1.48
4)	04/07/73	(6h38)	8.0	110°	3.0	280°	.45
5)	05/13/73	(during)	1.0	105°	3.0	260°	--
6)	10/22/73	(29h30)	14.5	225°	12.0	195°	.41
7)	10/23/73	(53h36)	14.0	200°	24.5	215°	.46
8)	12/15/73	(4h45)	--	--	--	--	--
9)	03/15/74	(6h08)	--	--	--	--	--
10)	04/20/74	(13h47)	7.0	145°	7.0	215°	.51
11)	05/26/74	(24h20)	7.5	145°	10.5	235°	.48
12)	11/04/74	(14h00)	7.0	240°	3.5	120°	.28
13)	08/18/75	(during)	7.5	120°	1.5	160°	--
14)	08/28/75	(during)	6.0	220°	1.5	270°	--
15)	10/21/75	(6h35)	8.0	250°	6.4	188°	.97
16)	11/17/75	(5h00)	8.0	120°	2.0	160°	.40
17)	01/19/76	(3h00)	6.5	245°	2.0	245°	.67
18)	02/24/76	(6h00)	10.0	105°	4.0	135°	.67
19)	04/18/76	(70h19)	--	--	--	--	--
20)	06/20/76	--	--	--	--	--	--
21)	07/17/76	--	--	--	--	--	--
22)	08/22/76	--	--	--	--	--	--
	AVERAGE		7.8	175.9°	5.3	206.4°	.59

4.3 Application of Current Drogues

A total of nine cruises were made to the acid waste disposal site during the period from May 1975 to June 1976, to launch radio-signal-emitting current drogues. Four of the cruises were made when a summer thermocline was present. The other five cruises were made during the winter months when isothermal conditions existed in this area. During each cruise three or four current drogues were deployed to measure currents at the surface, mid-depth or above the thermocline, and below the thermocline. Also weather and sea conditions were noted during each cruise and a temperature profile was made to determine the presence and depth of the thermocline.

The drogues used are dispensable units, costing about $200 each, developed by the Electro-Physics Laboratories of the I.T.T. Avoinics Division (Klemas et al., 1974). Each drogue consists of a two-foot length of plastic pipe containing all electronics (Figure 4.5). Buoyancy is provided by a pair of flotation chambers so attached that when properly ballasted, the antenna portion of the drogue projects 75 inches above a still sea datum plane. The transmitter broadcasts less than 100 milliwatts of power in the 2- to 6-megahertz band. When using the sea surface as a ground plane and transmitting via ground wave, ranges in excess of 100 miles have been obtained. The drogue's operating life is selectable from one to six weeks through choice of battery type and control of transmitter power (Klemas et al., 1974).

Current sensing is achieved by the use of a current trap, e.g. a biplane, which is suspended at a controllable depth beneath the drogue hull. The current intercept area is isotropic and ranged from 10 square feet for surface drogues to 16 square feet for subsurface drogues. A ballast weight is attached to the bottom of the current trap in order to provide a righting

moment about the system's metacenter to resist heelover under strong wind and wave conditions. Since the buoy portion of the drogue is nearly awash and has only a thin radio antenna protruding above the water surface, wind drag on the drogues was usually not significant. A ratio in excess of 20:1 was maintained between the projected area of the buoy exposed to surface currents and of the current trap exposed to currents at its depth. Careful hydrodynamic design of the buoy hull structure further reduces the effect of surface currents.

Position finding is accomplished by triangulation from two (or more) radio direction-finding (DF) stations located on-shore near the water's edge. The loop antenna used on the DF sets is highly directional and permits an accurate audio null of the received signal. Ideally the baseline between DF stations should be such that the bearing lines from the stations to each drogue intersect are as close to a right angle as possible. At an average distance to a drogue of 64 km a standard deviation in bearing angle of about 1 degree was obtained. To maintain this accuracy, each DF set must be recalibrated on a moored drogue before each series of measurements. Best results were obtained for tracking ranges of 16 km to about 96 km.
The triangulation method gives large position errors for drogues moving to the outer portion of the shelf. Therefore, for studies covering distant segments of the shelf more expensive drogue designs will have to be considered, e.g. drogues which contain LORAN or OMEGA repeaters.

4.4 Discussion of Results

As shown in Table 4.1 and Fig. 4.6, the maximum range of measurable wastes estimated by Falk et al. (1974) as being about ten nautical miles from the discharge point was substantiated by the satellite imagery since only one out of sixteen plumes was observed to be significantly beyond this range.

This was also the only plume observed by the satellite as being 32 km from shore with two others about 40 km from shore, and all remaining nineteen plumes more than 48 km from shore.

Waste plume drift velocities derived from Landsat imagery and shown in Figures 4.7 ranged from 0.25 knot to 1.48 knots, with an average of 0.59 knot. Plume drift velocities were calculated by dividing the distance between plume centroid and the center of the waste dump site by the time between dump and satellite overpass. The dump time was defined as the midpoint between waste dump initiation and completion. Barge captain's logs were consulted to validate this procedure. Our own observations confirm the contention that most of the waste dumps are centered on the proper site.

A total of 35 current drogues were released at the waste disposal site, during the time period from May 1975 through June 1976. The drogues were successfully tracked from one to 13 days, with the average tracking period being about five days. The average drift velocities of surface drogues ranged from 0.05 knot to 1.9 knots, with a combined average of 0.50 knot for all surface drogues. For mid-depth drogues the velocities ranged from 0.02 knot to 1.42 knot with a combined average of 0.46 knot. The near-bottom drogues moved at average velocities of 0.06 knot to 1.2 knots, with a combined average of 0.36 knot. However, since only several near-bottom drogues survived for more than two days, near-bottom results may not represent "typical" conditions.

Most of the current drogues, which were part of another study, were not released or being tracked during satellite overpasses. However, the average magnitudes of waste plume and drogue drift velocities are compatible with each other and with net current velocities measured by Falk et al. (1974), including their maximum recorded net drift velocity of 8.7 miles per

day (0.44 knot). Drogues were being released at the time of the 21 October 1975 pass of Landsat over an acid waste plume (Table 4.1). During the first six hours after dump the waste plume had drifted south (188° azimuth) at a velocity of 0.97 knot. During the same period the near surface drogue (Fig. 4.8) south-southeast (175° aximuth) at 1.06 knots and the 20 meter depth drogue (Fig. 4 drifted to the south-southwest (190° azimuth) at 0.85 knot. Since the waste plume disperses during the first few hours over intermediate depths, its drift direction and velocity lie between those of the two drogues. Twenty-four hours later the same plume was observed by aircraft at a distance of about 6.4 miles and an azimuth direction of 166° from its location in the satellite image. The slowing of the plume drift velocity to 0.47 knot and change in direction indicates that, similar to the drogues, a northeasterly current component has been temporarily superimposed on the southward movement. The cause of this northeast current was most likely a steady 20 knot wind from the west which developed during that same period.

During the stratified warm months, more drogues tended to move in the north-northeast direction while during the non-stratified winter months a southwest direction was preferred. These results do not conflict with previous studies which found that there was a mean flow to the southwest, with stratified surface waters moving in the northerly or northwesterly direction during the summer (Boicourt and Hacker, 1974). Identical drogues released at equal depths generally followed similar paths. However, drogues released at different depths frequently traveled not only along different paths, but also a different speeds indicating the presence of current shear.

Most rapid movement of the drogues at all depths occured during a severe northeaster storm with drogue velocities in excess of 1.8 knots being attained. Thus the circulation process at the waste dump site appears to be highly storm-dominated with an increase of water transport occurring

during storms, particularly northeasters. This conclusion is in agreement with results obtained by other investigators in the Middle Atlantic Bight (Beardsley and Butman, 1974).

As shown in Figures 4.10, a distinct summer thermocline was observed from June through August of 1975 at depths ranging from 43 to 103 feet (13 to 24 meters). In 1976 the first observation of a thermocline again occurred in June. The strongest thermocline was observed on 19 August 1975, having a change of temperature from 23°C to 8°C between depths of 13 and 20 meters, respectively. In comparison, Myers (1974) observed the formation of a thermocline at the same site during April of 1973 at depths between 18 and 23 meters. Ocean stratification conditions influence waste dispersion. The wastes do not reach the ocean bottom when a thermocline is present. They are distributed from top to bottom when the ocean is isothermal (Falk et al., 1974).

4.5 Conclusions

Satellites such as Landsat offer an effective means of assessing the drift and dispersion of industrial wastes dumped on the continental shelf. This is particularly true for the acid wastes disposal site approximately 64 km off the Delaware coast. These wastes form a sparse but optically persistent ferric floc which can be observed by Landsat's multispectral scanner band 4 up to three days after dump.

Most of the 22 waste plumes imaged by Landsat were found to be drifting at average rates of 0.28 knot to 1.83 knots into the southwest quadrant. The plumes seemed to remain above the thermocline which was observed to form from June through August at depths ranging from 13 to 31 meters. During the remainder of the year, the ocean at the test site was not stratified, permitting wastes to mix throughout the water column to the bottom.

The magnitudes of plume drift velocities were compatible with the drift velocities of current drogues released over a twelve month period at the surface, at mid-depth and near the bottom. However, during the stratified warm months, more drogues tended to move in the north-northeast direction, while during the non-stratified winter months a southwest direction was preferred. Drogues released at different depths frequently traveled along different paths and at different speeds, indicating the presence of current shear.

Rapid movement toward shore occurs primarily during storms, particularly northeasters. During such storms, however, the plume is rapidly dispersed and diluted. Therefore, the probability of an identifiable plume containing heavy concentrations of waste reaching the shore is quite low.

4.6 References

Beardsley, R. C. and B. Butman. (1974) Circulation on New England Continental Shelves: Response to Strong Winter Storms. Geophys. Res. Letters 1(4): 181-184.

Boicourt and Hacker. (1974) Personal Communication.

Bumpus, D. F. (1965) Residual drift along the bottom on the continental shelf in the Middle Atlantic Bight area. Limnol. Oceanogr., Suppl. to Vol. X (Redfield volume), R50-R53.

Bumpus, D. F. (1969) Reversals in the surface drift in the Middle Atlantic Bight area. Deep-Sea Res., Suppl. to 16: 17-23.

Bumpus, D. F. and L. M. Lauzier. (1965) Surface circulation on the continental shelf off eastern North America between Newfoundland and Florida. Amer. Geographical Soc., New York, Folio 7, Serial Atlas of the Marine Environ.

Bumpus, D. F., et al. (1973) Physical Oceanography. In: Coastal and Offshore Environmental Inventory, Cape Hatteras to Nantucket Shoals. Marine Publ. Series No. 2, Univ. Rhode Island, Kingston, R.I., pp. 1-28 to 1-33.

Environmental Protection Agency. (1975) Interim ocean dumping permit DE006, Issued to E. I. duPont de Nemours and Co., Inc. by the U. S. Environmental Protection Agency, Region III, Philadelphia, Pennsylvania.

Fader, S. W. (1972) Barging industrial liquid wates to the sea. J. Water Poll. Control Fed. 44(2): 314-318.

Falk, L. L., et al. (1974) Waste dispersion characteristics and effects in an oceanic environment. Rept. prepared for U. S. Environmental Agency, Program No. 12020 EAW.

Ketchum, H. (1953) Preliminary evaluation of the coastal water off Delaware Bay for the disposal of industrial wastes. Unpubl. manuscript, Ref. No. 53-31, Woods Hole Oceanographic Inst., Woods Hole, Massachusetts.

Klemas, V., et al. (1974) A cost-effective satellite-aircraft-drogue approach for studying estuarine circulation and shelf waste dispersion. Proc. Ocean 75 Conf., San Diego, Calif.

Myers, T. D. (1974) An observation of rapid thermocline formation in the Middle-Atlantic Bight. Est. and Coastal Mar. Sci. 2: 74-82.

Peschiera, L. and F. H. Freiherr. (1968) Disposal of titanium pigment process wastes. J. Water Poll. Control Fed. 41(1): 127-131.

4.7 List of Figures

Figure 4.1: Location of DuPont ocean waste disposal site.

Figure 4.2: DuPont waste plume images during dump on 28 August 1975 by an aircraft flying at 12,000 feet altitude.

Figure 4.3: DuPont waste plume visible in Landsat imagery on 28 August 1975 (during dump).

Figure 4.4: DuPont waste plume visible in Landsat imagery on 24 February 1976 (6 hours after dump).

Figure 4.5: Deep current drogue with low parasitic drag (Model 3).

Figure 4.6: Distance from center of dump site to centroid of waste plume imaged by Landsat.

Figure 4.7: Drift velocities of acid waste plumes obtained from Landsat imagery (units = knots).

Figure 4.8: Drift tracks of near-surface current drogue released on October 21 and tracked until October 25, 1975.

Figure 4.9: Drift tracks of 20 meter depth current drogue released on October 21 and tracked until October 25, 1975.

Figure 4.10: Temperature profiles obtained with an Expendable Bathythermograph show water stratification and thermocline location during summer months.

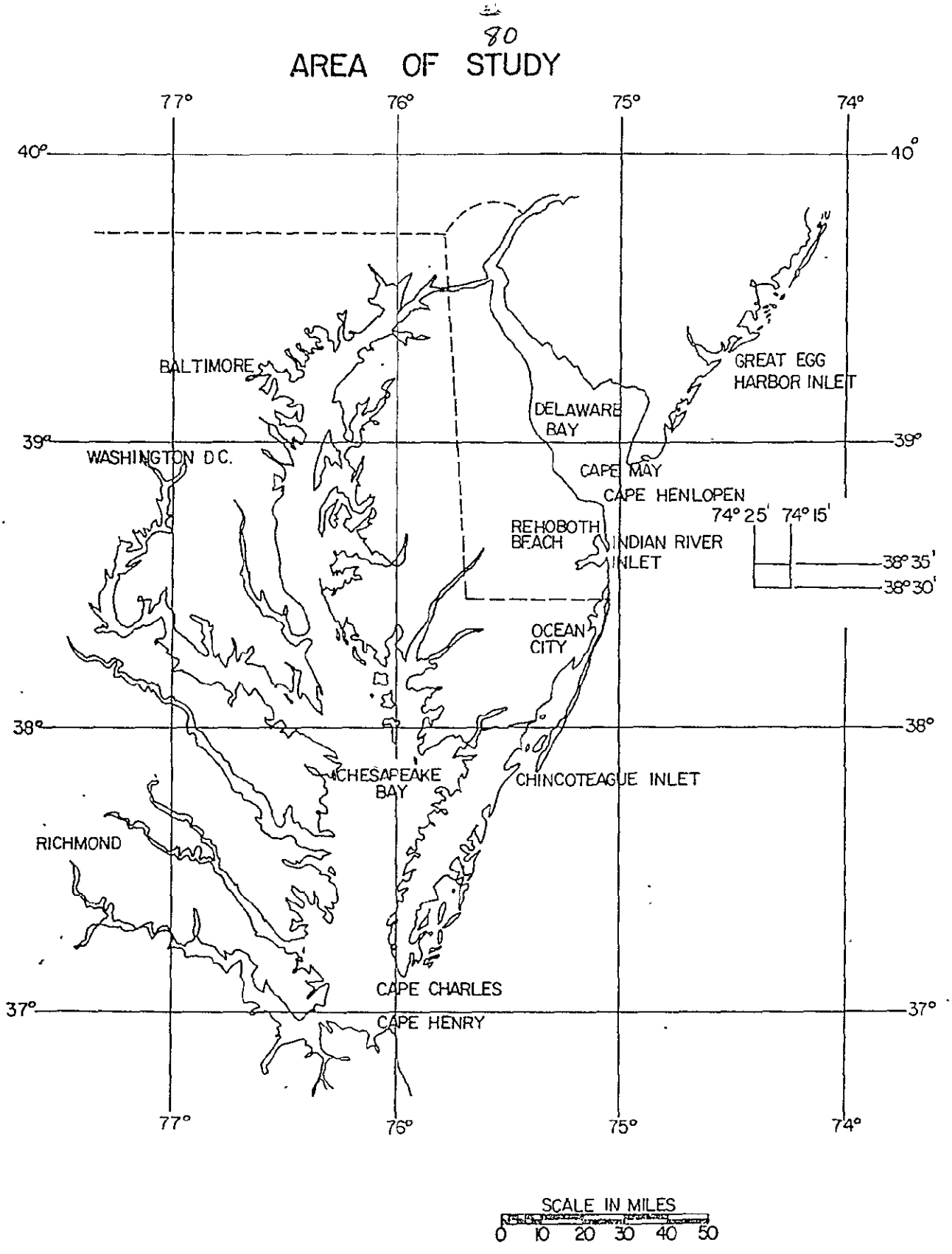

Figure 4.1. Location of DuPont ocean waste disposal site.

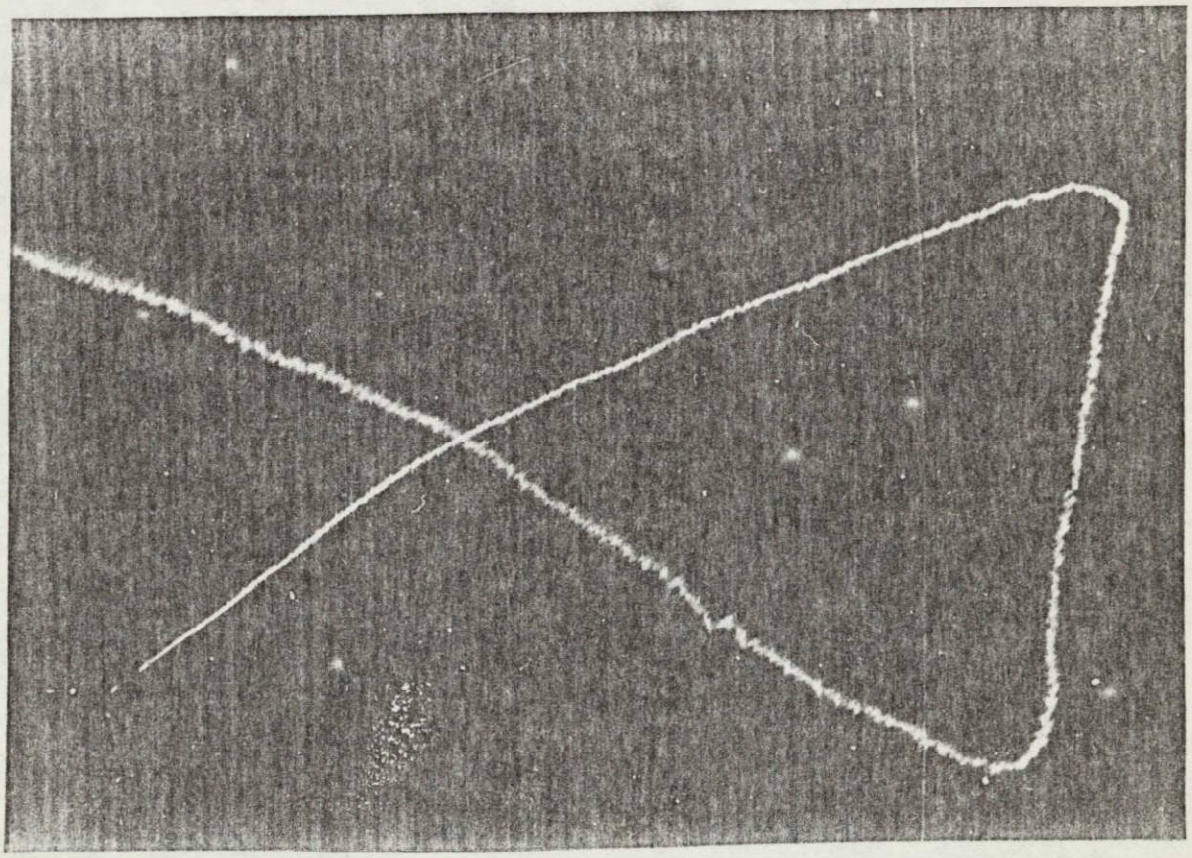

Figure 4.2. DuPont waste plume images during dump on 28 August 1975 by an aircraft flying at 12,000 feet altitude.

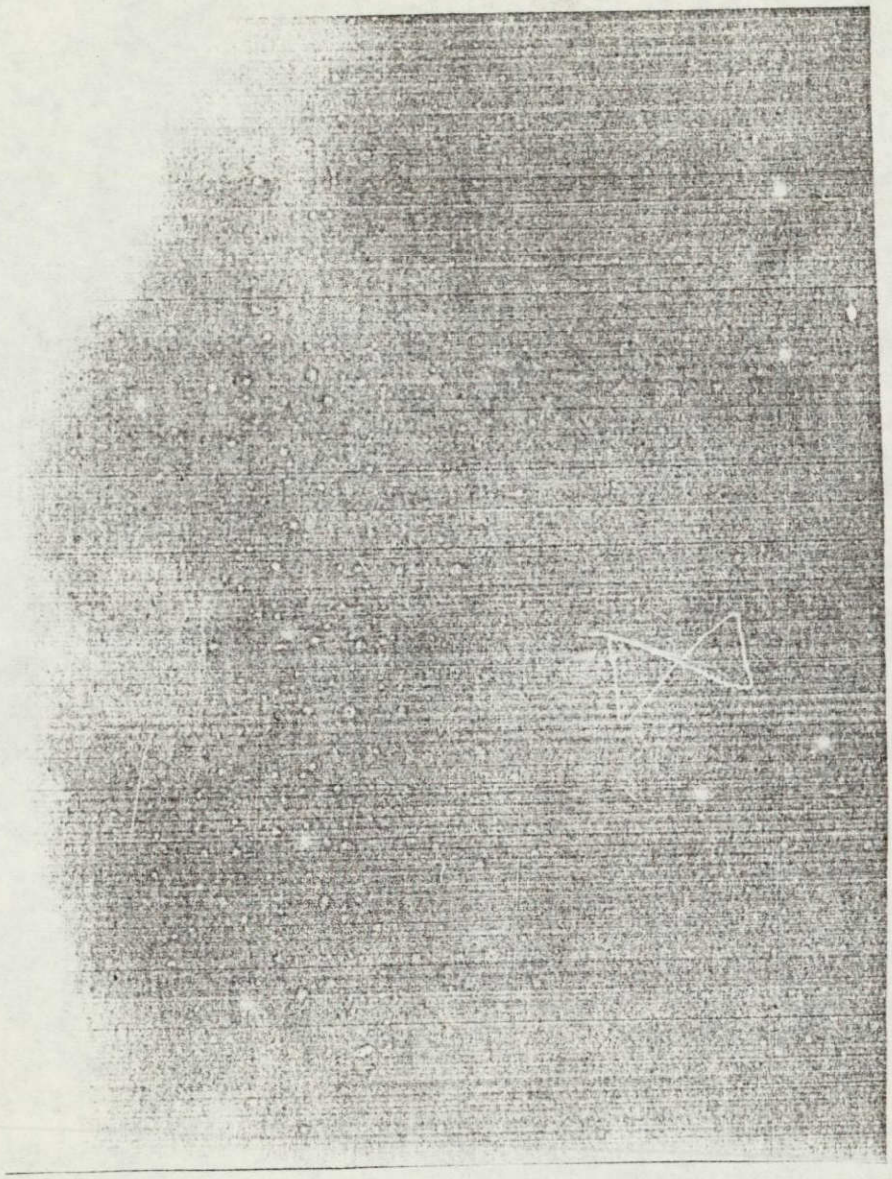

Figure 4.3. DuPont waste plume visible in Landsat imagery on 28 August 1975 (during dump).

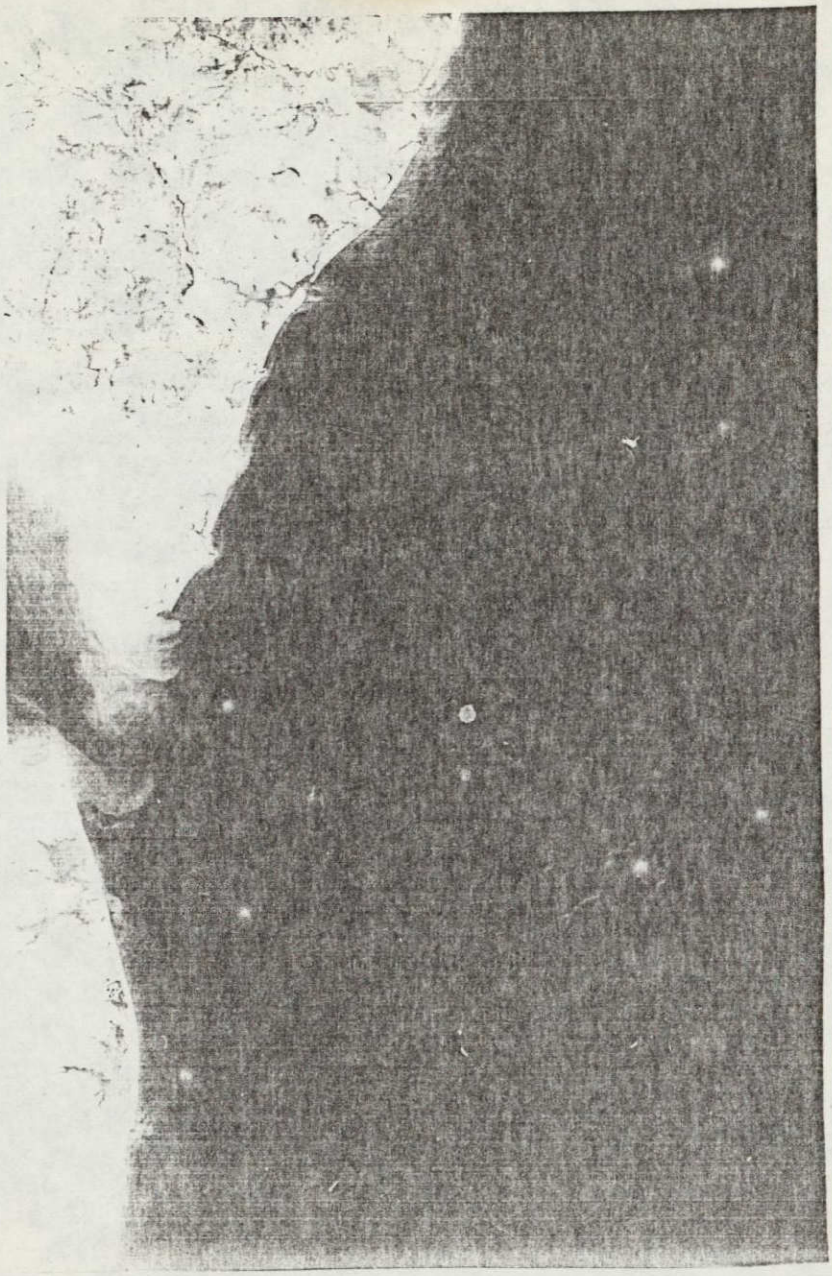

Figure 4.4. DuPont waste plume visible in Landsat imagery on 24 February 1976 (6 hours after dump).

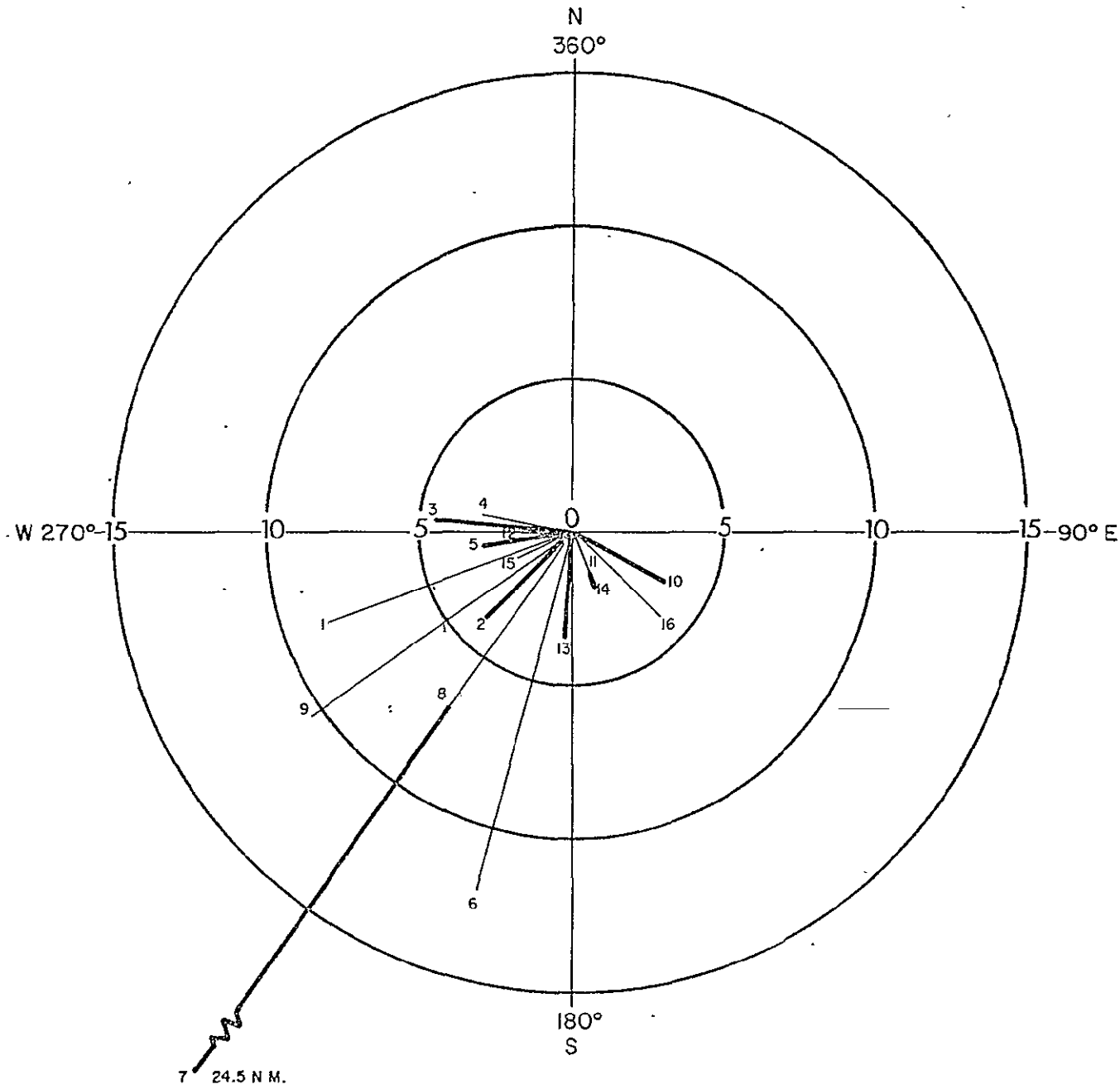

Figure 4.6. Distance from center of dump site to centroid of waste plume imaged by Landsat.

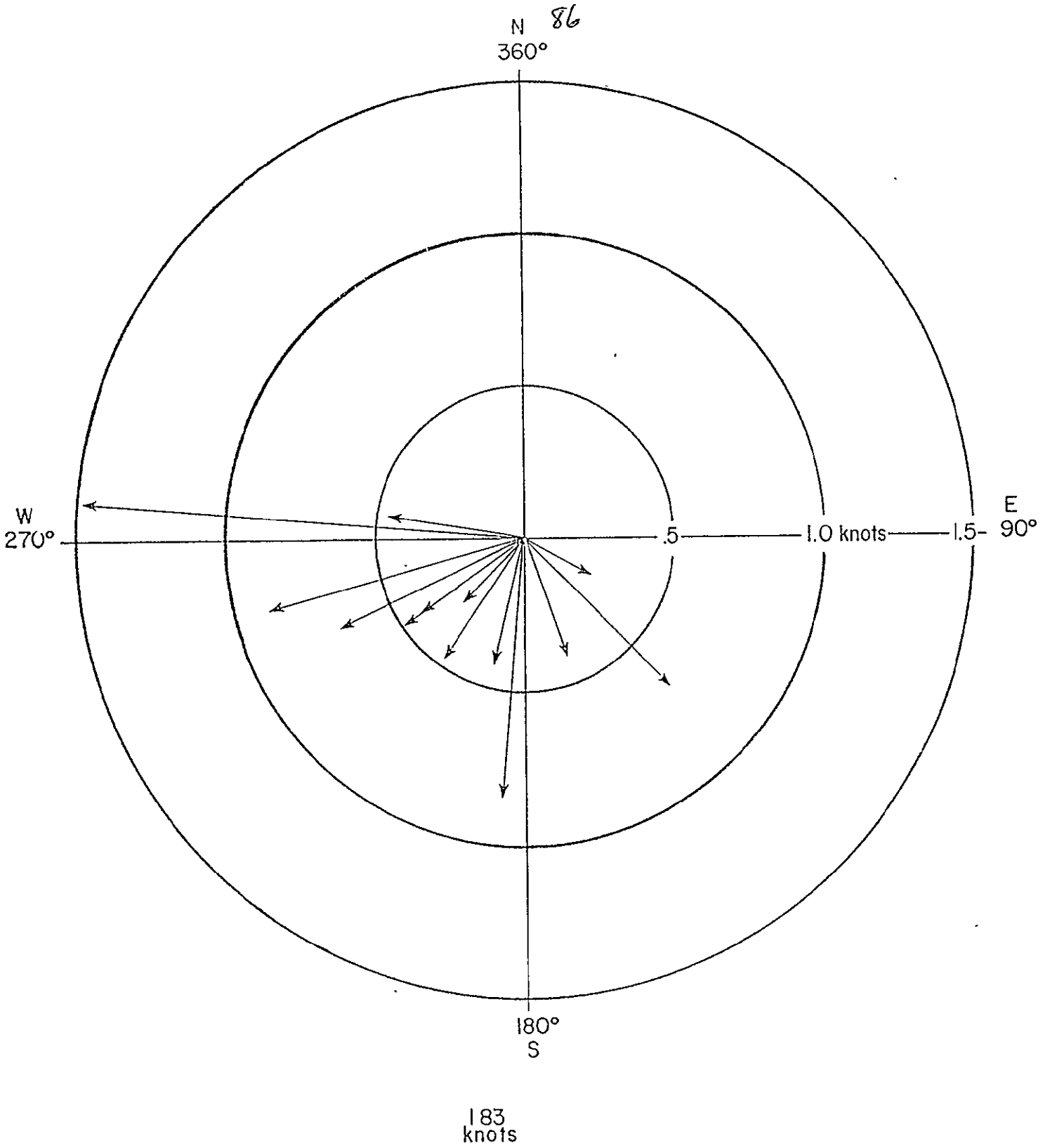

Figure 4.7

Drift velocities of acid waste plumes obtained from Landsat imagery (units = knots).

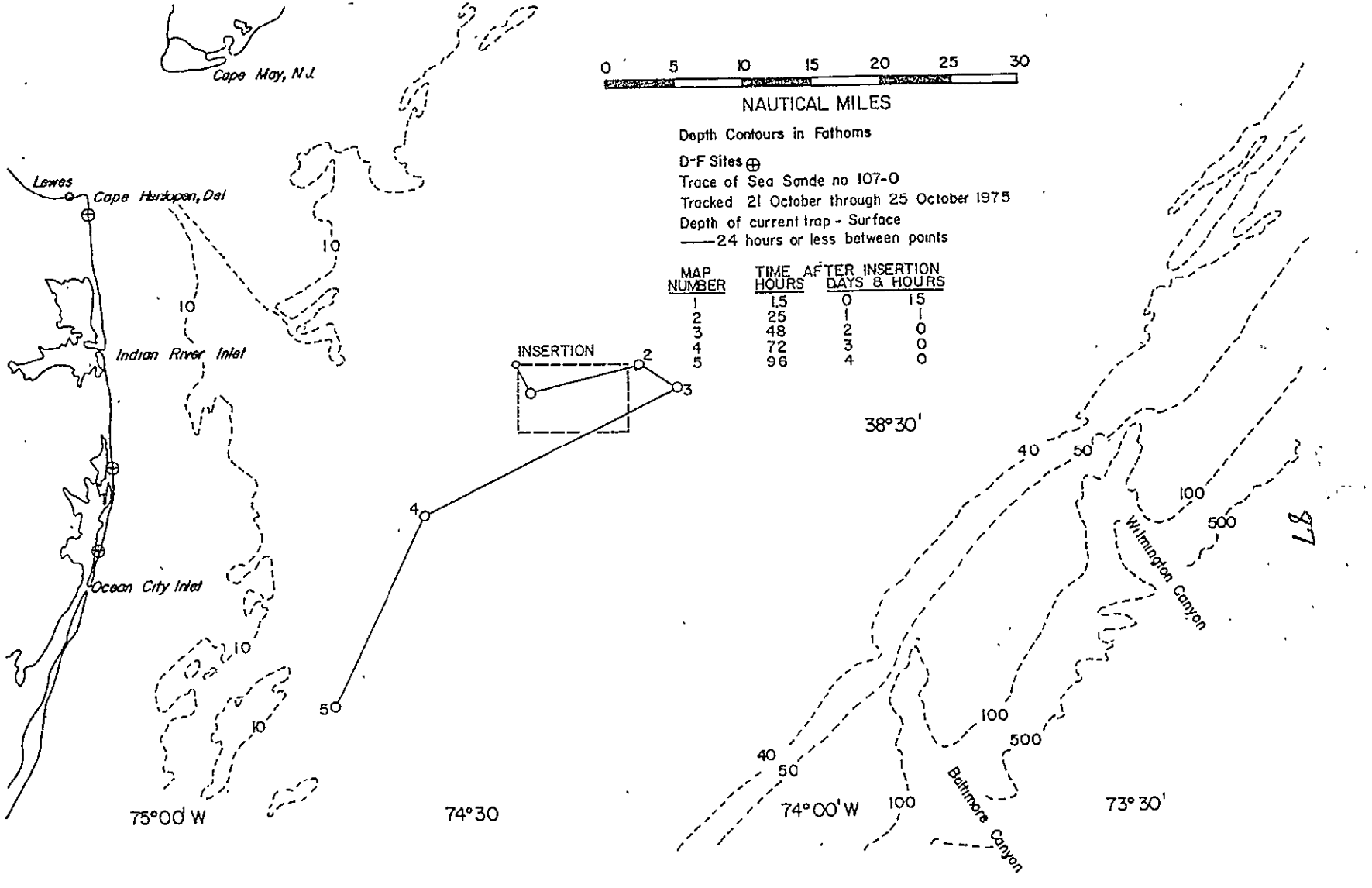

Figure 4.8. Drift tracks of near-surface current drogue released on October 21 and tracked until October 25, 1975.

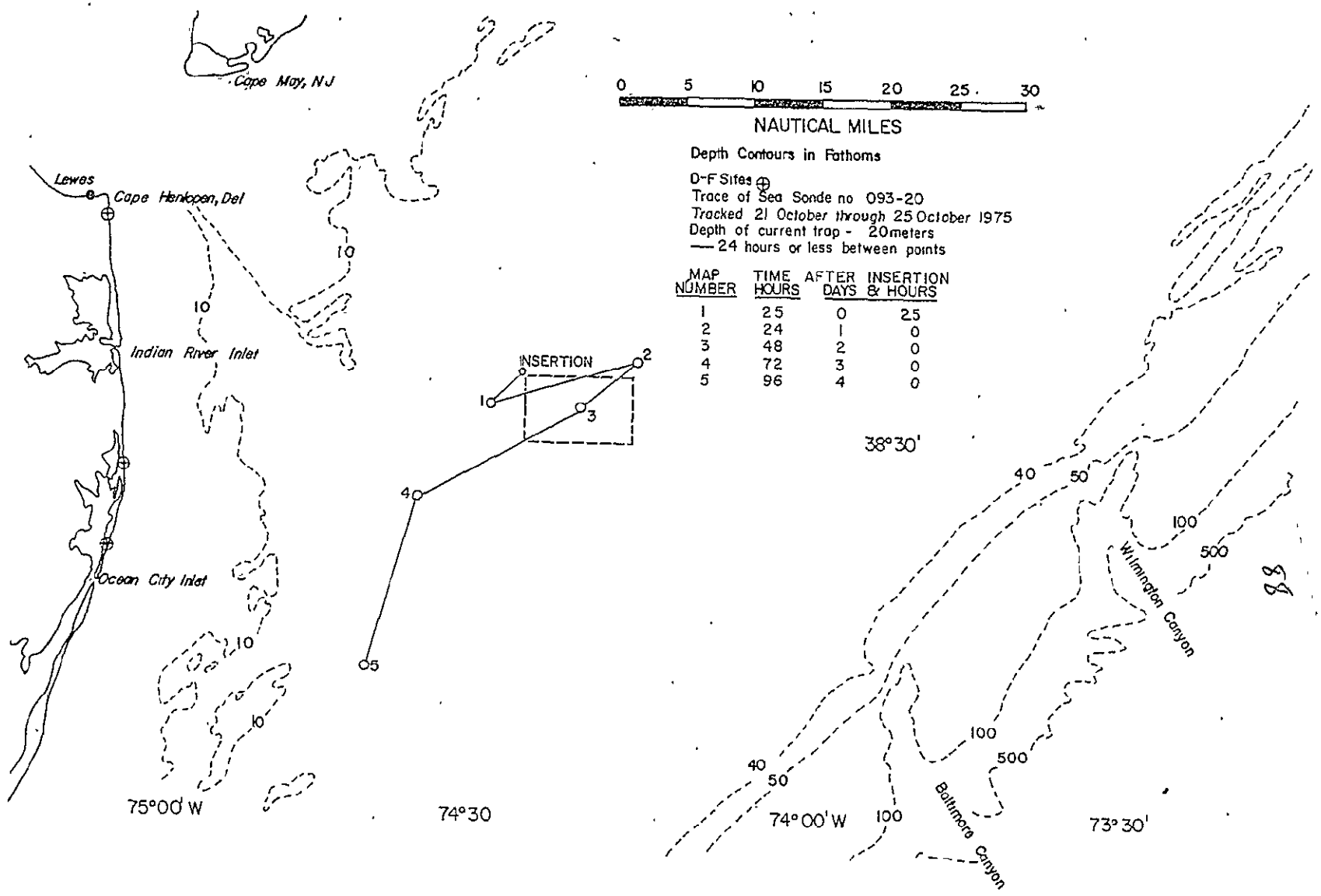

Figure 4.9. Drift tracks of 20 meter depth current drogue released on October 21 and tracked until October 25, 1975.

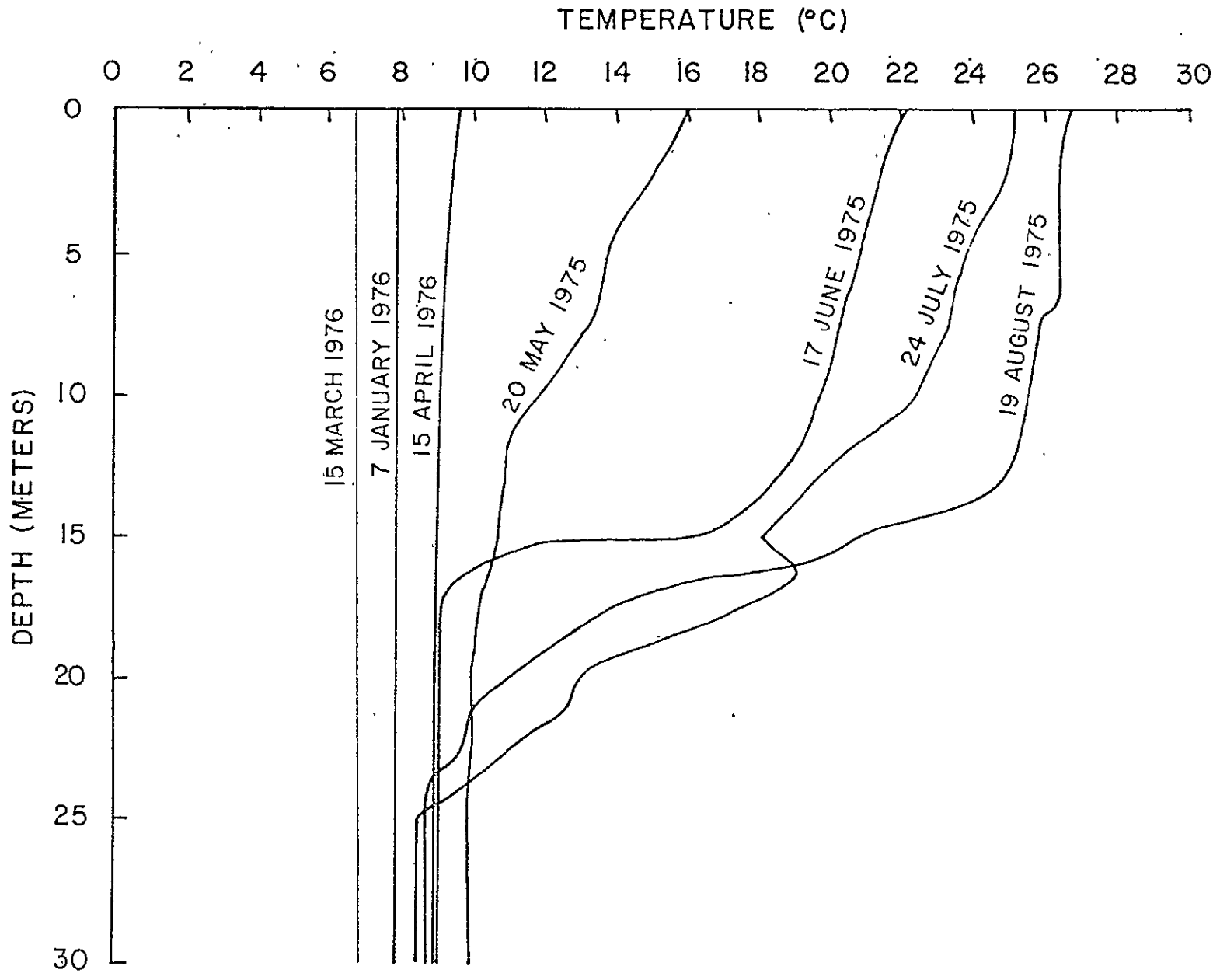

Figure 4.10. Temperature profiles obtained with an Expendable Bathythermograph show water stratifiction and thermocline location during summer months.

V. COASTAL VEGETATION STUDIES

5.1 Introduction

The technology for automated analysis of multispectral data has been developed and refined over the past several years, particularly in response to the extensive data available from Landsat's 1 and 2. Classification algorithms, hardware and software functions and the variety and quality of output products have reached a high level of efficiency and sophistication. Nevertheless, the accuracy and utility of the information output of supervised, digital classification schemes ultimately relies on the investigator's knowledge of the spectral properties of the cover types of interest and the effectiveness with which he can incorporate his knowledge into the automated analysis procedure. This critical process of training the computer to recognize and discriminate the spectral characteristics of specified targets has traditionally been accomplished through the identification of "training areas" within the satellite data itself. Usually, the investigator locates several geographical areas which he is confident represent the cover types to be discriminated. The scanner radiance measurements for these training areas are then edited and used by the computer to provide a statistical characterization or "signature" for each of the desired cover classes. This procedure has several advantages over alternate training techniques which are responsible for its current widespread use.

The primary advantage of "training areas" is that only geographical, rather than spectral, characterization of cover types is required of the investigator. He need know very little of the spectral properties of the desired targets if he can simply locate representative sample areas and use the scanner measurements to derive spectral radiance signatures. There are

of factors other than reflectance allow significant relationships between reflectance and other environmental characteristics to be recognized.

c) Radiance measurements transformed to "absolute reflectance" through application of atmospheric corrections may be manipulated and extended independent of the solar and atmospheric conditions present during satellite overpasses. Training data may be applied to analysis of any overpass for which atmospheric correction has been performed without recourse to ratioing techniques. In detection of change over time such extension of signatures will be critical.

This report describes a technique for obtaining Landsat/MSS-equivalent spectral radiances in situ and the transformation of these and actual MSS data to atmospherically corrected reflectance values. The use of this data in training automated analysis of Landsat data over Delaware's tidal wetlands is also shown along with an evaluation of environmental sources of variation in visible/near IR reflectance properties of wetlands cover types.

5.2 Methods

Evaluation of the atmospheric correction technique and, in particular, of the use of in situ measurements of target reflectance to train multispectral analysis may be divided into two efforts -- 1) Field Studies, which include:

a) Atmospheric, solar and target measurements made at or near the time of the Landsat overpass. These measurements were used in the actual atmospheric correction and analysis of the Landsat data.

b) Target reflectance measurements made through the study period for the purposes of assessing variability in those reflectances and in order to accumulate a bank of data for use in tests of in situ measured

other, more secondary, advantages but most are related to the inherent ease of development of sample data. There are, however, several ways in which this type of training may potentially restrict the speed, accuracy and utility of the automated information extraction process:

1) The investigator must have ground truth information over large areas of the scene to be categorized. The information must be up to date and the training areas must be located precisely in the raw data image. Failure in any of these respects may result in choosing a training set which is not representative of the category the investigator desires, either through insufficient knowledge of the area or through mislocation of, or subsequent changes occurring in the training sample areas selected.

2) The training sample for each category must consist of a large enough number of independent measurements (20-50 scanner picture elements) to provide a statistically significant data set from which to derive a multispectral signature. The investigator is confronted with using training data integrated over areas 20-50 times the smallest area which the scanner's instantaneous field of view (IFOV) actually allows him to detect. Thus, analysis of smaller scale phenomena which may be discernable by the scanner is limited. In discrimination of plant types, for instance, even if a large enough monospecific stand for training is available, intraspecific variability on a smaller scale may be integrated into the generalized signature obtained. If such small scale variability is accessible to the IFOV of the scanner then information of potential value is lost through the use of large training areas.

3) Finally, the spectral signatures obtained are based upon the radiance measured by the satellite and do not account for atmospheric and solar dependence of that reflected radiance or modifications of the signal

as it is transmitted from the target to the scanner. The use of relative radiance training areas thus complicates the extension of signatures obtained under one set of atmospheric conditions to data obtained under other conditions. Gross assumptions about atmospheric variability or ratioing techniques must be employed if new training data is not derived for each new scanner overpass.

An alternative training procedure is available through technology and instrumentation for in situ measurement of cover type radiance and subsequent transformation of this data to atmopsherically corrected reflectance. Measurement of atmospheric and solar parameters at the time of satellite overpasses also allows transformation of in situ measured radiances to satellite measured equivalents. In situ measurements of spectral characteristics, applied to atmospherically corrected satellite data, may produce a significant improvement in training sample quality for many applications. Specifically,

a) While ground truth is still required it would not be necessary to locate the geographic coordinates of sample areas precisely nor would the information have to be updated frequently. Reflectance over a particular cover type under known environmental conditions will be representative regardless of any changes which subsequently occur in the sample area.

b) Measurement on the ground allows selection of training samples without the large area restriction of the "training area" approach. Thus, training data may be collected over areas too small to provide an adequate training area, allowing detection and monitoring of phenomena down to the IFOV restriction of the scanner. Further, an investigator on the ground can be much more efficient in recording the conditions present in the specific site he has sampled. Such sampling accompanied by measurements

reflectance signatures in training of the computer analysis.

and, 2) Landsat Data Processing and Evaluation of Classified Products, in which Landsat data from a selected date was classified using atmospheric correction with in situ reflectance for training and the results compared with those achieved using conventional "training area" analysis.

5.21 Field Studies

The Bendix Radiant Power Measuring Instrument (RPMI) was used to measure atmospheric parameters necessary to tranform Landsat data and in situ measurements of radiance to equivalent reflectance values. Equation (1), below, was used in transforming target radiance (L) to reflectance (ρ) through normalization by the appropriate solar and atmospheric parameters: solar zenith angle (Z), direct solar irradiation (H_{sun}) and sky-light irradiation (H_{sky}).

$$\rho = \frac{\pi L}{H_{sun}\ CosZ + H_{sky}} \qquad (1) \quad \text{(Rogers et al., 1973)}$$

Direct solar irradiance (H_{sun}) is measured by placing a field restricting tube (7° solid angle field of view) over the RPMI sensor head and pointing the head directly at the sun. As is the case for all radiant power measurements, four bandpass filters corresponding to the Landsat-MSS bands are rotated in front of the detector and a value for each band is read in mw/cm^2 (or $mw/cm^2/sr$ for radiance measurements) from the meter assembly. The measurement of sky-light irradiation (H_{sky}) is made by removing the field restricting tube, leveling the instrument and shading the cosine response detector head from direct sunlight. A measurement of total global irradiance (H) equivalent to (H_{sun} Cos Z + H_{sky}) can be made with the leveled, unshaded RPMI. For

measurements of target radiance (L) the RPMI detector, with field restricting tube in place, is directed at the target surface and radiance in the four MSS-equivalent bands is recorded.

A large number of measurements of sample target reflectances were obtained between July 1974 and August 1977. Test targets chosen for study were:

1) The "Salt Marsh Cord Grass" (Spartina alterniflora) community,

2) The "Salt Hay" (Spartina patens and Distichlis spicata) community, and

3) Unvegetated tidal mud flat.

In addition, areas of open water were identified in order to facilitate registration of data sources based on land/water boundaries. These three wetland communities, along with adjacent tidal waters, constitute the vast majority of Delaware's marsh areas and knowledge of their distribution allows valuable inferences to be made concerning the tidal regimes and marine and terrestrial animal habitats present. In all, over 200 target measurements were made over the three primary test cover types, along with the necessary atmospheric measurements for conversion of target radiance to percent reflectance through equation (1) above. In addition, a standard reflectance panel was routinely measured as a test of the measurement and correction procedures. Physical and environmental observations of the test targets, such as plant height, biomass and tidal stage, were made at the time of radiance measurements and later correlated with reflectance. Biomass samples were harvested from .25 m^2 measured plots, sorted into live, dead emergent and litter classes, dried for 48 hours at 65°C and weighed.

5.22 Landsat Data Processing and Evaluation of Classified Results

Landsat multispectral data analysis was performed at the Bendix Earth Resources Data Center. The center's "M-DAS" analysis system consists of a Digital Equipment Corporation PDP-11/75 computer; two 1.5 million word disk packs; two nine-track 800 bpi tape drives; line printer; card reader and teletype unit. Specialized equipment includes a 14-track tape recorder; a hard-wired, special purpose computer for processing multispectral data; a 70 mm laser film recorder for recording data on film; and a color, moving window, computer-refreshed television display. In addition, a Calcomp digital plotter was used to reproduce classified data at specified map scales.

Each of four test wetland areas was classified twice -- first, using the conventional "training area" approach and then again, utilizing atmospheric correction and in situ measurements of reflectance for training. The "training area" approach was used in both cases for the categorization of water in order to provide maximum uniformity of water boundaries used in registering the comparison data sources during accuracy verification.

Atmospheric and solar normalization of Landsat data was implemented through equation (2), transforming MSS radiance measurements (R) to percent reflectance (ρ) in each band.

$$\rho = \frac{R - L_A}{H \cdot \frac{H_{sun}\ (\cos Z)}{H_o}} \qquad (2)$$ (Rogers et al., 1973)

Total global irradiance (H), solar zenith angle (Z), and direct solar irradiance (H_{sun}) were measured using the RPMI. The beam transmittance term,

$$\frac{H_{sun}\ (\text{Cos } Z)}{H_o}$$

was computed using known values for solar irradiation outside the atmosphere (H_o) (Thekaekara, 1971). The remaining value necessary for solution of equation (2) is path radiance (L_A). The direct measurement of this parameter is impossible, but its value may be inferred by one of two procedures: 1) an equivalent value may be obtained with the RPMI if solar elevation is < 45° by orienting the instrument at the same scattering angle with respect to the sun as the Landsat sensor or 2) known reflectances (ρ) of targets on the ground may be used to empirically derive path radiance by solving equation (2) for L_A. In this case, the empirical approach was used. Two large, relatively homogenous targets of known reflectance were available which could be readily identified and extracted from the Landsat-MSS data: 1) one of several large areas of Spartina alterniflora could be used since a number of measurements of reflectance of this species were made as part of the study, and 2) reflectance of water around the known position of the RPMI was obtained at the time of the October 18 overpass. These two targets, having relatively low reflectance, lend themselves to the estimation of L_A whose value is quite small with respect to most ground targets. The target with the lowest reflectance in a given band was thus chosen in order to best resolve L_A. The lowest reflectance in bands 4 and 5 was over Spartina alterniflora and so the ground measured reflectance for this target was transformed to radiance and subtracted from the Landsat measured radiance over a known area of Spartina alterniflora in order to derive L_A values in those bands. The coastal water mass sampled had the lower reflectance in bands 6 and 7 and so radiance values over this target were used in the same manner to calculate L_A for bands 6 and 7.

Raw data listings and categorized results were obtained for all test areas using both classification procedures. Accuracy of categorization was assessed by comparison of the categorized Landsat data with low-altitude aerial photography acquired in August, 1973 -- slightly more than one year earlier than the Landsat overpass used. Such low altitude, color infrared photography may be reliably interpreted as to the cover type present, particularly since a large amount of field knowledge of the wetlands areas involved had been acquired during this and other studies (Klemas et al., 1974, 1975). The one year separating the two data sources did not have a significant effect on the distribution of plant species at the mapping scale used (1:24,000). Categorized plots at this large scale were obtained to resolve individual pixels for accuracy analysis and this does not necessarily represent the most useful scale for displaying Landsat information for other purposes. Quantitative comparison of Landsat and photographic data was accomplished with a Bausch and Lomb "Zoom Transfer Scope" (ZTS). The optical superimposition of the two sources provided by the ZTS allowed them to be compared pixel by pixel and a record kept of differences between the data sources. Because of the impossibility of precisely registering two images with such widely divergent resolutions, and to simplify comparison, a pixel was recorded as having been correctly categorized if, when compared with the photography, it contained any of the cover type it was intended to represent.

Errors of omission and commission using both training procedures were recorded and are shown in Table 5.1. Table 5.1 represents the standard confusion/accuracy table modified to use "mapping accuracy" as a figure of merit in addition to "classification accuracy." The calculation of classification accuracy (k) is performed through equation (3) and reflects

TABLE 5.1

PIXELS CLASSIFIED FROM LANDSAT-1 DATA, OCTOBER 18, 1974

PIXELS INTERPRETED FROM AERIAL PHOTOGRAPHY

CLASS		UNCLASSIFIED	SALT HAY	SPARTINA ALTERNIFLORA	MUD	WATER	TOTAL	TOTAL OMISSIONS	% OMISSIONS	MAPPING ACCURACY
SALT HAY	1	25	1375	27	17	3	1447	72	5%	72%
	2	4	1540	2	0	0	1546	6	<1%	76%
SPARTINA ALTERNIFLORA	1	181	436	1711	3	0	2331	620	27%	72%
	2	33	470	1590	40	4	2137	547	26%	74%
MUD	1	10	3	2	184	0	199	15	8%	59%
	2	0	1	1	218	15	235	17	7%	58%
WATER	1	129	15	13	95	697	949	252	27%	73%
	2	54	10	3	103	838	1008	170	17%	82%
TOTAL	1	345	1829	1753	299	700	4926			
	2	91	2021	1596	361	857	4926			
TOTAL COMMISSIONS	1	345	454	42	115	3				
	2	91	481	6	143	19				
PERCENT COMMISSIONS	1	100%	24%	2%	39%	<1%				
	2	100%	24%	<1%	40%	2%				
OVERALL CLASSIFICATION ACCURACY	1	81%								
	2	85%								
OVERALL MAPPING ACCURACY	1	72%								
	2	76%								

'1'-Using in situ reflectance for signatures

'2'-Using "training areas" for signatures

errors of omission only, thus overestimating classification accuracy when a map representation is required.

$$k(\%) = \frac{\sum_{I=1}^{n} N_I}{\sum_{I=1}^{n} T_I} \qquad (3)$$

k = overall classification accuracy

$\sum_{I=1}^{n} N_I$ = total number of correctly classified pixels in all classes

$\sum_{I=1}^{n} T_I$ = total number of pixels in all classes

An alternative figure of merit, suggested by Kalensky and Scherk (1975), is "mapping accuracy" (M_I) derived for each class through equation (4).

$$M_I(\%) = \frac{N_I}{N_I + E_I} (100) \qquad (4)$$

M_I = mapping accuracy for class (I)

N_I = number of correctly classified pixels in class (I)

E_I = number of misclassified pixels in class (I) (the sum of omissions and commissions)

"Mapping accuracy" has the advantage of more realistically assessing positional accuracy of a categorized map by taking errors of commission and omission into account.

An equivalent measure of overall mapping accuracy (M) is calculated through equation (5).

$$M(\%) = \frac{\sum_{I=1}^{n} P_I M_I}{\sum_{I=1}^{n} P_I} (100) \qquad (5)$$

M = overall mapping accuracy

M_I = mapping accuracy for class (I)

$$P_I = \frac{T_I}{\sum_{I=1}^{n} T_I}$$

T_I = correct number of pixels in class (I)

$\sum_{I=1}^{n} T_I$ = total number of pixels in all classes

For a more detailed discussion of the statistical considerations involved the reader is referred to Kalensky and Scherk (1975).

5.3 Results

Table 5.1 shows the comparative results of accuracy analysis of the Landsat-MSS data classified using *in situ* reflectance for training (rows labeled '1') and using relative radiance "training areas" (rows labeled '2'). The conventional "training area" approach produced slightly higher mapping accuracies in three of the four classes and in overall classification and mapping accuracies. However, the differences are small in all but the "Water" category -- the reader is reminded that training for "Water" was accomplished using "training areas" in both cases and so differences in classification result solely from different positions of this signature relative to those of the other three classes in spectral space. In fact, the similarity of accuracies using the two training approaches is striking, both in class and overall accuracies

and in the types of error (commission or omission) encountered in each class. The measurement and application of solar and atmospheric corrections in this first attempt at reflectance training has certainly degraded the effectiveness of this technique although it is not known at this stage to what extent this has occurred. Studies are currently underway to evaluate alternative methods of acquiring atmospheric measurements for use in analysis. The accuracies obtained are so similar, however, that one may speculate that factors other than training technique are limiting the analysis. Two major limiting factors often cited are:

1) Large IFOV of the Landsat scanner resulting in misclassification of pixels containing more than one cover type.

2) Natural variation in the reflectance for each cover type resulting in signature overlap between classes and ambiguities in classification.

Examination of the categorized data plots showed that while many boundary pixels were misclassified, the majority of misclassified pixels were not located at category boundaries. Each of the four classes is, at one time or another, found adjacent to each of the other three categories yet, as may be seen in Table 5.1, misclassifications predominately occur between categories which are spectrally similar (see Table 5.2) -- the two vegetative categories being confused with each other while tidal mud and water are often confused. The relatively rare confusion between vegetation categories and "water" or "mud" may be attributed to boundary misclassifications while the dominant factor limiting discrimination would appear to be spectral similarities.

The in situ measurement of reflectance combined with observations of physical/environmental conditions offers a valuable insight into the sources of natural spectral variance and resulting signature ambiguities.

Table 5.2

Means and Standard Deviations of Reflectance Data Obtained by *In Situ* Measurement (except "Water"):

Category	Band 4 (0.5-0.6μm) M	σ	Band 5 (0.6-0.7μm) M	σ	Band 6 (0.7-0.8μm) M	σ	Band 7 (0.8-1.1μm) M	σ
Salt Hay:								
S. patens	8.9%	2.5%	10.4%	3.2%	27.3%	6.0%	37.3%	10.0%
D. spicata	8.6%	2.1%	10.7%	2.7%	21.5%	3.5%	30.5%	3.0%
S. alterniflora	5.0%	1.1%	5.8%	1.2%	16.0%	4.0%	23.7%	6.5%
Mud	9.1%	3.6%	10.5%	4.3%	11.4%	4.4%	11.6%	4.3%
Water	8.4%	1.4%	6.5%	1.2%	2.5%	1.9%	2.1%	2.8%

(obtained from training areas in satellite data)

Such insights cannot easily be obtained solely from satellite measurements of radiance. For instance, reflectance of tidal mud was found to be quite variable (see Table 5.2). Since moisture is a prime factor affecting the spectral characteristics of soils, reflectance over a test area of unvegetated mud was correlated with the time elapsed since the last tide of significant magnitude to inundate the area (~4 ft. above MLW). Figure 5.1 shows the result of linear regression analysis for Bands 6 and 7 (0.7μm to 0.8μm and 0.8μm to 1.1μm). Since Bands 4 and 5 (0.5μm to 0.6μm and 0.6μm to 0.7μm) reflectances for mud and open water are similar (see Table 5.2) multispectral analysis relies upon infrared spectra to distinguish these categories. Yet, as may be seen in Figure 5.1, infrared reflectance over mud varies considerably -- with almost half of this variation accounted for by tidally controlled wetting of the mud surface (r^2, the variance in 'Y' accounted for by variance in 'X' is .48 (48%) in Band 6 and .45 (45%) in Band 7). Mean infrared reflectances over

coastal water on the test date were found to be 2.5% in Band 6 and 2.1% in Band 7 (Table 5.2). Infrared reflectance over mud which has been inundated 0-8 hours prior to measurement can be low enough for there to be confusion with water, particularly in view of the standard deviations of the two targets (see Table 5.2). Thus, misclassifications of water as mud and vice versa are related, to some extent, to tidal conditions prior to and during overpasses. (Note: Some apparent errors in classification of these two categories were undoubtedly produced by differences in tidal stage present during the Landsat overpass and the aerial photography used for comparison. However, misclassifications were found even in those parts of the scene experiencing comparable phases of the tidal cycle and so signature ambiguity of the type described does occur.) It is suggested that the derivation of training signatures for tidal mud may be most effectively accomplished through careful selection of "training areas" by conventional techniques. In this case, use of training data acquired by the satellite has the advantage of representing precisely the tidal and soil moisture conditions which will be incorporated in the categorization analysis. However, if a large area is to be classified (i.e., an entire Landsat scene), care must be taken to chose several training areas representative of the varied soil moisture conditions which are present in such an area at any one time. Even so, ambiguity of signatures will inevitably occur with resulting errors in classification.

Studies of the test plant communities were also undertaken to identify sources of variability in their reflectance characteristics. The two communities are distinguished by the generally lower reflectance in all bands (see Table 5.2) of Spartina alterniflora relative to Salt

Hay (Spartina patens and Distichlis spicata). Signatures obtained, particularly in the infrared, appear to be dominated by the growth morphology of the plants -- Salt Hay exhibiting a low, dense canopy often made up of recumbent or horizontal stalks while S. alterniflora characteristically grows in less dense stands of vertical stalks through which varying amounts of marsh soil and leaf litter may be visible. Significant differences were found ($\rho < .01$) between mean reflectances in all four bands of recumbent versus vertical stands of D. spicata with the recumbent reflectance always the larger of the two. The same relationship for S. patens is suggested by the data although sample sizes were too small for tests of statistical significance. Further indication of the degree of morphological control over infrared reflectance is seen in Figure 5.2, showing reflectance in Band 6 correlated with plant height of S. alterniflora. A relatively high correlation between Band 6 reflectance and plant height ($r = .74$, $r^2 = .55$) is observed for plant heights up to 90 cm. Stands taller than this may obscure the underlying, low-reflectance soil resulting in degradation of the relationship if the entire range of plant heights is correlated ($r = .39$, $r^2 = .16$). The same relationship is shown for Band 7 in Figure 5.3. Based on morphological control of reflectance it would appear that signature ambiguity is most likely to occur between vertical stands of Salt Hay (having reflectances lower than the class mean in all bands) and tall stands of S. alterniflora with enhanced infrared reflectance.

The literature suggests that the observed correlations for S. alterniflora shown in Figures 5.2 and 5.3 may be related to biomass. Nixon and Oviatt (1973) and Williams and Murdoch (1969) have reported strong correlations between standing crop biomass (dry weight gms/m^2)

and stand height for S. alterniflora, thus providing an indirect link between reflectance and biomass. Tucker and Maxwell (1976) report that reflectance of midwestern grassland species in the 0.63μm to 0.69μm and 0.74μm to 1.00μm regions was highly correlated with a variety of measures of biomass including physiological parameters such as leaf water content. Since these two spectral regions correspond closely to Landsat Bands 5 (0.6μm to 0.7μm) and 6 and 7 (0.7μm to 1.1μm), it is possible that the observed correlations in this study result from direct relationships between reflectance and biomass rather than indirectly through plant height.

A study was carried out during the 1977 growing season (April through August) to identify the relationships between plant height, various components of plant biomass and spectral reflectance. Over 50 samples of S. alterniflora were measured using the RPMI and subsequently harvested for biomass analysis. The presumption that stand height was directly related to components of biomass was found to be of limited value as least squares linear correlation yielded a correlation coefficient of $r = .52$ between plant height and live (green) biomass (grams dry wt./m^2). Slightly better correlation was observed between plant height and total standing biomass (live and dead) with $r = .63$. Thus, Band 6 and 7 reflectance is apparently correlated to some degree with total standing biomass (excluding stem and leaf litter) but regression is of marginal value in accounting for variability in plant reflectance. More promising, although somewhat surprising, results were obtained by correlating reflectance with components of biomass directly. Band 5 reflectance correlated with green biomass inversely ($r = -.71$) as expected for a chlorophyll absorption spectral region. Band 6 reflectance correlated

very poorly (r = .09) perhaps due to sensitivity in both the red chlorophyll absorption region and the infrared leaf reflectance region. Band 7 correlation with green biomass was significantly better (r = .49) perhaps due to elimination of the ambiguous red/IR crossover present in Band 6. Nevertheless, the ineffectiveness of regression in Band 7 (r^2 = .25) is surprising in light of results of Tucker and Maxwell (1976) and others showing good correlation between infrared reflectance and green biomass. It may be that leaf litter reduces contrast in the infrared between living plant material and the background, thus reducing the sensitivity to plant density. There are also indications that sun angle may exert considerable influence on infrared reflectance for S. alterniflora but does not affect visible reflectance significantly. Empirical techniques may be useful in correcting for the effect of sun angle. Use of the Band 7/Band 5 ratio, however, yields good linear correlation (r = .89, r^2 = .79) with green biomass as shown in Figure 5.4. As suggested by Tucker and Maxwell (1976) ratioing of chlorophyll absorption and mesophyll reflection bands produces more sensitivity to green biomass than use of single band reflectances. Moreover, the relationship appears to be equally sensitive over the entire range of observed green biomass (0-1000 grams dry wt./m^2) in contrast to the asymptotic relationship found by Tucker (1977). These results indicate that several green biomass classes may be discriminable in S. alterniflora by ratioing of LANDSAT Bands 5 and 7. Resolution limitations preclude mensuration of small scale biomass variability (such as that related to distribution of tidal creeks) but large scale distribution of biomass classes related to salinity, climate, substrate and nutrient availability should be detected at LANDSAT mapping scales of 1:24,000 and smaller. The ratioing technique

has the added advantage of reducing the effects of atmospheric variation although measurements of atmospheric parameters allow more thorough evaluation of the differential spectral effects of the atmosphere.

The extent of dependence of reflectance on plant morphology suggests that most effective discrimination of species will occur when 1) there is the least intraspecific variability in the canopy and 2) there is the largest interspecific morphologic difference. Both of these conditions occur simultaneously in northern marshes early in the growing season when plant canopies have uniformly low biomass and winter conditions have thinned the stands of upright S. alterniflora while the dense, recumbent mats of the previous year's Salt Hay crop remain as they were in late fall. The optimal months for species discrimination in northern marshes may thus be April/May.

5.4 Conclusions

Digital analysis of Landsat earth resources data may realize significant advantages from in situ measurements of target radiance and transformation of these and MSS data to absolute reflectance by application of appropriate solar and atmospheric corrections. Such a technique would, in some cases, allow more accurate derivation of target signatures and facilitate temporal extension of signatures obtained. A recently developed technique for in situ radiance measurement and atmospheric correction was tested using four cover categories in Delaware's tidal wetlands.

The atmospheric correction technique, as applied, can produce comparable classification accuracies to those obtained using conventional relative radiance training. The technology exists for further

refinement of the technique if the limit of classification accuracy imposed by natural spectral variation is not reached.

Field studies indicate that while natural signature variability is a problem, the means of identifying sources of variation offered by in situ reflectance measurement may allow refinements in sampling and choice of season for data analysis to improve categorization accuracy and utility. Specifically, assessment of green biomass for S. alterniflora appears to be possible using ratioed Band 7 and Band 5 reflectances. Most effective species discrimination may result from minimizing intra-specific variation in biomass and growth morphology by choosing early growing season data for analysis.

5.5 References

Kalensky, Z. and L. R. Scherk. (1975) Accuracy of forest mapping from LANDSAT computer compatible tapes. Tenth International Symposium on Remote Sensing of Environment, Ann Arbor, MI: 1159-1168.

Klemas, V., D. Bartlett, F. Daiber, O. Crichton and A. Fornes. (1974) Inventory of Delaware wetlands. Photogrammetric Engineering. 40(4): 433-439.

Klemas, V., D. Bartlett and R. Rogers. (1975) Coastal zone classification from satellite imagery. Photogrammetric Engineering and Remote Sensing. 41(4): 499-513.

Nixon, S. W. and C. Oviatt. (1973) Analysis of local variation in the standing crop of Spartina alterniflora. Bot. Mar. 16(2): 103-109.

Rogers, R., K. Peacock and N. Shah. (1973) A technique for correcting ERTS data for solar and atmospheric effects. Third ERTS Symposium, NASA SP-351, Goddard Space Flight Center, Greenbelt, MD: 1787-1804.

Thekaekara, M. P. et al. (1971) NASA Document SP-8005.

Tucker, C. J. (1977) Asymptotic nature of grass canopy spectral reflectance. Applied Optics. 16(5): 1151-1156.

Tucker, C. J. and E. L. Maxwell. (1976) Sensor design for monitoring vegetation canopies. Photogrammetric Engineering and Remote Sensing. 42(11): 1399-1410.

Williams, R. B. and M. B. Murdoch. (1969) The potential importance of S. alterniflora in conveying zinc, manganese and iron into estuarine food chains. 2nd National Symposium of Radioecology, Atomic Energy Commission: 431-439.

5.6 List of Figures

Figure 5.1: Graph of reflectance of bare mud in Bands 6 and 7 vs. time since last tidal inundation. Regression results are shown.

Figure 5.2: Graph of Band 6 reflectance of Spartina alterniflora vs. plant height. Regression results are shown.

Figure 5.3: Graph of Band 7 reflectance of Spartina alterniflora vs. plant height. Regression results are shown.

Figure 5.4: Graph of ratioed reflectance in Bands 7 and 5 vs. green biomass for Spartina alterniflora. Regression results are shown.

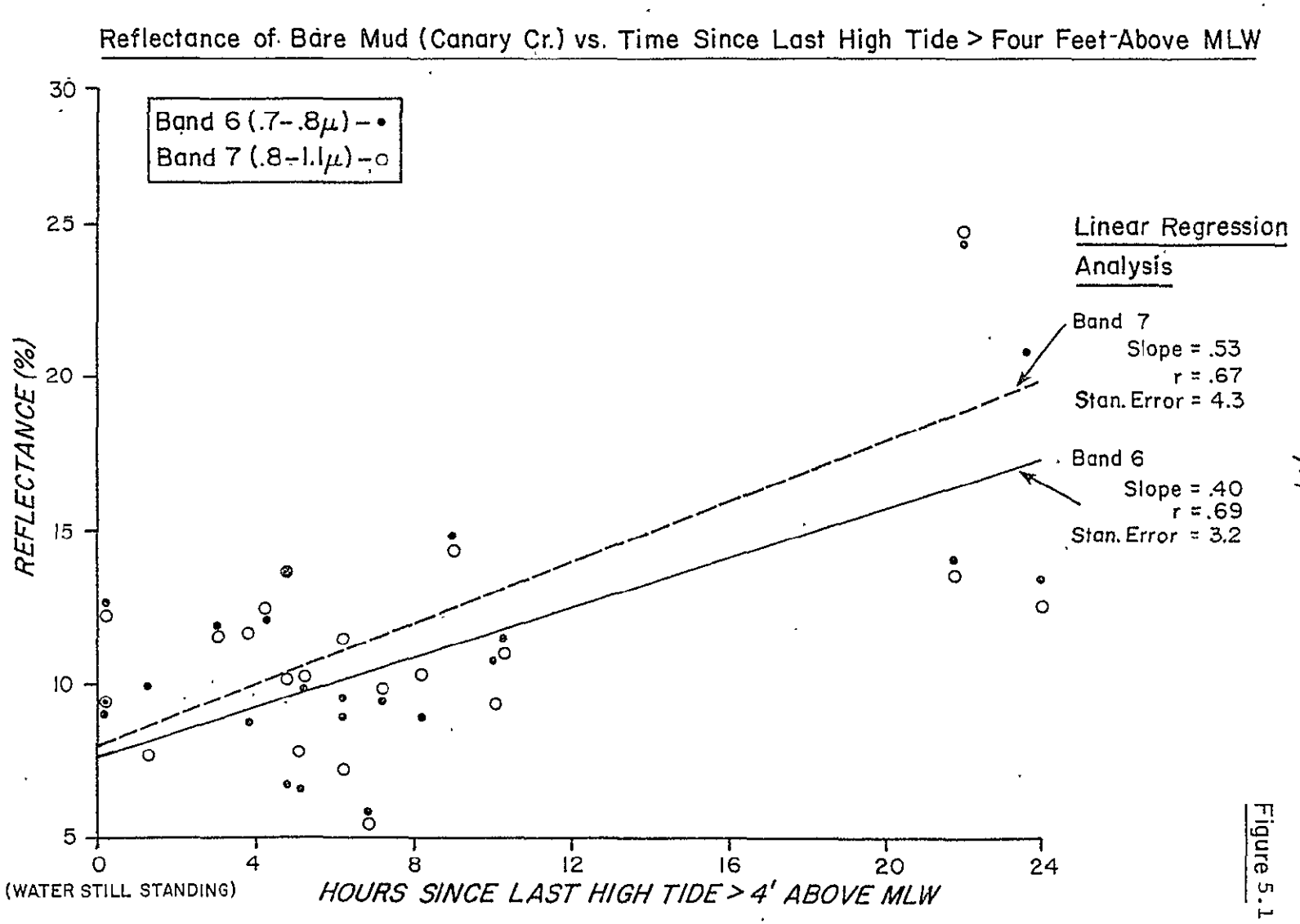
Reflectance of Bare Mud (Canary Cr.) vs. Time Since Last High Tide > Four Feet Above MLW
Band 6 (.7-.8μ) - •
Band 7 (.8-1.1μ) - ○
REFLECTANCE (%)
30
25
20
15
10
5
0
4
8
12
16
20
24
(WATER STILL STANDING)
HOURS SINCE LAST HIGH TIDE > 4' ABOVE MLW
Linear Regression Analysis
Band 7
Slope = .53
r = .67
Stan. Error = 4.3
Band 6
Slope = .40
r = .69
Stan. Error = 3.2

Figure 5.1

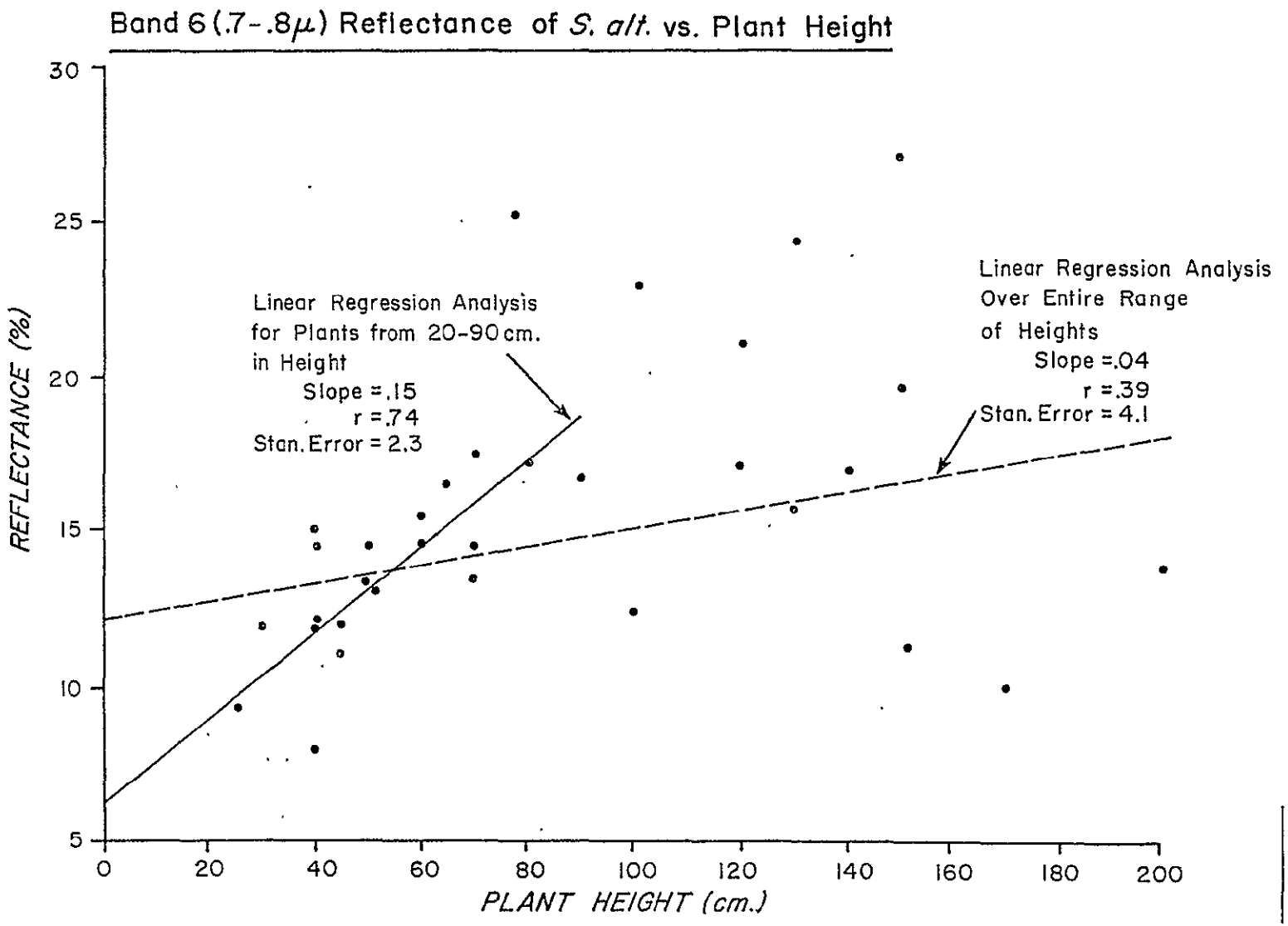
Band 6 (.7-.8μ) Reflectance of S. alt. vs. Plant Height
REFLECTANCE (%)
30
25
20
15
10
5
0
20
40
60
80
100
120
140
160
180
200
PLANT HEIGHT (cm.)
Linear Regression Analysis
for Plants from 20-90 cm.
in Height
Slope = .15
r = .74
Stan. Error = 2.3
Linear Regression Analysis
Over Entire Range
of Heights
Slope = .04
r = .39
Stan. Error = 4.1

Figure 5.2

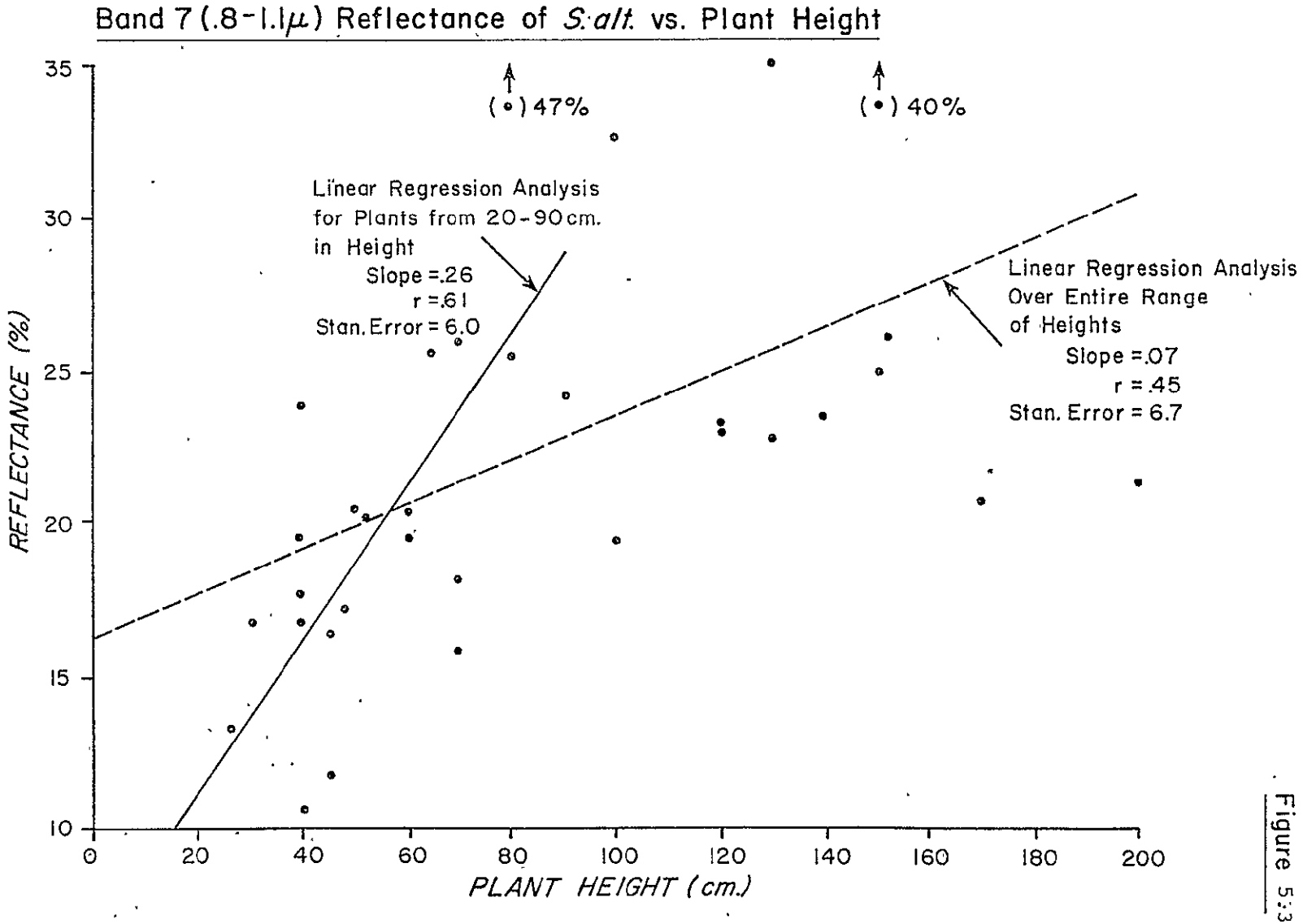
Band 7 (.8-1.1μ) Reflectance of S. alt. vs. Plant Height
(•) 47%
(•) 40%
Linear Regression Analysis
for Plants from 20-90 cm.
in Height
Slope = .26
r = .61
Stan. Error = 6.0
Linear Regression Analysis
Over Entire Range
of Heights
Slope = .07
r = .45
Stan. Error = 6.7
REFLECTANCE (%)
PLANT HEIGHT (cm.)
35
30
25
20
15
10
0
20
40
60
80
100
120
140
160
180
200

Figure 5:3

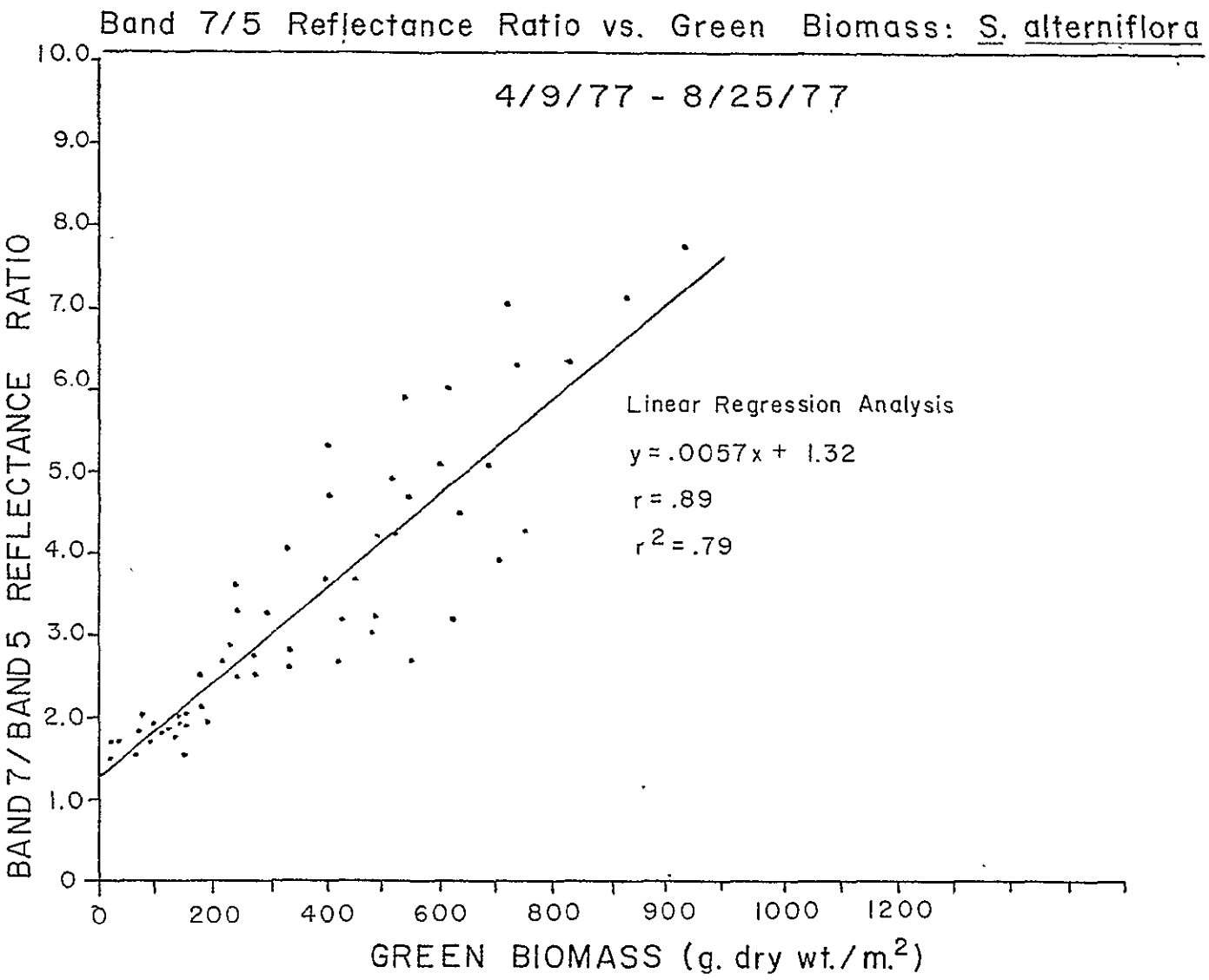
Band 7/5 Reflectance Ratio vs. Green Biomass: S. alterniflora
4/9/77 - 8/25/77
BAND 7/BAND 5 REFLECTANCE RATIO
10.0
9.0
8.0
7.0
6.0
5.0
4.0
3.0
2.0
1.0
0
0
200
400
600
800
900
1000
1200
GREEN BIOMASS (g. dry wt./m.2)
Linear Regression Analysis
y = .0057x + 1.32
r = .89
r2 = .79

Figure 5.4

VI. ANALYSIS OF THE EFFECTS OF OFFSHORE DEVELOPMENT ON COASTAL LAND USE IN THE KENAI REGION, ALASKA

6.0 Introduction

The quest for energy independence is certainly one of the premier issues facing the United States today. Energy forms the essence of our society. Acquiring the sources of it, producing it, and using it, is the basis of our free-market economy. The problem of expanding energy demands is compounded by another force active at work within our society -- environmental protection and conservation. As a result of our cognizance of the environment and its nonrenewable resources, there must be a careful examination of the consequencies of resource exploitation before such exploitation can proceed.

This section addresses one facet of this examination process. It analyzes a particular data acquisition technology, remote sensing, and the ability of this technology to evaluate the impacts of one form of energy exploitation, offshore oil and natural gas development. The objective of this study then, is to determine to what extent remotely sensed data can be used in the evaluation of onshore impacts of offshore petrochemical development. It is hoped that this analysis will provide some insights into the prospects of using remotely sensed data as a predictive tool in assessing such impacts.

6.1 Offshore Petrochemical Development

The Alaskan petrochemical industry began with the discovery of oil onshore at Swanson River in 1957. The discovery had two immediate effects on Kenai. First, it insured the Kenai area of being Alaska's first petrochemical complex; and second, it opened-up the Kenai area to further exploration. It was this second effect which led to the bulk of the land

use impacts on Kenai by opening up the offshore oil and natural gas fields. Table 6.1 lists the oil and gas fields in the Kenai-Cook Inlet area along with their location and date of discovery. Table 6.2 presents the crude oil production values for the same fields.

By 1961, the mining and construction industries accounted for 10 percent of the total employment of the region. At that time the development of the Swanson River oil and gas fields and the Kenai gas fields was continued while the exploration activities were ongoing for other fields. By comparison, the state's mining industry represented less than eight percent of total employment with about sixty percent of the mining employment engaged in metal minerals and coal extraction.

Table 6.3 presents a contract construction category which includes workers employed by general and special trade contractors involved in projects not directly related to hydrocarbon activity, e.g., residential and commercial buildings, streets and roads, plumbing and carpentry. From Table 6.3 it is also possible to discern four distinct phases of mining and construction employment between 1961 and 1972. The first phase covers the period 1961 to 1964. Therein mining employment remained relatively stable. The second phase covers the period 1965 to 1968. During this period mining employment increased six-fold to a peak of nearly 1,100 jobs in 1968. Similarly, construction employment climbed to a peak of 1,200 workers, near ten times its 1964 level. The third phase, 1968 to 1970, was marked by a rapid decline in both categories of employment. While the mining work force fell by nearly 450 workers, there was a loss of 850 construction jobs. The final phase, 1970 to 1972 marked a relative stabilization period. Although mining employment declined by an additional 125 workers and construction gained about 80 jobs, it is clear that the more dramatic boom-and-bust period had passed.

Table 6.1

Oil and Natural Gas Fields of the Kenai - Cook Inlet Region

Field	Type	Location	Date of Discovery Well
Swanson River	Oil and Gas	Onshore	August, 1957
Kenai	Gas	Onshore	October, 1959
West Fork	Gas	Onshore	September, 1960
Falls Creek	Gas	Tidelands	May, 1961
Sterling	Gas	Onshore	August, 1961
West Foreland	Gas	Onshore	April, 1962
Middle Ground Shoal	Oil	Offshore	June, 1962
North Cook Inlet	Gas	Offshore	September, 1962
Beluga River	Gas	Onshore	December, 1962
North Middle Ground Shoal	Gas	Offshore	November, 1964
Trading Bay	Oil	Offshore	June, 1965
Birch Hill	Gas	Onshore	June, 1965
Granite Point	Oil	Offshore	June, 1965
McArthur River	Oil and Gas	Offshore	October, 1965
Moquawkie	Gas	Onshore	November, 1965
North Fork	Gas	Onshore	December, 1965
Nicolai Creek	Gas	Onshore	May, 1966
Ivan River	Gas	Onshore	October, 1966
Beaver Creek	Gas	Onshore	February, 1967
Albert Kaloa	Gas	Onshore	January, 1968
Redoubt Shoal	Oil	Offshore	September, 1968

Source: State of Alaska, Department of Natural Resources, Division of Oil and Gas, Statistical Report, 1973.

Table 6.2 118

Crude Oil Production in the Kenai - Cook Inlet Region values in thousands of barrels

Year	Onshore	Offshore	Total Kenai-Cook Inlet Production	Kenai as Percent of Total Alaska Production
1959	187	-	187	100.0
1960	578	-	578	100.0
1961	6,327	-	6,327	100.0
1962	10,259	-	10,259	100.0
1963	10,740	-	10,740	100.0
1964	11,054	-	11,054	100.0
1965	11,099	32	11,131	100.0
1966	11,712	2,653	14,365	100.0
1967	12,980	15,934	28,914	100.0
1968	13,619	52,524	66,143	100.0
1969	13,151	60,887	74,038	99.6
1970	12,408	70,006	82,414	98.6
1971	11,466	66,162	77,628	98.5
1972	8,896	63,742	72,638	98.7

Source: State of Alaska, Department of Natural Resources, Division of Oil and Gas, Statistical Report, 1973.

Table 6.3 119

Kenai - Cook Inlet Employment in Mining and Quarrying Construction

Year	Mining and Quarrying (No. of Persons)	Construction (No. of Persons)
1961	154	57
1962	169	94
1963	158	101
1964	179	127
1965	212	259
1966	415	432
1967	916	821
1968	1,098	1,209
1969	966	739
1970	652	354
1971	524	398
1972	529	432

Source: State of Alaska, Department of Labor, Alaska Work Force Estimates by Industry and Area for Kenai - Cook Inlet Labor Market Area, 1961 to 1972.

Descriptively, these hydrocarbon-related employment periods can be classified as follows:

(1) 1961-1964	Onshore Development
(2) 1965-1968	Offshore Development and Petrochemical Construction
(3) 1969	Development Decline
(4) 1970-1972	Production

6.2 Remote Sensing Analysis and Change Assessment

The technique of land use mapping and land use change detection using remotely sensed data is well established. In documenting offshore petroleum-related land use changes the most significant changes occur within the generalized urban and built-up category. For this reason the following land use change analysis has been based primarily on Level II urban and built-up categories from the Anderson classification (1976), in concert with several associated non-urban categories. For illustrative purposes these have been consolidated into a single category called urban and developing land (Figure 6.1).

The remote sensing technique used in this study is based on the rationale that the land use changes occurring in Kenai (a frontier region), after 1964, could almost entirely be attributed to offshore petrochemical development. The basis for this rationale stems from the frontier nature of the Kenai area where, prior to offshore drilling, there was no heavy industry and no commercial support function. The assumption can be made, therefore, that most, if not all, land use changes occurring after the advent of offshore activity are in some way associated with that activity.

6.21 Aircraft

Accepting this premise, then, the next step is to document the urban land uses in Kenai prior to, and subsequent to, the offshore development activity. This is done in the series of land use maps presented in Figure 6.1. Each map, produced from medium to high-altitude aircraft photography, depicts the urban and urban-associated land use conditions at Kenai for a specific time. In that context each can be used as an indicator of change when compared to the next earliest map.

Urban and Developing Land Use - 1951

The urbanized condition of Kenai in 1951 is illustrated in the map at the upper left of Figure 6.1. The most dominant feature on the map at that time was the airstrip, which appears as a cross on the map. Immediately south of this was an area of mixed urban uses. This is the site of the old Kenai settlement. It is essentially a residential section interspersed with small commercial establishments. Much of what the map depicts is in a transitional condition. This reflects the "Fifties/Construction Boom" which came directly as a result of the homesteading period. It also illustrates well the pre-offshore petroleum industry landscape of Kenai.

Urban and Developing Land Use - 1961

Although the 1961 aerial photo mission did not completely cover the Kenai test site, the northern and western portions of the site were photographed (Figure 6.1, upper right). From a development viewpoint, however, these were the most important areas.

The new built-up areas just west and north of the airfield are primarily residential. There are a small number of service-oriented functions mixed in here. Moving farther up the coast the changes which occurred since 1951 were essentially to residential and commercial uses. These changes reflect the development of the onshore oil and gas fields at Swanson River,

Kenai, and West Fork. The one exception was Wildwood Station, the U. S. Army Communications Center. In 1951 ground for this facility had been cleared and by 1954 the facility was in operation.

By 1961 North Kenai Road had been extended beyond Nikishka. This extension was primarily the result of the Swanson River development. The road serviced the petroleum loading pier and storage facility built at Nikishka in 1959. It also fostered the growth of residential land in North Kenai.

Urban and Developing Land Use - 1967

The 1967 developed land situation of the Kenai test site is illustrated in the lower left corner of Figure 6.1. A considerable amount of change occurred during the 1961 - 1967 period. In Table 6.3 it was illustrated how the mining and construction workforce remained relatively stable between 1961 and 1964. Using that as a guide it can be assumed that the majority of the change between 1961 and 1967 occurred after 1964, that is, after the discovery of oil and gas offshore.

This period was marked by a considerable amount of commercial and industrial development, especially in North Kenai, and all along the North Kenai Road. At the Nikishka terminal a refinery had gone into operation and another processing facility was under construction.

Farther north, near Nikishka No. 2 a second refinery had also been put into operation. Just adjacent to this plant there was considerable residential and commercial growth. The residential development was largely in the form of mobile home parks along the main road. A number of homesteads were also beginning to appear, just east of the North Road, around the numerous lakes in this area. The commercial development was more varied. It did, however, contain itself more strictly along the main road.

Urban and Developing Land Use - 1972

By 1972, when the petrochemical development of the Kenai-Cook Inlet area had entered its second year of the production phase, several significant changes had occurred. In the north, additional residential land had appeared adjacent to Nikishka No. 2. At the Nikishka terminal area two additional refineries were put into operation. Along the main road to the south there was some increase in residential areas and large increases in petrochemical support facilities. A larger number of consumer-oriented services were not also beginning to appear as the population was beginning to stabilize with the close of the boom period.

Within the limits of the City of Kenai there was a sizeable increase in the number of permanent single-family residential units during the 1967-1972 period. There also appeared to be a commensurate increase in commercial and services activities within the city.

6.22 Landsat

Effective utilization of the remote sensing technique for change detection requires a mechanism for the timely update of source materials. Aircraft flights over the Kenai area have been infrequent, and the contracting of a photo-mission can be expensive.

Since 1972, the date of the last aircraft mission over the Kenai area, the Landsat 1 and 2 spacecraft have made numerous data-collecting passes over the Kenai-Cook Inlet area. In this study the Landsat system was not evaluated for its ability to discriminate particular land use and land cover types. Of more importance was an examination of Landsat's ability to discern areas of land use and land cover change. In a highly dynamic region, as Kenai has been since the advent of offshore petrochemical development, the monitoring of the frequency and magnitude of change is essential to an understanding of the process of land use change.

Urban and Developing Land Use - 1976

The urban and developing land condition of the Kenai test site, in 1976, is depicted in Figure 6.2. This interpretation was made from enlarged (1:250,000-scale), Band 5 and 7 Landsat images. Several problems are inherent in working with such imagery. The discrimination of land use types, for example, which is really the delineation of photographic tonal and textural groupings, can be very difficult. This difficulty results from the variety of land use types present in a scene, their size and shape, and similarities in their spectral response (Alexander and others, 1975). The problem is exacerbated by the emulsion characteristics of photographic films and papers.

The result of these factors is an interpretation of land use which appears more generalized. The urban and developing land polygons in Figure 6.2 appear, therefore, as an analgam of smaller polygons. Many of these smaller polygons were not distinct enough to be delineated as in the interpretations derived from aircraft photography.

In addition to data generalization there is an associated problem involved in determining areas of land use change. Whether or not an area has undergone change or just appears that way due to photography characteristics is difficult to detect. Without correlative information, such as field gathered data, an interpretation of such areas can only be intuitive at best.

Based on photographs taken from a low-altitude aircraft and an automobile at the Kenai test site, the map depicted in Figure 6.2 does in fact show some land use changes. Unfortunately, these changes are largely obscured by the spatial generalization of the data.

This treatment of Landsat's ability to discern changes, within a small geographical area, has ignored a more precise approach. That approach

is to map land use and subsequent changes by automated techniques using the Landsat digital tapes. In his work on automated mapping in selected U. S. metropolitan areas Ellefsen (1974) demonstrated that Landsat data could be used to generate detailed and accurate maps of urban and developing land uses. He presents a table of land use classes best determined through computer classification of spectral data (Table 6.4).

Interestingly, these land use classes fit well the types of land uses most prevalent in the Kenai test site. For example, the Commercial - Industrial, Transportation category comprises a large proportion of the developed land of North Kenai. Furthermore, this classification not only provides for the delineation of residential regions, but devotes an entire category to mobile home parks. Mobile homes form a large part of the total housing in the Kenai test site.

The most significant portion of Ellefsen's work, vis-a-vis Landsat computer mapping in the Kenai area, is the accuracy of the computer classification. A section of the computer classified land use map of Phoenix was tested for accuracy. It was determined, for an 18 square kilometer sample, that the residential category was 95.9 percent correct; the commercial-industrial category was 91.7 percent correct; barren open space was 91.3 percent; irrigated open space was 89.7 percent; and water was 92.3 percent. In combination these figures averaged to an overall accuracy value of 94.4 percent. This clearly establishes the potential of Landsat data to accurately delineate urban and developing land. It further indicates, then, the potential value of Landsat data in assessing impacts of offshore oil and gas development.

Table 6.4

Land use classes optimally discriminated by computer classification of Landsat MSS data.

Classes	Characteristics
Commercial - Industrial, Transportation	Composed of extensive flat-roofed surfaces, service areas, and ancillary transportation surfaces
Parking Lots	Usually comprising both darker asphalt surfaces and lighter concrete surfaces
Residential	Comprising individual houses, landscaping, drives, and residential streets (note: large flat-roofed apartments are often spectrally too similar to commercial-industrial to be correctly included in this class)
Mobile Homes	Close-set, metal-roofed units with one of the most highly reflective surfaces on the entire ERTS frame
Improved Open Space (grass covered)	Irrigated grass areas such as parks, golf courses, and school grounds ranking very high in the infrared band
Open Space (bare ground)	Non-irrigated areas usually abandoned agriclutural land or land in process of being developed.
Open Space (with trees)	Occurs in parks and along streams. May also be orchards
Water	Includes reservoirs, lakes, bays, etc.

6.3 Separating Offshore - and Onshore - Related Land Use Changes

The essential element of this study has been the documentation of land use and land cover changes resulting from offshore petrochemical development. This documentation procedure is not, however, as straight forward as it may seem. Land use changes occur in response to numerous variables. For example, the construction of a new road into a formerly undeveloped area could initiate a development chain reaction! First houses, then services, then institutions, etc. This process can be further complicated by other chain reactions resulting from completely different stimuli in the same area. When this occurs it becomes very difficult to differentiate the effects etiologically.

In the Kenai example the series of urban and developing land maps in Figure 6.1 do not reflect only the effects of offshore petrochemical development. For example, the 1951 map depicts a pre-petrochemical development land condition resulting from the inveterate salmon fishing industry and the more recent homesteading boom.

In 1957 oil was discovered onshore at Swanson River. The changes present in this 1961 map primarily reflect the effects of this discovery. Significantly, since these changes result from and support only the onshore component of petrochemical development, on analysis of this land use and land cover condition is still relatively simple.

With this 1974 discovery of oil offshore in Cook Inlet the complexity of land uses increased dramatically. This complexity begins to manifest itself in the 1967 map. The new urban and developing land appearing on this map cannot be easily separated into offshore/onshore support development by looking at the aircraft photography. This distinction is equally difficult, in many instances, when viewed from the ground.

Often there is no differentiation to be made. Many industries and commercial establishments serve both onshore and offshore production. The Nikishka terminal area, for example, refines and loads onto tankers petrochemical products from both onshore and offshore wells. Furthermore, welding and pipefitting contractors and other similar services in the Kenai area work with both forms of drilling operations.

While remote sensing techniques alone are inadequate for this type of analysis, their use in concern with other data sets, e.g. population data, labor statistics, etc., provides a more accurate account of land usage. From the labor and industry data presented in the section on offshore petrochemical development (Tables 6.2 and 6.3) it is possible to demonstrate the importance of offshore development in the land changes depicted on the 1967 map in Figure 6.1. Between 1962 and 1963, when oil was first discovered offshore, onshore oil production increased at a very low rate. Similarly, during the same period the number of mining and construction jobs increased at a steady, but low, rate.

This trend indicates that some land use changes would have occurred as a result of the onshore development, but probably not a large number of changes. The urban and developed land area certainly would not have doubled as a result of these changes.

During the post offshore discovery years, 1965 to 1967, onshore oil production continued its slow, steady increase. Offshore production, however, increased from 32 thousand to nearly 16 million barrels per year. Whereas in 1965 offshore oil accounted for less than 1 percent of the total production, in 1967 it accounted for nearly 54 percent. Also the number of mining and construction jobs quadrupled between 1965 and 1967.

Clearly, these data indicate that the changes occurring during the 1961 to 1967 period occurred after 1964, that is, during the initial phases of offshore oil development. It is felt, therefore, that the 1967 map in Figure 6.1 largely reflects a response to offshore petrochemical development.

The same logic can be applied to the 1968 to 1972 period. During 1968 onshore production continued its slow increase while offshore production more than tripled. In 1969 the onshore industry began a decline. This decline was slow at first but then jumped to a rate of 22 percent between 1971 and 1972.

Offshore production, on the other hand, continued its rise between 1968 and 1970 at a rate of about 15 percent per year. In 1970 offshore production peaked at slightly more than 70 million barrels. At that time the Kenai-Cook Inlet offshore industry accounted for nearly 80 percent of all Alaskan oil production. Between 1970 and 1972 offshore oil production declined at a rate of 4 to 5 percent per year.

What this means in terms of land development seems clear. Between 1968 and 1972 the production of offshore oil exceeded the production of onshore oil by over 80 percent. Such a predominance of offshore oil dictates a concurrent predominance in consequent land use change. It is believed, therefore, that the changes occurring on the 1972 urban and developing land map, in Figure 6.1, are almost entirely the result of offshore development. Some changes may be the result of both on and offshore industries, but very little, if any, are resultant solely from onshore development.

In summary, separating onshore and offshore related land use changes is difficult, if not impossible, to do from remotely sensed data alone. Correlative data sets are necessary if any reliable breakout is to be made.

6.4 Conclusions

Interpretation of remotely sensed data is a valid and valuable technique for evaluating onshore impacts of offshore petrochemical development. There are, however, limitations inherent to the use of such information.

High-altitude aircraft photography can be used to document specific land use and land cover types indicative of petrochemical development. It can also be used to monitor and define land use and land cover changes resulting from petrochemical development.

Similarly, Landsat imagery can be used to document land use types and changes, but from more generalized categories and to a more limited degree. Results of other studies on computerized classification of digital data from the Landsat multispectral scanner (MSS) indicate, however, that this type of remote sensing platform can provide almost as much detail as the aircraft photography when used in frontier areas such as Kenai.

The primary deficiency in the use of remotely sensed data occurs in areas where petrochemical development is proceeding both onshore and offshore. In such cases the designation of specific land uses as either onshore-related impact of offshore-related impact is virtually impossible. This separation becomes practical, however, when additional data such as population, labor, resource development and similar statistics are analyzed in concert with remotely sensed data.

In summary, conventional remote sensing technology provides excellent information for analysis of types and locations of land changes which result from offshore oil and gas development. The disadvantage to the use of this information is its inability to identify the functional relationships of many land use and land cover types. Visual analysis of Landsat imagery provides an update capability which is often not available through

conventional means but which is limited to general classification of land use categories. Results reported by Ellefsen (1974) suggest that better results can be achieved through automated analysis of digital data.

6.5 References

Alexander, R. H., et al. (1975) Interpretation, compilation and field verification procedures in the CARETS project. National Aeronautics and Space Administration, Goddard Space Flight Center, and U. S. Geological Survey, Type III Final Rept., Under ERTS-1 Inv. SR-125 (CARETS), V. 5.

Anderson, J. R., E. E. Hardy, J. T. Roach and R. E. Witmer. (1976) A land use and land cover classification system for use with remote sensor data. U. S. Geological Survey Prof. Paper 969. 28 pp.

Ellefsen, R. A. (1974) Automatic digital processing of ERTS-1 MSS data in an urban land-use mapping experiment. Ann. Mtg. Amer. Soc. Photogramm., St. Louis, Mo. 12 pp.

State of Alaska. (1961-1972) Alaska work force estimates by industry and area for Kenai-Cook Inlet labor market area. Dept. of Labor, Juneau, Alaska.

State of Alaska. (1973) Statistical report. Dept. of Natural Resources, Division of Oil and Gas, Juneau, Alaska.

6.6 List of Figures

Figure 6.1: Urban and developing land, Kenai test site: 1951, 1961, 1967, 1972, as interpreted from aircraft photography

Figure 6.2: Urban and developing land, Kenai test site: 1976, as interpreted from Landsat MSS imagery

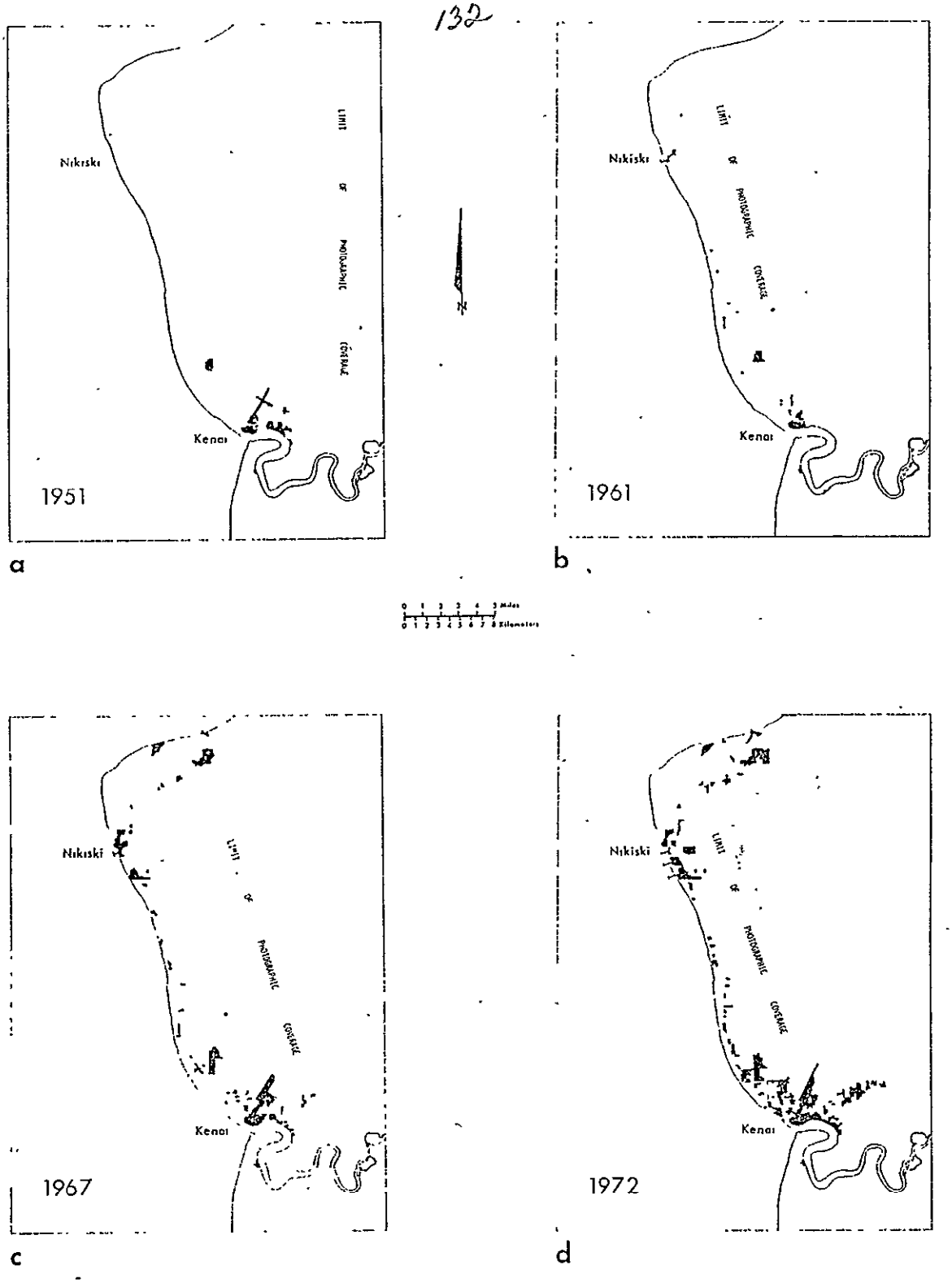

Figure 6.1. Urban and developing land, Kenai test site: 1951, 1961, 1967, 1972, as interpreted from aircraft photography.

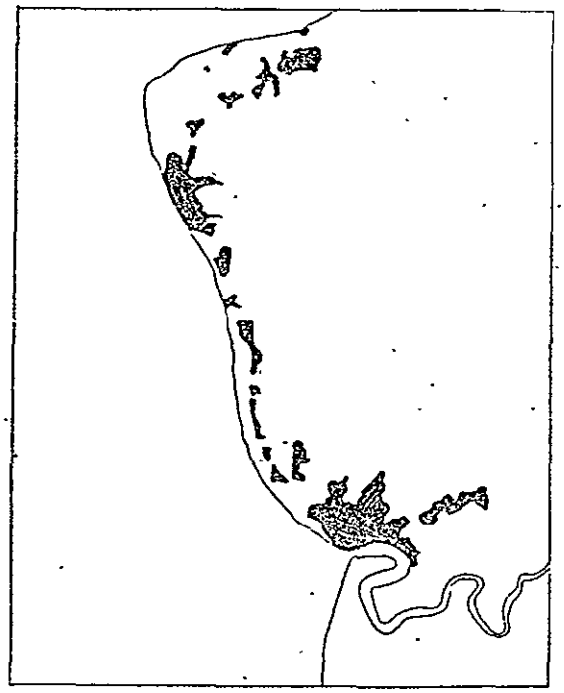

Figure 6.2 Urban and developing land - 1976, Kenai, Alaska, as interpreted from Landsat MSS imagery.

APPENDIX A - Publications and Invited Presentations

Bartlett, D. and V. Klemas. (1977) Variability of wetland reflectance and its effect on automatic categorization of satellite imagery. Proc. Amer. Soc. Photogramm., 43rd Ann. Mtg., Washington, D. C.

Eight reports on significant results to NTIS.

Klemas, V. (1975) Invited presentation to Captain Jacques Cousteau and Dr. Philippe Cousteau on Ocean Current Measurement with Integrated Drogue-Aircraft-Satellite Systems. NASA Headquarters, Washington, D.C.

Klemas, V. (1975) Remote sensing of wetlands vegetation and estuarine water properties. Proc. 3rd Internatl. Estuarine Res. Conf., Galveston. (Invited paper)

Klemas, V. and D. Bartlett. (1975) Application of ERTS-1 and Skylab to coastal zone management. NASA Earth Resources Survey Symp., Houston.

Klemas, V., D. Bartlett and R. Rogers. (1975) Coastal zone classification from satellite imagery. Photogramm. Eng. and Remote Sensing, Journal of the Amer. Soc. Photogramm., 41(4): 499-513.

Klemas, V., G. Davis and R. Henry. (1977) Satellite and current drogue studies of ocean-dispersed waste drift. J. Water Poll. Control Fed. 49(5): 757-763.

Klemas, V., G. Davis, J. Lackie, W. Whalen and G. Tornatore. (1977) Satellite, aircraft and drogue studies of coastal currents and pollutants. IEEE Transactions on Geoscience Electrnics, GE-15(2): 97-108.

Klemas, V., G. Davis, H. Wang, W. Whelan and G. Tornatore. (1974) A cost-effective satellite-aircraft-drogue approach for studying estuarine circulation and shelf waste dispersion. Proc. Ocean '75 Conf., San Diego.

Klemas, V., G. Davis, H. Wang and W. Whelan. (1975) Monitoring estuarine circulation and ocean waste dispersion using integrated satellite-aircraft-drogue approach. Internatl. Conf. on Environ. Sensing and Assessment, Las Vegas.

Klemas, V. and D. F. Polis. (1976) Remote sensing of estuarine fronts and their effects on oil slicks. Univ. Delaware Publ. CMS-RANN-4-76. 48 pp.

Klemas, V. and D. F. Polis. (1977) Remote sensing of estuarine fronts and their effects on pollutants. Photogramm. Eng. and Remote Sensing 43(5): 599-612.

Klemas, V. M. Otley, C. Wethe and R. Rogers. (1974) ERTS-1 studies of coastal water turbidity and current circulation. Am. Geophys. Union 55th Ann. Mtg., Washington, D. C.

Klemas, V., G. Tornatore and W. Whelan. (1975) A new current drogue for monitoring shelf circulation. Am. Geophys. Union, 56th Ann. Mtg., Washington, D.C.

LANDSAT follow-on investigation interviews conducted at NASA Goddard Space Flight Center, Greenbelt, Md. on October 18, 1976.

NASA Headquarters Review of task on comparison of training site and spectral signature techniques for classifying coastal land cover, Washington, D. C., March 31, 1977.

Review of Basic Research in NASA-related Environmental Quality Monitoring held at NASA Langley Research Center, Hampton, Va. on December 8, 1976.